



CHANCE project

(Contract Number: 755371)

FINAL REPORT WP4 DELIVERABLE (D4.5) Work Package 4

Author(s): **J. Velthuis, A. Alrheli, D. Barker, C. De Sio, M. Mhaidra, D. Kikola, A. Kopp, P. Stowell, L. Thompson, M. Weekes**

Reporting period 3: 01/06/2020 – 31/03/2022

Date of issue of this report: 20/4/22

Start date of project: 01/06/2017

Duration: 58 Months

<i>This project has received funding from the Euratom research and training programme 2014-2018 under grant agreement No 755371;</i>		
Dissemination Level		
PU	Public	X
CO	Confidential, only for partners of the CHANCE project and EC	

History chart			
Status	Type of revision	Partner	Date
Draft	Initial version	UNIVBRIS, WUT and USFD	

Reviewed by

Andra

Approved by

The Executive Board



1. Overview

Muon scattering tomography (MST) is a non-invasive method that allows to inspect (large) objects from a safe distance without the introduction of radiation. It exploits the natural background radiation. By measuring the incoming and outgoing radiation, the contents of the object under inspection can be determined. The technique can be used to address many challenges including imaging the contents of nuclear waste drums.

In CHANCE we developed a mobile muon tomography system to inspect waste drums. We developed new and improved algorithms to image waste drums. In particular, we focused on the material identification of blocks of material inside the waste drums, on the detection of small gas bubbles in waste drums and inspection of CASTOR drums.

Despite issues out of our control with the experimental setup, we have made significant improvements in the field. We published 10 papers in the field, 1 more was submitted recently and 1 more is in preparation, gave 14 conference talks and three PhD theses are in preparation.

During the project we aimed for a deployment of the system. We have spoken to several waste management organisations, however with the Covid-19 situation a deployment could not be realised. We did raise the profile of muon tomography. Several new projects have spun out of the CHANCE program as well.

This document starts with an introduction to muon tomography. Next the experimental system is presented. This is followed by an overview of our work on novel algorithms. Then the deployment plans are discussed followed by raising awareness and future and current muon tomography projects that are a result of the CHANCE project.

2. Muon tomography

As part of the CHANCE project, work package 4 the Muon Tomography work package, we built and operated a mobile muon tomography system using RPCs and drift chambers and operate it in a non-laboratory environment. This report details the performance and challenges in the realisation of the system.

Muon scattering tomography (MST) is a non-invasive method which shows a great potential to produce 3D images of closed objects from a safe distance. MST uses cosmic rays as probes. Cosmic rays are high energy, charged particles which come to the Earth's atmosphere from outer space. In the atmosphere, cascades of new particles are produced. The main type of particles that reach sea level are muons. Muons are identical to electrons, but 200 times heavier. Muons can go through large amounts of material as they do not scatter very much due to their high mass.

Muon tomography is being developed for many different applications, both using Monte Carlo simulation studies and experiments. A focal point of muon tomography is the characterization of nuclear waste drums and related security applications, where contents of concrete or bitumen filled waste drums are studied. Key issues here include the potential presence of gas bubbles in the matrix of the waste drum [1] and identify the material inside the drums [2, 3, 4]. Security applications were mainly focused on detection of lumps of high-Z material in cargo containers [5, 6], but work on the detection of explosives is ongoing as well [7]. Examples of MST trials include experimental studies of concrete blocks [8, 9] and detection of rebars in concrete walls and floors [10].

The main advantage of muon tomography is its non-invasiveness, no additional radiation is introduced to perform the scan. Furthermore, cosmic radiation is abundant. The cosmic muon flux at sea level is about $10000 \text{ m}^{-2}\text{min}^{-1}$ [11] and has a wide angular and momentum spread, see figure 2.1. Cosmic muons are highly penetrating, so they are perfect in situations where the tested volume is shielded by a layer of metal or rock. Furthermore, since muons are charged particles, they are relatively easy to detect.

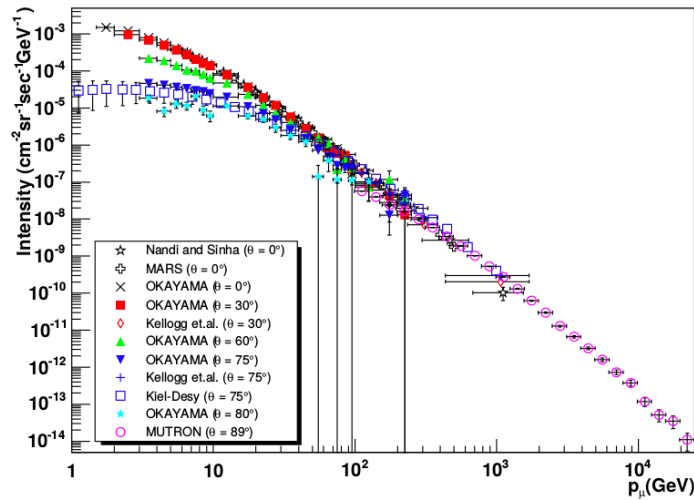


Figure 2.1: Muon intensity as a function of muon momentum, where θ is the zenith angle. Taken from [12].

When traversing material, Coulomb interactions take place between the muons and the nuclei of the material. As a result, muons exit the material under an angle. The angular distribution of scattering of muons can be described by a Gaussian distribution with a mean of zero and a standard deviation σ_θ described by [13]:

$$\sigma_\theta = \frac{13.6 \text{ MeV}}{pc\beta} \sqrt{\frac{T}{X_0}} \left[1 + 0.038 \ln \left(\frac{T}{X_0} \right) \right] \quad (2.1)$$

$$X_0 \approx \frac{716.4A}{Z(Z+1) \ln \left(\frac{287}{\sqrt{Z}} \right)} [g \cdot \text{cm}^{-2}] \quad (2.2)$$

where p is muon's momentum, β is muon's speed divided by the speed of light c , T is the thickness of the material and X_0 its radiation length. A is the atomic weight of the medium in g/mol. The standard deviation depends on the atomic number, Z , of the traversed material. Under the assumption that scattering occurs in single locations and by reconstructing the incoming and outgoing trajectories of the muons, the scattering angle distribution can be reconstructed and thus information about the traversed material can be extracted.

There are two ways to utilize muons: one is to record the number muons absorbed in the material, which is known as radiography, and to measure the scattering, which is known as muon tomography. The radiography is particularly relevant for the scanning of large objects like waste silos. Radiography returns density (contrast) information. Muon tomography is utilized for objects like waste drums up to cargo containers and can provide more information on the scanned object. Muon tomography requires measurement of the incoming and outgoing muon path and thus can only provide information on the volume sandwiched between two detector systems. Muon radiography only requires measurement of the transmitted muons. As a result, very large objects can be scanned with only one (small) detector system.

Muon tomography requires both the incoming and outgoing muon trajectory to be measured. Hence, the object under inspection needs to be covered on both sides. As muon tomography relies on reconstruction of the scattering angle, the key parameter for the detector system is the angular resolution of the upper and lower detector system. As such, a poor hit position resolution can be compensated for by increasing the distance between the measurement planes. That typically requires large area detectors. Due to cost reasons, these detector systems are either gaseous [14, 15]¹ or scintillation detectors see for example [16]. Several types of gaseous detectors are in use: resistive plate chambers (RPC), drift chambers and drift tubes are the most common. There are two types of scintillator-based detectors in common use. All aforementioned technologies provide large area detector systems with good performance for reasonable cost.

2.1 Imaging algorithms

All muon tomography imaging algorithms rely on the reconstruction of the scattering angle of the muon, see figure 2.2. They all differ in how the information is processed. In our work, we are building mainly on the Angle Statistics Reconstruction algorithm (ASR), see section 2.1.2, and the Binned Clustering algorithm (BC), see section 2.1.3.

¹ [15] is an output of the CHANCE project and can be found in Appendix A.1 as well.

2.1.1 PoCA

In the simplest approach, called the Point of Closest Approach (PoCA) algorithm, multiple scatterings of a muon are modelled as a single scattering at a single point ('scattering vertex'), see figure 2.2. The scattering vertex is found by extrapolating the incoming and outgoing tracks and searching for a point at which the distance between them is minimal.

To obtain a 3D image, the scanned volume is divided into cubic voxels. The number of scattering vertices and the scattering angle reconstructed in each voxel depends on the radiation length of the material in that voxel. Thus, analysis of the density of scattering vertices, their distribution and distribution of a scattering angle provide means to discriminate between material with different atomic number Z .

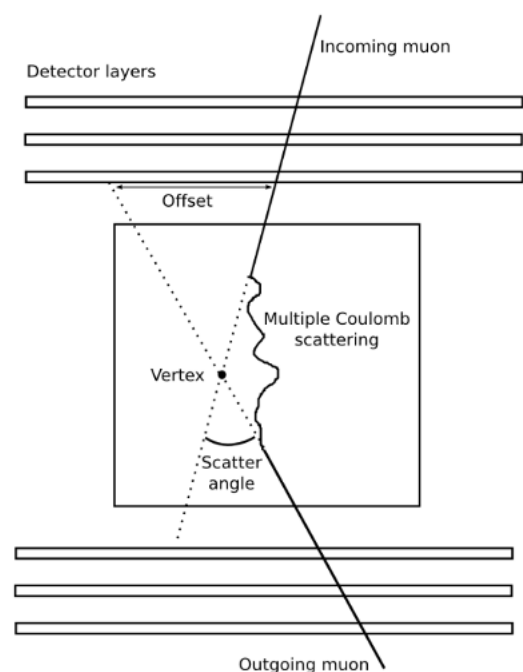


Figure 2.2: Illustration of scattering vertex reconstruction of a muon.

In the PoCA algorithm, the image is obtained as a 3D density map of the scattering vertices, sometimes weighted by a value of scattering angle. Such an approach is simple, but it suffers from intrinsic noise due to single-scattering-point approximation.

2.1.1 Angle Statistics Reconstruction Algorithm

Unlike the PoCA method, the ASR algorithm [17] assumes that when a muon travels through the 3D voxel grid, it is likely to experience many small scatters. The ASR thus avoids the underlying assumption of the PoCA algorithm that a muon only scatters inside a single vertex. The Angle Statistics Reconstruction (ASR) algorithm was developed to mitigate the effects of using the PoCA method's inaccurate approximation of the muon trajectories. This has been achieved by applying a minimum

chosen distance (D_r) between the reconstructed muon trajectories and the centre (c) of a voxel, therefore only voxels that lie within the chosen distance are considered. Any voxel that is located beyond the chosen distance D_r will be neglected. The minimum distance is determined by

$$D_r = \max(\min(|a(z) - c|), \min(|b(z) - c|)) \quad (2.3)$$

where $a(z)$ and $b(z)$ represent the fitted trajectories of the incoming and the outgoing muons, respectively. A threshold distance of (d_{th}) is chosen, ideally it is the same size as a voxel so that all voxels that have $D_r < d_{th}$ will be assigned a discriminator score. For each voxel and each muon with momentum of (p), the projected scattering angles on the x-axis and y-axis (θ_x and θ_y , respectively) are used to generate two scores $S_1 = (|\theta_x| \tilde{p})$ and $S_2 = (|\theta_y| \tilde{p})$ where \tilde{p} is the muon's momentum according to $\tilde{p} = \frac{p}{p_{norm}}$ where $p_{norm} = 3$ GeV. This is repeated for all muons passing through the object of interest resulting in a distribution of the S_1 and S_2 scores for each voxel. For each voxel the final distribution of scores is taken and an ASR discriminator score is assigned to be that of the third quartile (0.75) of the distribution and this value will be referred to as the ASR discriminator. These final discriminator scores are subsequently used to locate voxels in which high-Z materials might be present.

2.1.3 Binned clustering algorithm

In our studies, we developed more advanced methods, based on the Binned Clustering (BC) algorithm [5]. It builds on PoCA and exploits the spatial density of scattering vertices to improve image resolution and quality.

The Binned Clustering algorithm employs spatial density of large scattering vertices to discriminate between materials of different densities. In denser materials large angle scatters occur more often, hence the density of high angle scatters is higher.

The principle of the BC method is as follows:

1. The volume is divided into voxels (for instance cubes of side length 1 cm) and location of muon scattering vertices is calculated within each voxel.
2. Within each voxel, scattering vertices are sorted into descending order by the scattering angle. The first n entries in the list are kept and the rest discarded. Voxels with less than predefined value of n scattering vertices are discarded.
3. For each pair of vertices i, j in each voxel, a metric value $m_{i,j}$ is calculated as

$$m_{i,j} = \frac{|v_i - v_j|}{p_i \theta_i p_j \theta_j} \quad (2.4)$$

Where v_i , θ_i and p_i are respectively, the scattering vertex position, scattering angle, and momentum of muon i . Then, $|v_i - v_j|$ is a metric distance between vertex i and j .

For high-Z materials the density of the scattering vertices is higher (this the distance between voxels is shorter) and scattering angles are larger thus the metric value is lower. The original BC method uses median of the $\ln(m_{i,j})$ distribution in a voxel as a material-discriminating variable. In our studies, we adopted slightly modified definitions of the discriminator to maximize performance for low-Z and high-Z object identification.

3. Muon tomography detector system

In CHANCE it was chosen to produce a system based on both Resistive Plate Chambers (RPCs) and Drift Chambers. The design is shown in figure 3.1. There is a lot of expertise on RPCs and drift chambers at both the University of Bristol and the University of Sheffield, see for example [18, 19, 20]. Details are given in CHANCE Deliverable 4.1.

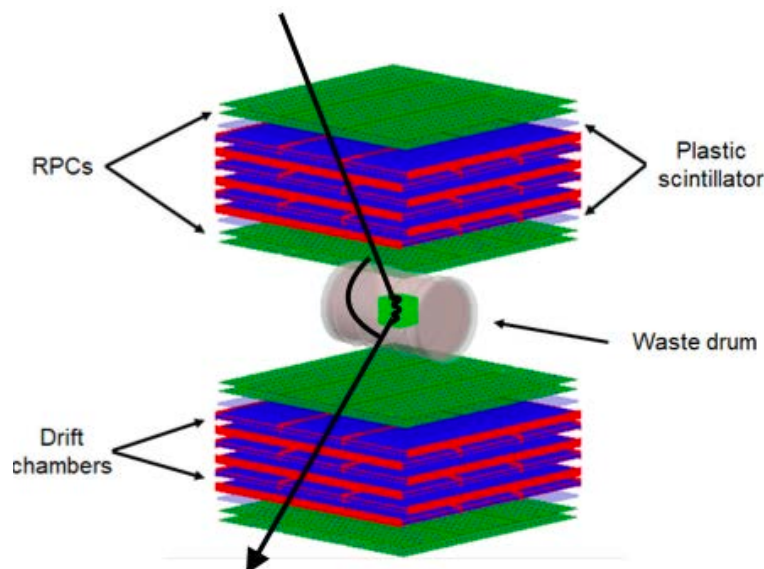


Figure 3.1: The design of CHANCE MST detector with an example of a muon showing the angle between the incoming and outgoing direction.

The system consists of 30 Resistive Plate Chambers (RPCs), see section 3.2 for details, 18 Drift Chambers, see section 3.3 for details and trigger panels, see section 3.1 for details. The panels are located in two perpendicular orientations, namely X and Y: each orientation detects hits in the (X, Z) and (Y, Z) planes, respectively, together forming a 3D track. It was chosen to operate the detector in a non-laboratory environment. The detector is hosted at the Fenswood Farm, 5 miles south-west of Bristol, UK.

During the project, there were 2 different experimental configurations used. **Configuration A** corresponds to trigger panels, drift chambers and 4 layers of RPCs, and **Configuration B** consists of trigger panels, drift chambers and 5 layers of RPCs. Figure 3.2 (left) shows the Configuration A of the system, while Configuration B is presented in Figure 3.2 (right). Figure 3.2 (right) also shows a mock-up drum during the experimental program. The 300 L drum has a diameter of approximately 66 cm and a length of 88 cm, and it was positioned in the center of CHANCE muon tomograph system.

3.1 Trigger system

Both of the tracking subsystems of the CHANCE detector require an external trigger to know when the muon crossed through the detector and initiate a readout cycle. This is especially important for the drift chamber subsystem as it is used in time of arrival calculations.



Figure 3.2: The CHANCE detector at Fenswood Farm in the first barn (configuration A) and the second barn (configuration B).

To provide an external trigger to the CHANCE subsystems, two scintillator trigger paddles are used. As shown in figure 3.3, they comprise of 300 20 cm×20 cm injection moulded plastic scintillator tiles arranged to form a 200×200 cm scintillating trigger paddle. To provide a reliable trigger for muons that have passed through the muon tracking subsystems, and reject background noise, a coincidence discriminator unit is used to ensure that both scintillator paddles are triggered within a short timing window. This coincidence discriminator is provided by a unit developed by the University of Bristol. The trigger signal is issued to each of the separate tracking subsystems. In addition to this basic

coincidence logic, busy signals are provided by the RPC and drift subsystems so that no trigger signals are issued whilst either subsystem is busy, helping to synchronise the trigger event indices between the two subsystems. The coincidence detection rate for the system is approximately 40 Hz during normal operation.



Figure 3.3: Single scintillator trigger paddle consisting of layers of scintillating tiles readout with wavelength shifting fibres.

3.1 RPC system

An RPC essentially consists of a chamber filled with gas under a high voltage (HV). When a charged particle traverses the gap chamber, ionisation takes place. Under the influence of the high voltage, a current pulse is produced. This induces a signal on pick up strips on the outside of the sensor. These signals are read out to detect the particle and reconstruct where it traversed the detector. An image of a single RPC is shown in figure 3.4. Figure 3.5 shows an RPC layer inside the CHANCE system.



Figure 3.4: Exploded view of an RPC (left) and an assembled RPC (right).

The large chambers were manufactured by an external glass company and tested in our laboratories to ensure that they all passed minimum quality criteria. The top and bottom surfaces of the RPCs are coated with conductive paint, Statguard Conductive Acrylic Paint, to create a thin film with surface resistivity of $105\Omega/m^2$. The film is used to create a uniform electric field within the gas cavity by applying HV to it. Two sheets of 1 mm thick PETG are glued to the RPCs to insulate the HV planes. Each RPC is mounted on an aluminium tray to increase its mechanical rigidity. The trays are designed to be slid in position on a larger mechanical support and to host the front-end electronic boards.

A single PCB with 1.68 mm pitch readout strips is glued on the top of each RPC. 320 strips run along the length of the PCB and are read out by a single board [21], designed in Bristol, which digitizes their signal and transmits them to the DAQ. Each board hosts five MAROC readout chips [22], each one connected to 64 strips. When a trigger signal is received, see chapter 3.1, the inputs are digitized using the 12-bit Wilkinsons converters built in each MAROC and the samples are stored in a buffer to be read by the DAQ system. The trigger signals are distributed via HDMI. The communication between DAQ and front-end boards is based on the IPBus protocol [23] and is performed using a standard giga-Ethernet connection. The RPC data acquisition software is written in Labview[24]. It reads the data from each RPC and stores it in a binary format. The RPC panels are powered by a high voltage power supply, applying a maximum of $\pm 5kV$ to each side. Each readout board is powered by a dedicated low voltage power supply. For each trigger the RPCs are read out, the signals of all strips stored and the data is analysed off-line.

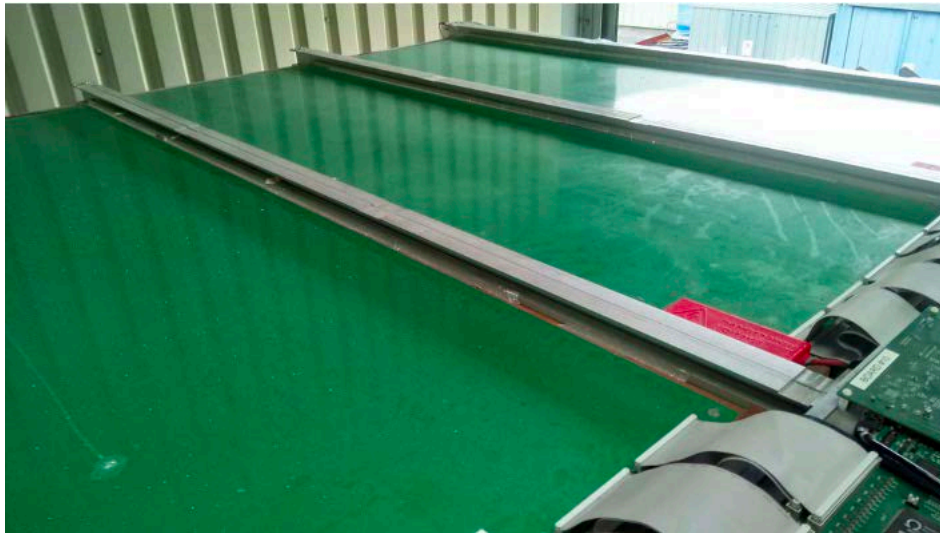


Figure 3.5: An RPC layer inside the CHANCE system.

3.1.1 RPC drift gas

These systems have achieved spatial resolutions better than 500mm and efficiency above 95% when flushed at a rate of 25 ml/min with a mixture of Tetrafluoroethane R-134a (95%) and Iso-butane (5%) at a pressure of about 500 Pa (2 inches of water) above the atmospheric pressure [18]. R-134a is a very good gas for RPCs. In R-134a on average 81.6 electron-ion pairs are produced per mm as primary ionisation [25]. The primary electrons then undergo multiplication processes to generate the signal. Unfortunately, R-134a is very bad for global warming. Due to stricter environmental regulations coming into force during the CHANCE project, we were forbidden from using R-134a. It became impossible to buy R-134a in the UK without a special permit, which we did not get. To keep using R-134a would require the installation of an abatement system. We requested an informal quote for such a system, which was around £200,000. We did not have the budget to buy such a system. In addition, it would have required significant works on site and it was not clear we would be able/allowed to install such a system.

As we could no longer use R-134a, it was decided to switch to CO₂ instead. CO₂ only has an average of 35.5 electron-ion pairs produced per mm as primary ionisation and 91 electron-ion pairs are produced per mm in total [26]. There are many RPC systems that successfully operate with CO₂. As such the signal in the CO₂ filled RPCs is much lower (around 5–10 times) than expected when designing the system, which lowers the hit efficiency dramatically. To get a good efficiency with CO₂ requires a combination of either a thicker gap, so more total ionisation takes place, and/or a larger electric field and thus a much higher high voltage. This problem is not unique to us. Many groups and systems operated around the world have encountered the same problems. There is a lot of work being done trying to find environmentally friendly and affordable alternatives, see for example [25, 27, 28, 29], but they are not (yet) available at a price and bottle size that made using it viable. As a result, we had to decide to increase the RPC voltage as much as we could and accept the lower efficiency in the hope that a better alternative became available soon.

Meanwhile a new environmentally friendly alternative has been discovered. The paper [30] appeared in December 2021 on ArXiv. In order to use this gas, we would still need to apply for a permit to use it, which takes about three months. In addition, BOC (our gas supplier) cannot deliver these gasses at the moment as they temporarily only fulfil existing contracts due to staff shortages.

3.1.2 RPC data

When a coincidence trigger arrives, RPC events are written to disk. The data are subsequently processed.

Events are selected based on timestamps: all timestamps occurring in a data file are scanned and corrected, see section 3.2.2. The occurrences of each timestamp are counted, and only events with a minimum of 3 hits detected by different boards are processed.

The process is composed of different steps, including consecutive and more accurate estimation for the average signal (pedestal) and the background noise:

- Average signal and standard deviation, representing a first estimation of pedestal and noise, are calculated using all the events recorded by each board.
- Using the first estimation of noise and pedestal, hits are found as signal exceeding $pedestal + 4 * noise$
- Since the presence of a hit causes pedestal over estimation and poor noise calculation, hits found in the previous step are excluded, and a second estimation for noise and pedestal is evaluated.
- Hit finder is run again using the second estimation, and hits are excluded. Pedestal is subtracted from the signal, and “common mode” is calculated as the average signal in each MAROC, and corrected in the pedestal-subtracted signal; the resulting signal baseline should at this point be around 0. The last estimation of the noise is performed
- After pedestal and common mode subtraction, hits are found as signal exceeding $4 * noise$. For each hit, maximum position, start and stop coordinates are stored.

The pipeline can be summarised as follows:

1. first estimation of pedestal and noise item hit exclusion and second pedestal and noise estimation
2. hit detection, pedestal subtraction, common mode correction
3. final noise calculation
4. final hit detection

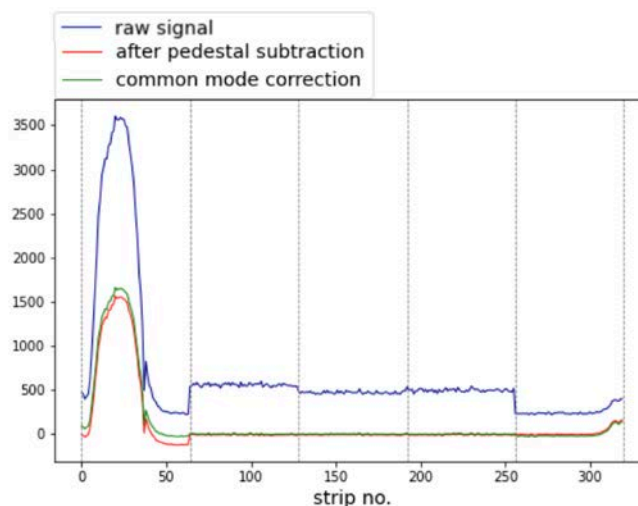


Figure 3.6: An event at different stages in the data processing pipeline.

Figure 3.6 shows an example of a detected hit, during three different stages of the pipeline. Some corrections are needed before applying the hit finding pipeline, and are described in the following sections.

Timestamp corrections

Timestamps are encoded in the int-32 format, starting from a random small non-zero value. A few consecutive corrections are applied to obtain compatible timestamps from all the readout boards.

First event correction

Sometimes, the first event recorded by each readout board is a random value, incompatible with what recorded by the other readout boards. When this happens, the event ID is also different from the expected value (usually 0 or 1). In this case, the first event in the board is skipped, and all event IDs are shifted back to 0. Figure 3.7 shows a zoomed plot of timestamps as a function of the event ID, to draw the attention on the first events, where the issue occurs. While the raw timestamps saved in the files are not exactly the same for all the readout boards, the time difference between each recorded event is the same. To compare timestamps occurring in each readout board, all remaining events, after skipping the first one, are brought to a common start by subtracting the first timestamp. Resulting “corrected timestamps” are now comparable, and differ by ± 1 or ± 2 at most.

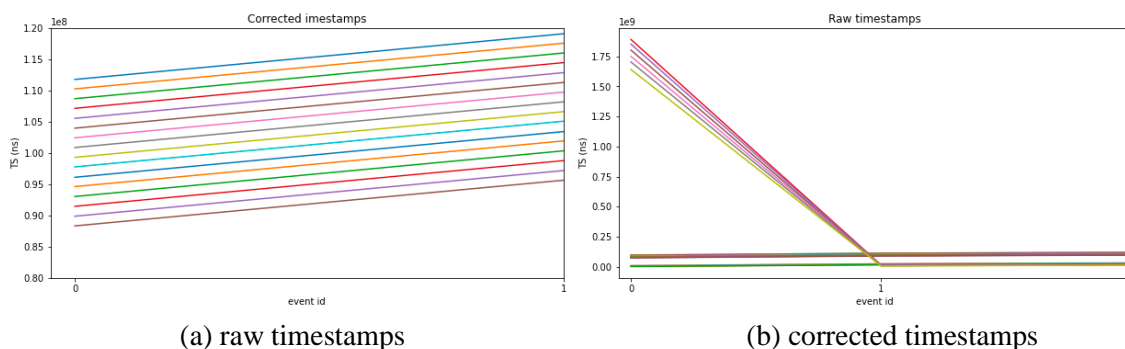


Figure 3.7: Timestamps before first event correction (left) and after skipping the first event (right), showing only the first events, where the issue occurs. Before applying the correction, some boards present a first event with a random high ID, while events from event ID=1 on are correct. After the correction, all events have a common start (event ID=0), and are compatible until the end.

Timestamp overflow correction

It often occurs that during data acquisition the timestamp value reaches 2^{32} , that is the maximum value that can be stored in that numerical representation. When this occurs, the following timestamps in the same data file roll over. After the restart, timestamps are not comparable anymore, as the starting point is different in each board. A second correction is applied, after converting the data to int-64, by adding multiples of the overflow 2^{32} .

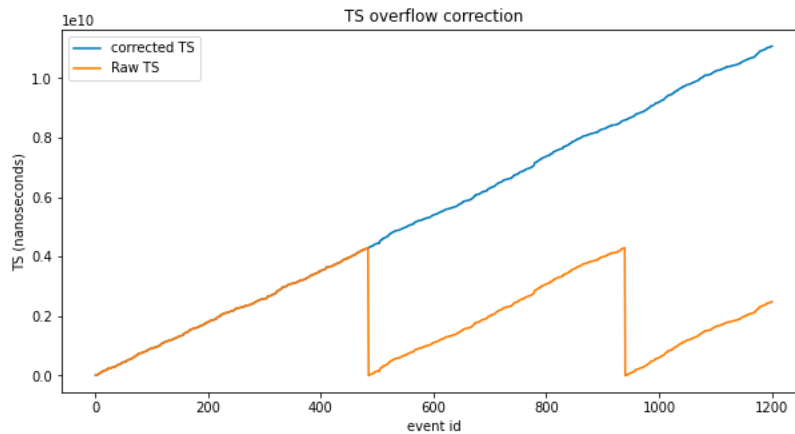


Figure 3.8: Timestamp overflow correction.

Signal overflow correction

The ADC signal is capped at 4096. When in an event the signal in ADC counts exceed that value, the signal for those strips is saved as 0. As this usually happens when a big hit occurs, a correction is needed to recover a hit that would otherwise be missed by the pipeline. A simple workaround is joining the top part of the peak, resulting in a square hit. This can be detected by the hit finder.

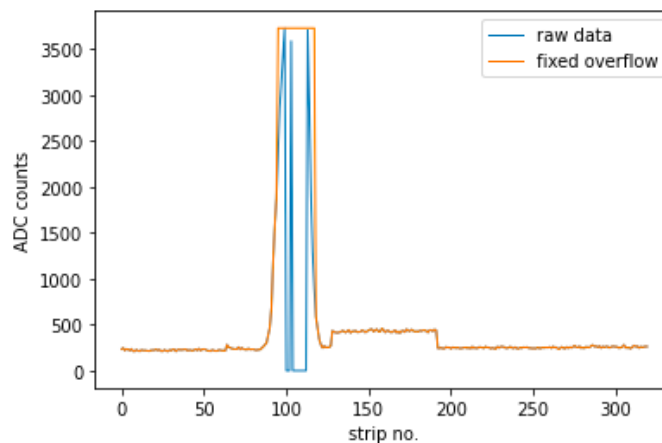


Figure 3.9: Signal overflow correction resulting in a square hit.

MAROC reordering

Some issues in the way MAROC chips are connected to the 64-strip blocks were found, which sometimes resulted in split and misplaced hits between two MAROCs. To solve this, the order in which data is processed from each MAROC is changed in the following way

$$(0, 1, 2, 3, 4) \rightarrow (0, 3, 4, 2, 1)$$

Resulting shift of signal hits can be seen in fig. 3.10. This improves the hits alignment in consecutive boards, as well as recovering split hits occurring at the edge of consecutive MAROCs.

3.1.3 Muon track reconstruction

Muon tracks are found by combining hits on consecutive layers. Hits that are found by the hit finding pipeline are then processed to search for muon tracks. Strip positions are converted to global coordinates (X, Z) and (Y, Z), using the size of each RPC, and their position in the detector. The tracking pipeline is:

- hits are collected in each event;
- global coordinates and layer id are calculated for every hit;
- if more than a given number of layers contain hits (usually 3), a global fit is calculated using all hits;
- if more hits occur on the same layers, all possible combinations of 1 hit in each layer are calculated; of all the global fits, the best, defined as the fit with the minimum chi-square is chosen as the final fit. The slope of the best fit is saved;
- if more than 4 layers contain hits, two local fits, namely top and bottom are calculated.

Figure 3.11 shows an example of a reconstructed track.

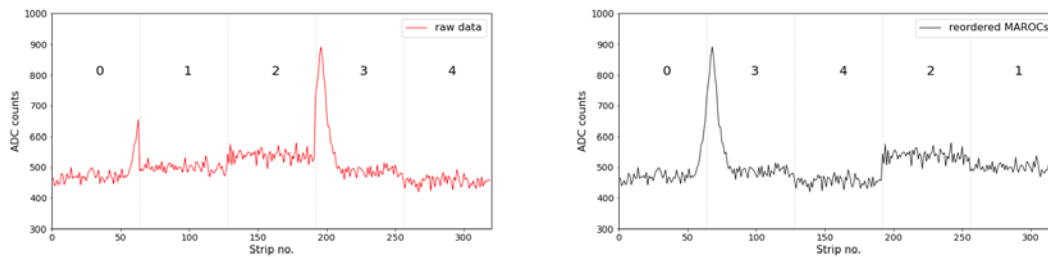


Figure 3.10: An event before and after the MAROC reordering. The reordering recovers a split hit.

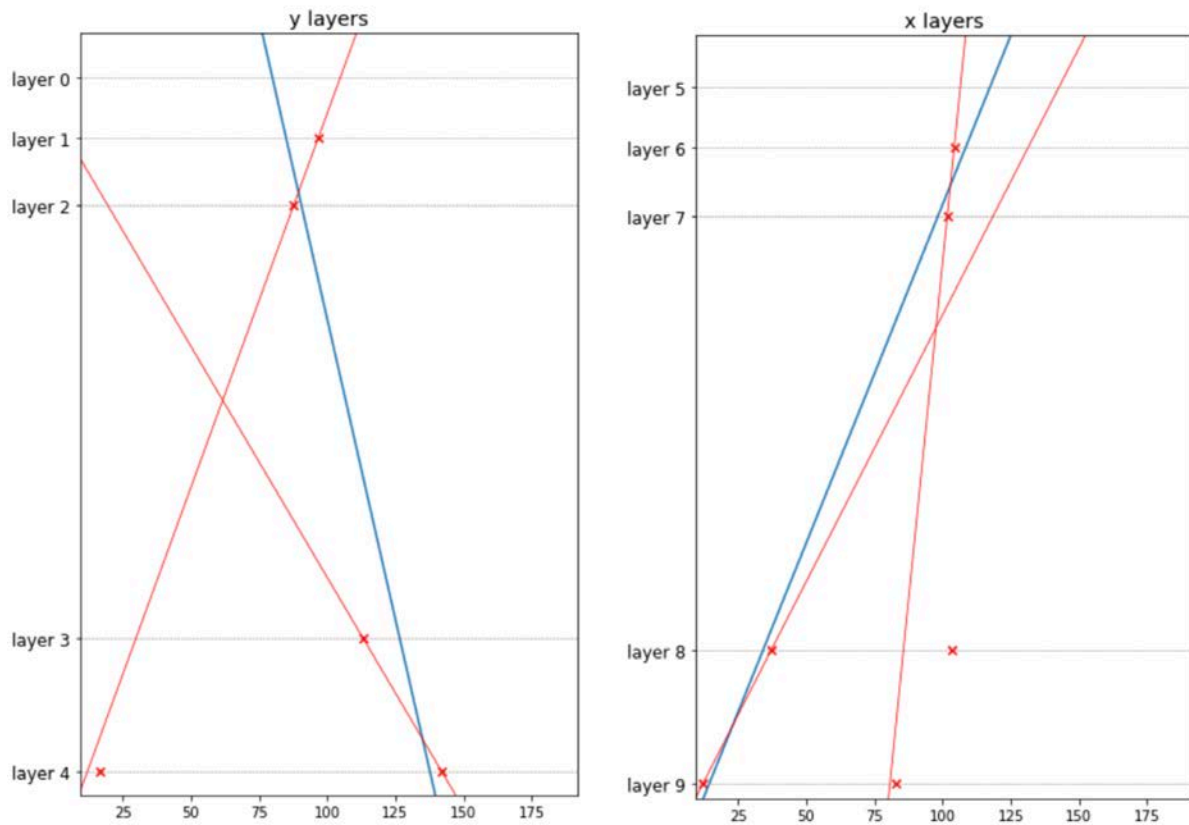


Figure 3.11: Example of a reconstructed track, for y layers (left) and x (layer), respectively. The blue lines are the global fits, calculated using all hits belonging to the "best track" (least χ^2), and the top and bottom tracks are shown in red.

3.1.4 RPC performance

Tracks obtained by the analysis pipeline are used to evaluate the detector tracking performance, and the efficiency of each panel by itself. For the results presented here, data collected in 8 months between June 2021 and February 2022 are used. Performance variables like the number of hits per track, the residual distribution

Number of hit layers per track

The muon track search starts if at least three different layers have hits. Ideally, good track contains a minimum of five hits, i.e. one per available layer. Around 10 thousand tracks were obtained in the analysed sample. Figure 3.12 shows the distribution of the number of hits per track. The graph shows that the system works well for the detectors in the y -direction, but there is an inefficient layer amongst the detectors in the x -direction. To perform tomography with RPCs only requires at least 4 hits in the xz and in the yz plane.

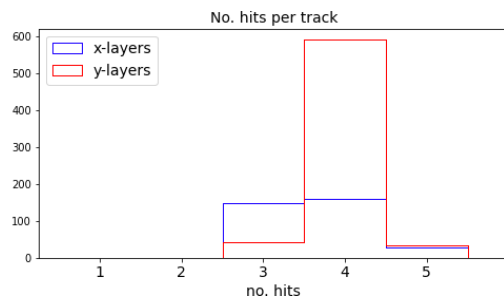


Figure 3.12: Distribution of the number of hits per reconstructed track. There are a few tracks with 5 hits, but most tracks have 4. Y-layers have the highest number of tracks.

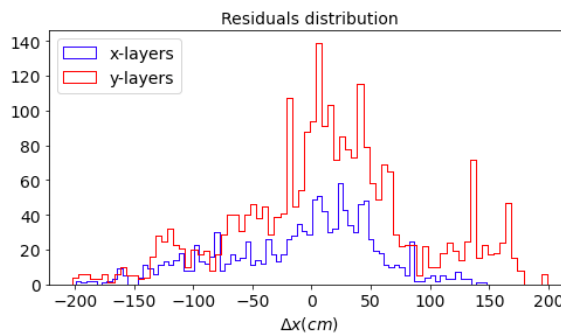


Figure 3.13: Distribution of the global fit residuals.

Residuals distribution

Residuals distributions are calculated to evaluate the how good the hit position reconstruction is. In the case of multiple hits occurring in the same layers, only the hits of the best fit are selected (i.e. the fit yielding the least χ^2). The results are shown in figure 3.13, confirming the better performance of the y -layers. However, the distribution is quite wide.

Signal-to-noise plots

In the absence of an external signal source, like cosmic muons, every strip yields an output that varies according to a Gaussian distribution around the pedestal of a strip. The standard deviation of the distribution is the noise of the strip. Hence, a distribution of A for all events where

$$A = \frac{\text{output}_{i,k} - \text{ped}_i}{\text{noise}_i} \quad (3.1)$$

where $\text{output}_{i,k}$ is the raw output of the strip i in event k and their respective pedestal and noise, a Gaussian with a mean of 0 and a standard deviation of 1 is obtained. The cosmic muons will add positive signals to several strips in each event. Plotting A for each MAROC shows whether the pedestal and noise are calculated correctly and show an excess on the positive side due to signals. Figure 3.14 shows examples of these plots for several RPCs. The graphs for e.g. board 8 show that for all 5 MAROCs the pedestal and noise have been calculated correctly. In addition, the large number of excess hits for MAROC 2 show that a large number of hits will be detected with a $> 5\sigma$ signal cut. On the other hand, board-1 and board-2 are examples of boards that did not collect many hits due to inefficiencies.

3.1.5 RPC performance summary

As shown here and will be shown in section 3.4.3, most of the RPCs are working well after solving some minor issues and implementing appropriate corrections. Unfortunately, the hit efficiency is low due to the use of CO₂ as the drift gas. CO₂ provides a signal 5–10 times lower than R-134a. This could only be recovered to a small extent by an increase in high voltage. We used the highest voltages possible below break down.

3.2 Drift Chambers

The CHANCE Drift Chamber tracking system provides a measurement of the muon trajectory below the region of interest by reconstructing the muon crossing position across 6 layers of drift planes. Each of these drift planes consists of three individual 60 cm×180 cm drift chambers placed next to one another to form a 180 cm×180cm detection plane.

3.2.1 Operating Principle

The 60 cm × 180 cm enclosed drift chambers used in the CHANCE detector allow the detection of a muon crossing position with approximately 2-3 mm resolution by measuring the time taken for ionisation electrons produced inside the chamber to drift to a centrally located anode wire. As shown in in figure 3.15, a cathode plane shapes the electric field in each chamber to produce a stable electric field up to 30 cm away from the anode wire. The gas volume inside each chamber is flushed with a mixture of 5% CO₂, 2.5% Methane, and 92.5% argon, which provides a stable drift velocity over a wide range of electric field strengths.

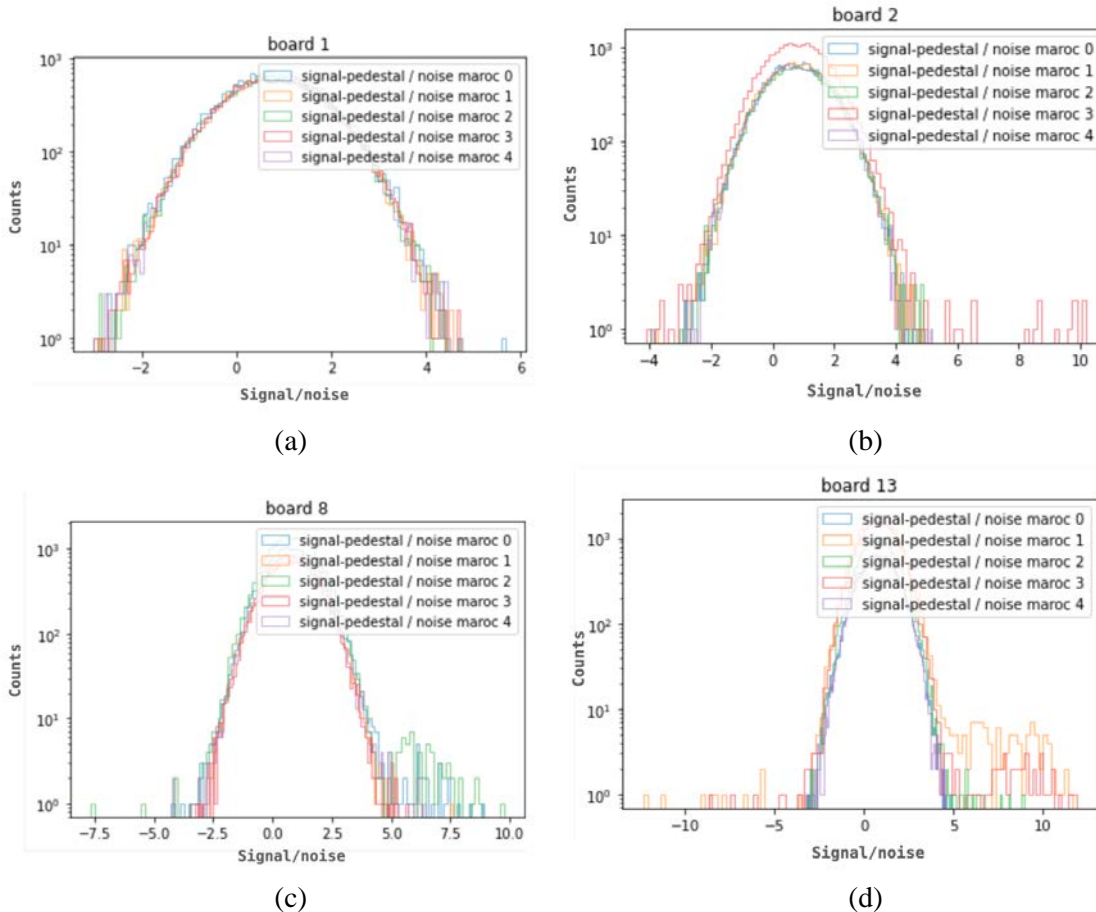


Figure 3.14: Signal-to-noise plots for four boards. (a-b) show cases with none or very few hits collected; (c-d) show well-behaving panels, where collected hits are the tail to the right of the distribution.

If the original time the muon crossed the chambers is known, for example from an external trigger, then the time difference between the crossing time and the time of arrival for the electron drift cloud, provides a process measurement of the crossing position. Each chamber has a built-in preamplifier circuit next to its high voltage feed throughs that converts the drift electron signal on the anode wire to a voltage output pulse.

Because of the long drift distances only a single readout channel is needed for a 60 cm wide chamber. This makes single wire drift chambers an economical way to instrument large area muon tracking systems. The two drawbacks in this long drift distance design is that oxygen ingress in each chamber needs to be kept to a minimum, and no information is available on whether the drift electrons came from the left or right side of the wire. This creates what is referred to as “ghost” hits in the chamber. This is corrected for by introducing a 3 cm offset between drift chamber layers on consecutive layers. This offset can be used to distinguish individual tracks as typically for muon candidate events only a single combination produces a valid straight line fit result. The track residual, the average distance between each hit identified hit and a straight line fit, is used to identify the combination of drift chamber hits

most likely to be due to a crossing muon. As shown in figure 3.16, due to the relative chamber offsets in the middle layer, only a single combination of hits produces a straight track pointing to the right with a low track residual. Without this offset, two tracks one pointing left and the other pointing right, would both be equally valid straight tracks with no possible way to discriminate which was the true muon trajectory.

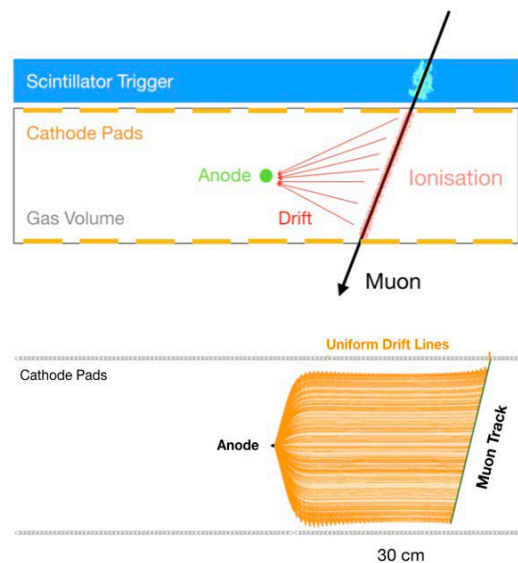


Figure 3.15: (Top) Drift chamber operating principle. Muons produce ionisation electrons inside the drift gas volume, which drift in a constant electric field to centrally located anode wire. The time taken to reach the anode wire, relative to an external scintillator trigger time, is used to infer the muons crossing position. (Bottom) Equally spaced cathode pads at voltages starting at 3800 V that drop with distance from the central anode, results in a uniform drift field with smooth drift lines leading toward the centre of the chamber.

3.2.2 Hit Position Finding

Event samples containing the maximum ADC value on each channel within the timing window need to be further processed to produce valid hit positions. Because the digitiser software saves the first time the maximum 12-bit ADC value occurs, there is a natural bias for noise hits due to baseline tinkle to occur at the start of the timing window as shown in the trigger time distribution in figure 3.18. The region of interest for the drift chamber readout shown in figure 3.18 is between samples 400 and 2000.

Additional data is taken outside of this region of interest during normal operation so that a baseline fit can be performed to determine the natural slope in the trigger time distribution and remove it.

The natural baseline ripple is also clear in the raw data in figure 3.18. This is corrected for by placing a cut on the minimum ADC value that constitutes a hit. This cut value is automatically placed 30 mV above the average baseline ADC value for each channel. Finally, cuts are placed on the minimum and

maximum time relative to the external trigger, to reject drift events that should not be associated with the given trigger due to noise or back-ground pileup. As shown in figure 3.18, the addition of these cuts produces a corrected timing distribution with a flat timing distribution corresponding to a uniform drift velocity when moving away from the anode wire.

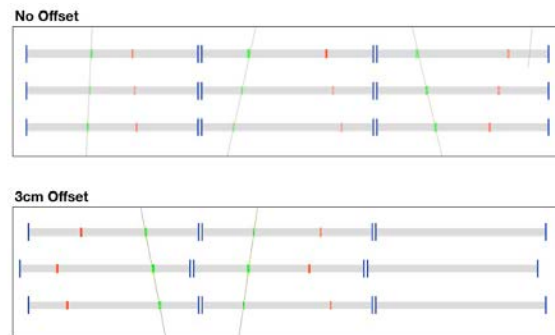


Figure 3.16: Track reconstruction example for a drift chamber subsystem. The true (green) and ghost (red) hit positions are shown for example MC simulation events. As shown in the top figure, without any chamber offset, based on the hit positions alone there is no way to distinguish which is the true muon trajectory. As shown in the bottom figure the introduction of a 3cm middle layer offset allows the tracking residual to be used to distinguish the true muon trajectory by looking for a straight line fit.

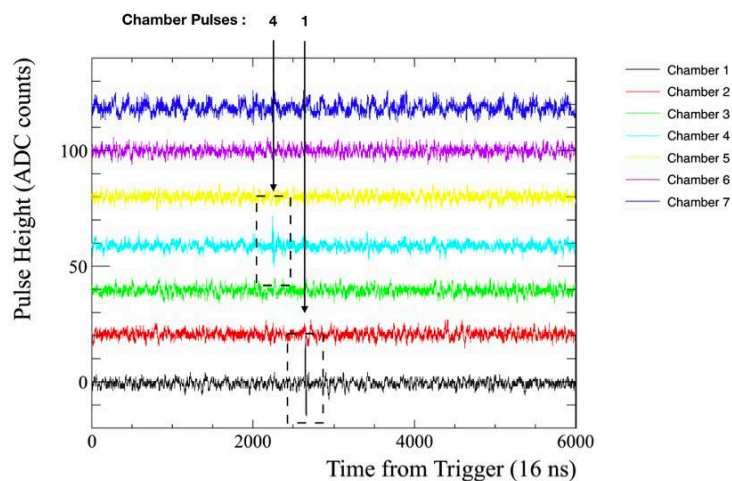


Figure 3.17: Example pulses from seven of the individual drift chambers. Chambers 1 and 4 (directly above one another), have both triggered at slightly different times, likely due to a high angle track. Given the large timing window necessary to readout each chamber, it is not feasible to save the entire 6000 sample long pulse for each event.

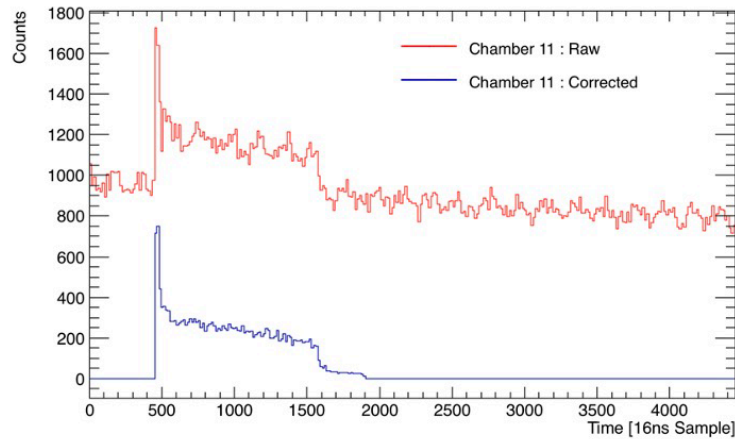


Figure 3.18: Drift chamber timing distributions before and after baseline and maximum ADC value corrections.

After these corrections, hit positions are obtained by simply multiplying the drift time (the time of each triggered channel relative to the external trigger time), by the chamber drift velocity, 0.0126 cm/ns. This velocity is obtained empirically from the data for each chamber, by looking at the maximum drift time obtained during normal operation and averaging across all chambers. Example converted drift positions obtained for one chamber are shown in figure 3.19. The final distribution is a flat distribution extending out to ± 33 cm away from the anode wire. It is exactly symmetric due to the lack of knowledge of whether any hit occurred on the left or right side.

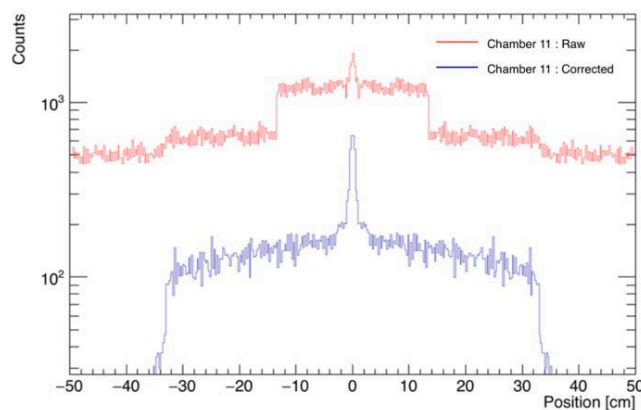


Figure 3.19: Drift chamber timing distributions before and after baseline and maximum ADC value corrections.

As discussed earlier, following the conversion of drift times into possible hit positions, an additional tracking residual cut is then needed to determine the true muon trajectory. Figure 3.20 shows an example of one of these track fits for real data, with chamber positions overlaid on top.

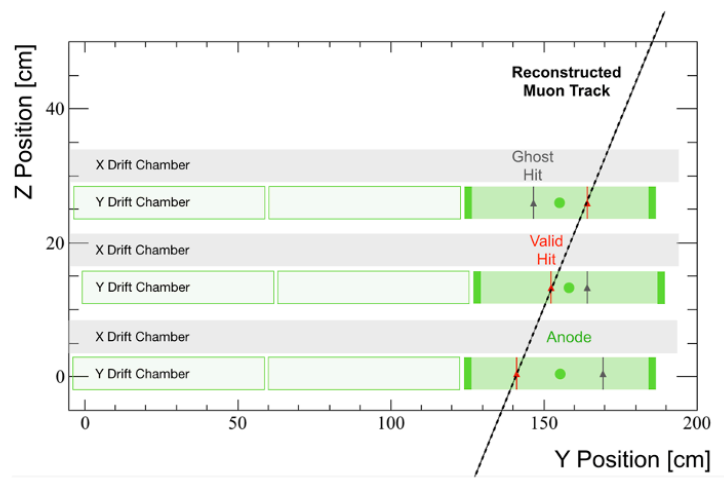


Figure 3.20: Track reconstruction example for the drift chamber subsystem. The valid and ghost hit positions are taken from an example event in the real system data. The extent of each chamber and approximate location of its anode wire has been overlaid on top. The combination of hits highlighted in red are the only ones that have an average track residual less than 3 mm.

3.2.3 Deployment issues

After our initial commissioning phase, a drift chamber plane in the bottom half of the system developed a problem. It was decided to replace this layer by a new drift chamber. This new layer first needed to be produced and then installed.

Later on, a drift chamber layer in the top part of the system developed problems. It was decided not to replace it by another drift chamber but by another layer of RPCs. This caused delay as the RPCs needed to be produced from the bare glass RPCs. The installation of the layer was delayed as the connectors were not available due to Brexit. When they became available, installation was not allowed as the country was in lock down and Covid access restrictions applied. In the final operational phase of the system, data was taking with 5 layers of RPCs and one drift chamber. The choice was mainly motivated by the need to get the system up and running again as soon as possible. At the time, the drift chamber experts from the University of Sheffield were not allowed to travel to Bristol due to UK government Covid-19 policy. As such, we had no alternative. It would have been more beneficial to replace the drift chamber by another drift chamber if we could have been sure that the experts could visit the system to install the new drift chamber.

3.3 Global Tracking

Due to differences in the control software between the RPC and Drift Chamber subsystems data acquisition is kept separate up until the global matching and track fit stage. Data is obtained independently from both systems, with their trigger indices are kept approximately synchronised by sharing a common global trigger from the discriminator unit. This allows an additional data processing stage to be run offline to match up the data from both subsystems before reconstructing global tracks of the muons trajectory above and below the imaging volume. The offline process is split into 3 stages; trigger matching, locale track fitting, final global point-of-closest approach calculation.

3.3.1 Event Trigger Matching

The global trigger system keeps the total event count between the RPC and Drift System approximately synchronised, however due to unexpected delays in data acquisition occasionally either system can miss a global trigger input. Most commonly this occurs due to a reconfiguring of the RPC front end boards after each new data file. This problem is less common for the drift subsystem, since the front ends of the drift chambers are analogue only and the data acquisition of the drift chamber system is performed on a single 32 channel event buffering digitiser. The trade-off between the two is that the drift chamber system is far less portable and reconfigurable than the RPC system due to lack of integrated front end boards.

Build up of trigger “misses” on either system due to unsynchronised dead time result in a gradual drift in the trigger count on the drift chamber system relative to the RPC system that must be corrected for. This is possible by recognising that aside from regions where the system is in an unsynchronised dead time state, the time difference between two consecutive triggers inputs should be the same on both subsystems. Therefore, if graphs of the time differences between triggers are created for small subsets of the RPC event sample (typically 100 events), it is possible to find a matching timing graph within the Drift Chamber event sample. These timing graphs are referred to as “timestamp signatures”, and are shown in figure 3.21.

An automated timestamp signature matching procedure has been developed that can reliably match the trigger indices between the RPC and Drift Chamber Systems and output combined hit position data for further processing. The trigger matching efficiency is found to be 96.4%, where the 4% drop in efficiency comes from missed events at the start or end of the RPC data stream due to unsynchronised system dead time.

3.3.1 Global Track Fitting

Global Track fitting is performed in a similar fashion to each subsystems individual track fitting. First hits are divide into corresponding “locales”. These are top-X, top-Y, bot-tom-X, and bottom-Y respectively. An individual track fit is then performed in each of these locales to obtain the 1D track gradient and vertical offset, before these are merged to form a 3D muon trajectory above and below the

imaging volume. Whilst a global track fit could be performed in 3D space to try to obtain a scattering point within the imaging volume, this split-locale approach allows us to also consider events that may have formed a valid track in 2 of the 4 locales and attempt to use this information to improve the speed at which a useful imaging data set could be obtained.

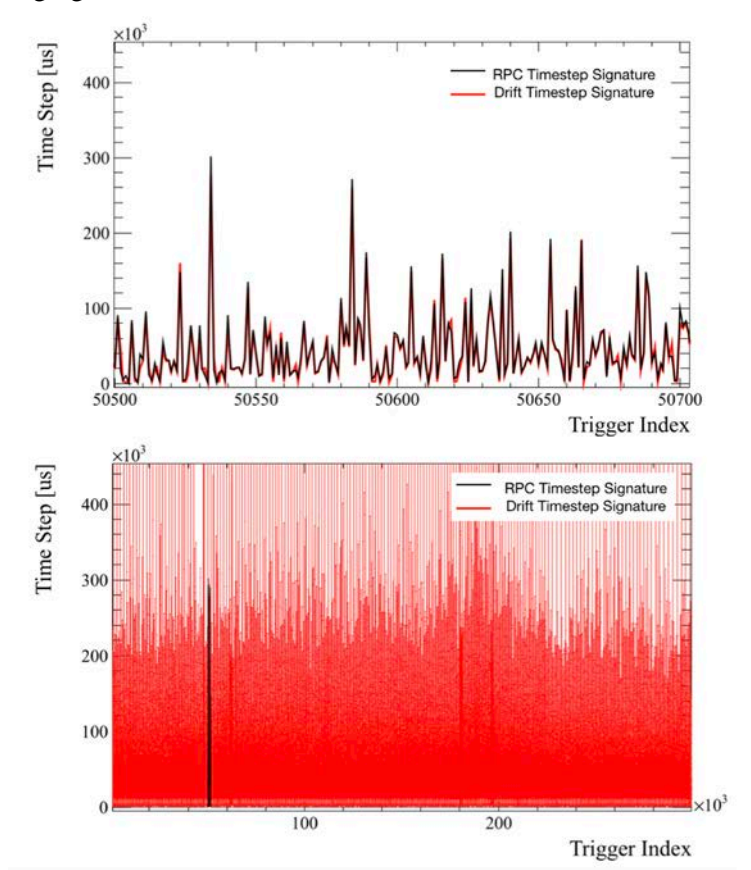


Figure 3.21: (Top) Example time step signature for a small sample of RPC events showing the correspondence obtained when the trigger indices are in sync. (Bottom) Trigger synchronisation is achieved by scanning all possible trigger indices within a drift chamber output file and finding where the RPC time step signature closely matches.

For the top-X, top-Y, locales, only a two RPC layers are present, therefore the track fit is a simple straight line approximation between the obtained hit positions within each log-scale. The bottom-X and Y locale track fit is slightly more complicated due to the inclusion of three additional drift chamber layers. Inclusion of these layers is important as the drift chambers in the bottom-Y locale provide additional 3-point tracking information, allowing a confirmation that the detected tracks are indeed due to a crossing muon. Since the drift chambers provide two possible hit positions (a normal and a “ghost” hit), the trackfit must consider all possible hit combinations for the bottom-X locale before choosing a track with a tracking residual less than a chosen threshold.

3.3.2 Implementation

We developed the global track fit at the beginning of the project, when we were expecting to run with R-134a for the RPCs and thus a large amount of good tracks. After installation of the system and suffering from the R-134a ban, see section 3.2.1, our efficiency was lower than expected. In addition, the drift chambers developed issues and in the end one was replaced by an additional RPC layer, see section 3.3.3.

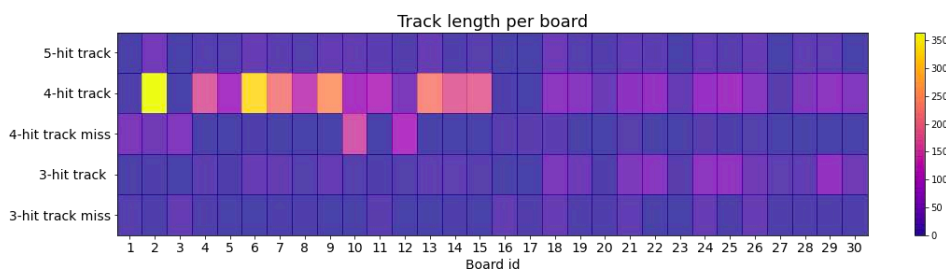


Figure 3.22: Heatmap showing for each board the length of the track it belongs to. Most tracks have 4 hits, and the Y layers have a higher detection efficiency than the X ones. Missing hits are also shown in the 5-hit track and 4-hit tracks case.

Around that time, we identified the RPC timing issue, see section 3.2.2. After solving that and the fifth RPC layer was installed, it was more practical to perform tracking with initially the RPC system only and later on combine the drift chamber information. Figure 3.22 shows an overview of the tracking performance for each RPC. It shows for each RPC how often it was part of a full 5 hit track, how often it was part of a 4 hit track, how often it was missing on an otherwise good 4 hit track, how often it was part of a 3 hit track, how often it was missing on an otherwise good a 3 hit track. Ideally, all RPCs are only part of good 5 hits tracks, but this is clearly not the case. Some RPCs are not responding well and are not often recording a hit, for example RPC 16 and 17, while RPC 2, 6 & 7 are showing a lot of hits on 4 hit tracks. The results indicate that we have recorded a small but good sample of tracks, but also that there are parts of the detector system that do not provide (many) hits.

3.4 Experimental Programme Challenges

As reported during the reporting cycle, we have experienced several major challenges severely affecting our experimental programme. We have tried to mitigate their effects to the best of our abilities and pushed to get the best possible results out of the system before the end of the project. Unfortunately, we were not successful and have only managed to obtain a small sample of muon tracks.

We have reported the causes for our delays and difficulties in the CHANCE progress reports. Here is an overview of the key challenges.

- Our foremost problem with the RPC system was the change in environmental regulations preventing us from using Freon, see section 3.2.1. This change in legislation only became apparent after the start of the programme. Freon is an excellent gas for RPCs. When running

our pre-CHANCE prototype with Freon, chamber efficiencies of well over 95% were obtained, see chapter 3.2. Freon yields on average 81.6 electron-ion pairs are produced per mm as primary ionisation, which then multiply while travelling through the gas gap. We needed to switch to CO₂ which only has an average of 35.5 electron-ion pairs are produced per mm as primary ionisation and 91 electron-ion pairs are produced per mm in total. This results in most probable signal of a factor 5 – 10 lower than when using Freon and thus a major decrease in efficiency. Other allowed gasses have similar performance to CO₂. To get a permit to run with Freon would have required the purchase of an abatement system. We requested an indicative quote and the price was close to £200,000. We could not afford to buy this system. The lower efficiency is the thing that harmed our experimental programme most. Ideal tracks that have recorded hits in all 12 layers (6 in the *xz* and 6 in the *yz* plane) are rare if the efficiency is small. The fraction of tracks that has hits in all 10 RPC layers is given by ε^{10} , where ε is the efficiency. Clearly, unless the efficiency of all planes is very high, very few muon tracks will be recorded, as indicated in the tableau below.

ε (%)	Track fraction (%)
99	90.4
98	81.7
95	59.9
90	34.9
80	10.7
70	2.8
50	0.98

Clearly, unless the efficiency of all planes is very high, very few muon tracks will be recorded.

- Initially, we suffered delays to get Health & Safety approval for our system as installed in the barn. There were questions about the strength of the mechanical supports and the safety of the high voltage system. The mechanical structure was deployed for a similar system before but came without the required paperwork. The design for our high voltage system was used before at the University of Bristol for our pre-CHANCE prototype system. Nevertheless, it took weeks before we got approval to turn on the system.
- After our initial commissioning phase, a drift chamber plane developed a problem. It was decided to replace this layer by a new drift chamber. This new layer first needed to be produced and then installed.
- The photomultiplier tubes were found to have a low efficiency and were replaced.
- The system was installed in a grain barn at Fenswood farm. During CHANCE the system needed to be moved from the grain barn to the main barn. This meant disassembling the system and reinstalling and recommissioning it. This took 2–3 months.
- A high voltage power supply module for the RPC system broke. Replacing this took 10 weeks.
- Key staff left during the project, in particular the PDRAs Dr Kopp, Dr Stowell and Dr Barker. A key responsibility of Dr Kopp's was to keep the system running. Dr Kopp left during the first

UK lockdown of the Covid crisis. The University of Bristol had a hiring stop. As such it took a few months to replace Dr Kopp. Dr Stowell was the expert for the drift chamber system and analysis. He was replaced by Dr Barker, who left later on in the project.

- During the Covid lock downs staff from the University of Bristol had permission to keep the system running, but we were not allowed to do significant amounts of work on the system and were not allowed in the building where the spare parts were located. The University of Sheffield staff was not allowed to attend the system at all. This led to significant delays as we could not fix and optimise minor issues.
- A drift chamber layer developed problems. It was decided not to replace it by another drift chamber but by another layer of RPCs. This caused delay as the RPCs needed to be produced from the bare glass RPCs. The installation of the layer was delayed as the connectors were not available due to Brexit. When they became available, installation was not allowed as the country was in lock down and Covid access restrictions applied. The choice was mainly motivated by the need to get the system up and running again as soon as possible. At the time, the drift chamber experts from the University of Sheffield were not allowed to travel to Bristol due to UK government Covid-19 policy. As such, we had no alternative. It would have been more beneficial to replace the drift chamber by another drift chamber if we could have been sure that the experts could visit the system to install the new drift chamber.
- We discovered a feature in the time stamping of the RPC data, see section 3.2.2, quite late on in the project. This feature did not affect data taking with our pre-CHANCE RPC system. In that system we relied on the trigger number, which was the same for each RPC. Hence, the RPC events in different RPCs were always combined correctly. To merge the data with the drift chambers required usage of the actual time stamp, which showed the feature.

Despite suffering these issues, we did build and operate a muon tomography system consisting of RPCs and drift chambers as planned in the proposal. Our main issues: the R-134a ban, the Covid pandemic with all travel and staff operations issues and Brexit related problems, could not have been foreseen at the start of the projects. These have made the practical part of the project extremely challenging, but we did manage to deliver a working system.

3.5 Experimental results

As indicated in the beginning of section 3, 2 different experimental configurations were used. Configuration A corresponds to trigger panels, drift chambers and 4 layers of RPCs, and Configuration B consists of trigger panels, drift chambers and 5 layers of RPCs. Figure 3.2 (left) shows the Configuration A of the system, while Configuration B is presented in Figure 3.2 (right). Figure 3.2(right) also shows a 300L mock-up drum during the experimental program.

To quantify the system's performance in a size and position reconstruction and quality of the material identification, we placed objects of known material inside the measurement area during the data-taking

campaign. We used blocks of lead, tungsten, steel, and aluminium; each of them had a size of approximately $54 \times 5 \times 5 \text{ cm}^3$, and were located alongside the mock-up drum.

We analyzed experimental data separately for Configuration A and B of the CHANCE muon systems. A more extensive report on the results can be found in Deliverable 4.3. We started with a simple PoCA method, see section 2.1.1, where the scattering points were reconstructed independently in XZ and YZ planes. The scattering vertex is taken as an intersection of two tracks registered in the top and the bottom parts of the system. Each of these tracks is reconstructed independently in XZ or YZ plane. We required at least two hits in the top or bottom detector for each track, respectively. The image is then created as a density map of the PoCA scattering vertices within the CHANCE muon system geometry. Figure 3.23 shows this map for configuration B. The density map of the PoCA scattering vertices for configuration A is shown in figure 3.24.

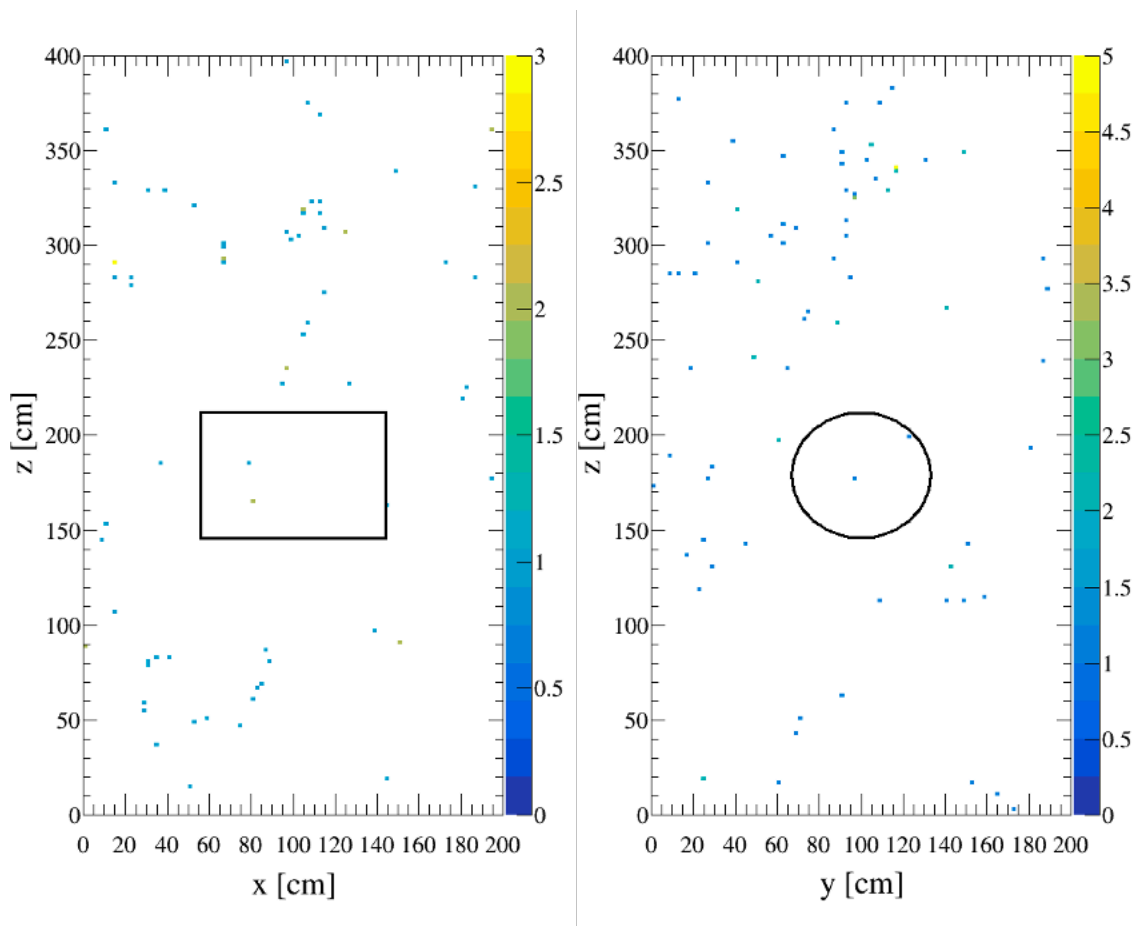


Figure 3.23: Distribution of scattering vertices reconstructed using the PoCA algorithm with CHANCE muon tomography system in the XZ (left) and the YZ (right) plane. Results for Configuration B of the CHANCE muon detector and voxel size of $2 \times 2 \text{ cm}^2$. The black rectangle and circle represent the expected location of the mock-up waste drum.

As explained in the D4.1 report and section 3.5, we were caught by surprise by a Freon ban that came into force at the early phase of CHANCE. This forced us to use CO₂ in the RPC system. CO₂ yields a much lower hit efficiency. In order to reconstruct tracks, hits in all traversed layers are required. Hence, the efficiency to detect tracks reduces by the product of the efficiency of all layers. This led to a very small track sample. Due to limited statistics, we were not able to perform more differential experimental studies of the performance of methods of material identification we had developed for the CHANCE muon scattering tomography system.

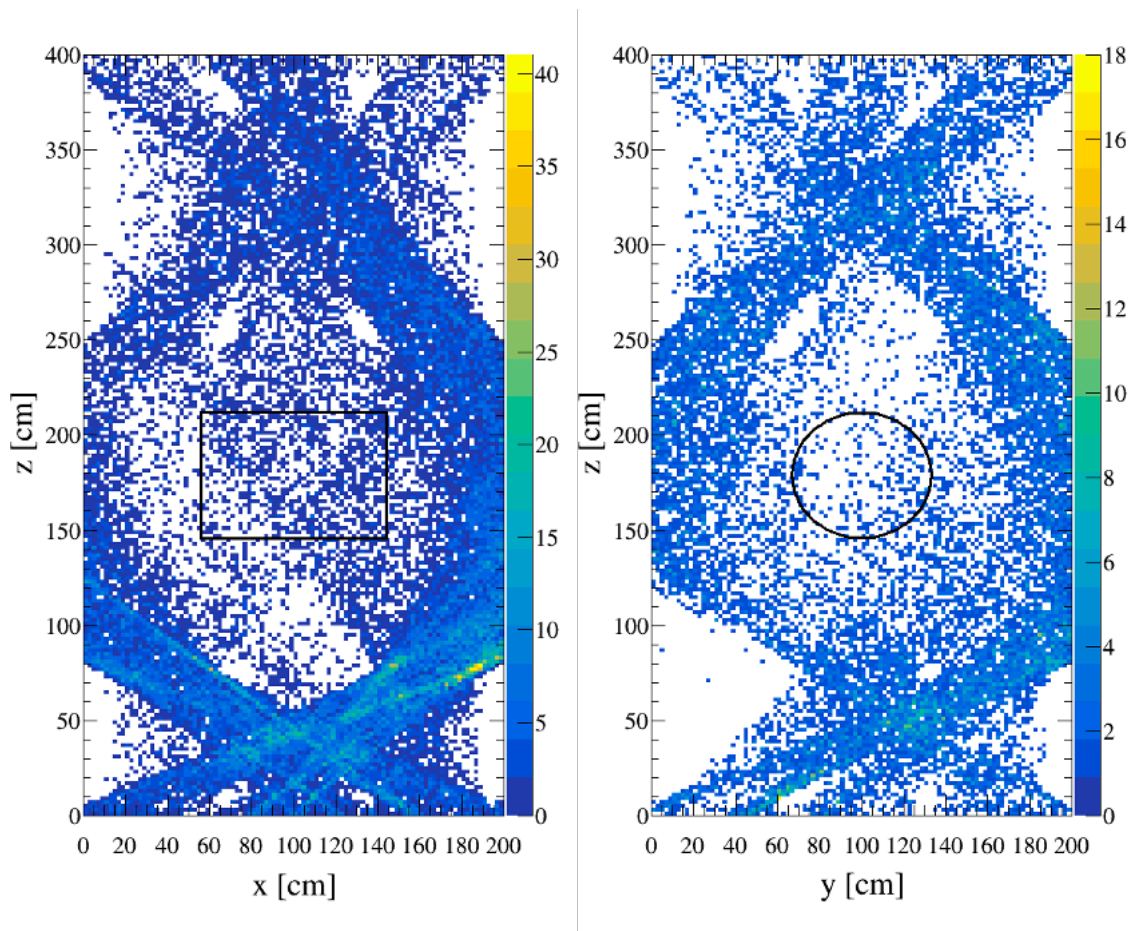


Figure 3.24: Distribution of scattering vertices reconstructed using the PoCA algorithm with CHANCE muon tomography system in the XZ (left) and the YZ (right) plane. Results for Configuration A of the CHANCE muon detector and voxel size of $2 \times 2 \text{ cm}^2$. The black rectangle and circle represent the expected location of the mock-up waste drum.

3.6 Summary experimental programme

In the Muon Tomography work package of the CHANCE project, we set out to build and operate a muon tomography system using RPCs and drift chambers. The system was intended to be mobile system to be operated in a non-laboratory environment. We have built and operated this system. It was operated in two different barns at Fenswood farm, a University of Bristol owned farm. The system was moved between the two barns, showing that it is mobile.

The project has not been without challenges. We have reported on them in this report and continuously during the project progress reports. An overview is given in section 3.5. Our main issue was the ban on the use of R-134a (Freon). This could not have been foreseen at the start at the project nor mitigate against. Our RPCs leak a small amount of this to the atmosphere, but a blanket ban on R-134a came into force in the UK, which came into effect after CHANCE started. This made it impossible to purchase R-134a without the appropriate permit, which we could not get. Installing an approved abatement system would have cost ~£200,000 plus installation cost for site engineering. This was not feasible within the restrictions of the CHANCE project. As a result, we had to decide to run with CO₂ which has a much worse performance until an environmentally friendly gas was found. Such a gas was discovered and published in November 2021 [30]. Our gas supplier still does not deliver it and we would still need to apply for a permit, which takes ~3 months.

Despite all these issues that have made the practical part of the project extremely challenging, we did manage to deliver a working system. Muon tracks have been found and reconstructed. The results of the data analysis are not as clear as we had hoped. We pushed the data taking as long as we could to improve our data sample and thus imaging capability. The key issue was the freon ban. This only became apparent after the start of the programme. An environmentally friendly alternative is now available, but came too late for CHANCE. We are convinced that with the new gas we would be able to achieve the required RPC performance to perform imaging with the required precision.

4. Monte Carlo simulation studies

In order to prepare for the expected experimental data and further the development of data analysis algorithms, many Monte Carlo studies were performed. They were also used to compare different aspects of detector performance, such as feature and size resolution and the dependence on exposure time and material type.

In general Monte Carlo simulations are a key tool in the development of muon tomography algorithms for many groups around the world. Access to large scale measurement systems and actual waste drums is rare. In addition, muon tomography is a slow imaging technique. As mentioned in section 2, the cosmic muon flux at sea level is about 10000 m⁻²min⁻¹. This means that the rate through a cm² top area voxel, is only 1 min⁻¹. For scanning of nuclear waste, this time scale is fine. It is no problem for most applications to measure a few weeks. However, for experimental studies it is not (always) feasible to

obtain the high statistics data sets for many, many configurations in a reasonable time. Our work has been cutting edge. It has led to 9 publications and 13 conference talks. Here several highlights are presented.

As usual in the field, GEANT4 [31] was used to simulate the passage of the muons through detectors and scanned objects. The muons were generated using the CRY library[32].

4.1 Performance studies algorithms

As mentioned in section 2.1, many algorithms exist. Of particular interest for the CHANCE project are the PoCA, the ASR and the BC algorithm. As these have been developed by different groups, no benchmarking was ever undertaken.

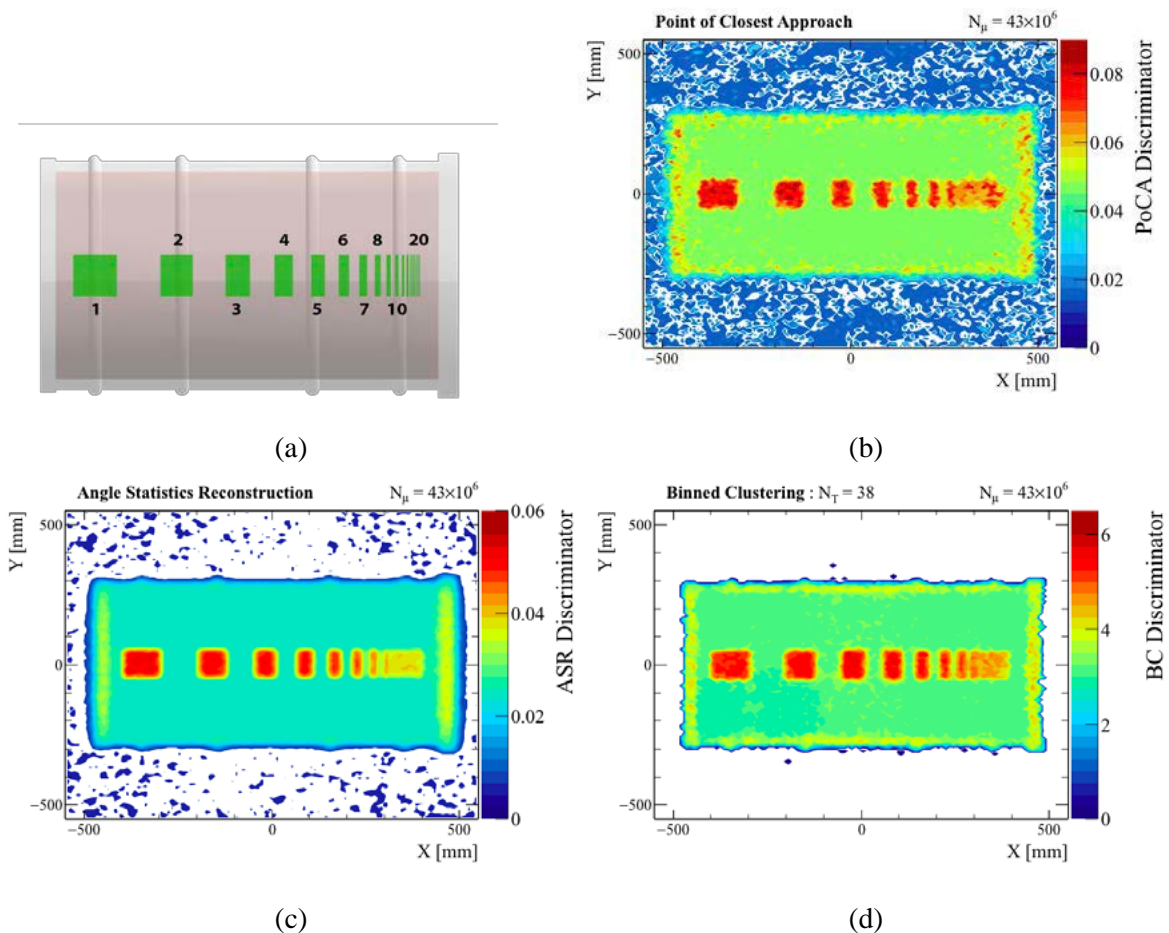


Figure 4.1: Uranium feature resolution test images after 25 days of simulated cosmic ray exposure. The true geometry is shown in (a). Reconstructed image using the PoCA (b), the ASR (c) and the BC (d) algorithm. The number of observable objects gives an indicator on the resolution of each imaging technique. It is only possible to observe 6 separated objects using the PoCA algorithm, whilst the ASR and BC algorithms can both make out an additional feature.

4.1.1 Resolution tests

A suitable Figure Of Merit (FOM) is needed for waste characterization that can be used to compare the performance of competing detector systems and algorithms for the detection and evaluation of radioactive material hidden inside large waste volume containers. Such a FOM would capture how the intrinsic detector resolution, and choice of tomography algorithm, can impact the detail in a reconstructed density map. To do this, an application of “optical” resolution tests to understand size and feature resolution in a muon tomography system was used. For details see [33]².

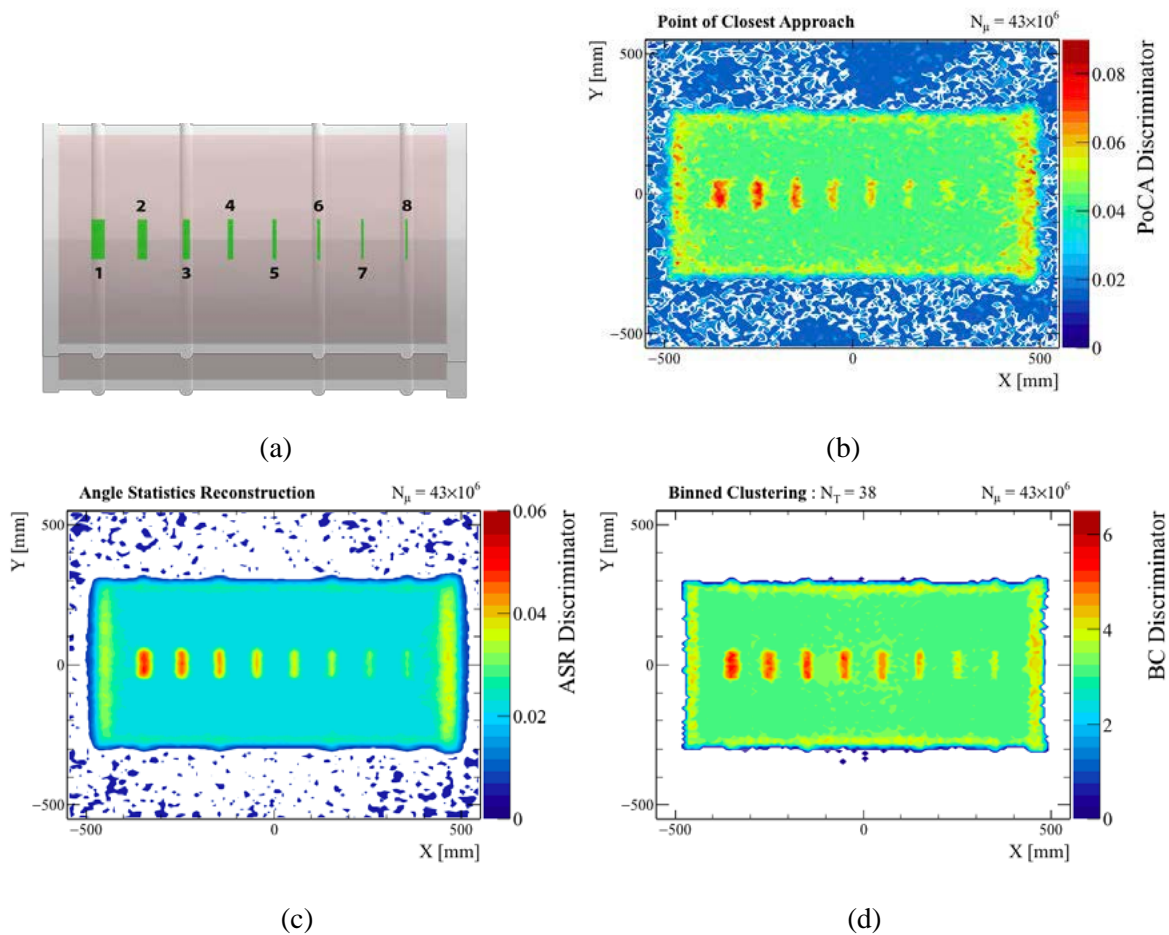


Figure 4.2: Uranium feature resolution test images after 25 days of simulated cosmic ray exposure. The true geometry is shown in (a). Reconstructed image using the PoCA (b), the ASR (c) and the BC (d) algorithm. The number of observable objects gives an indicator on the resolution of each imaging technique. It is only possible to observe 6 separated objects using the PoCA algorithm, whilst the ASR and BC algorithms can both make out an additional feature.

² [33] is a CHANCE output. The paper was presented at WM2019 and is included in Appendix A.2.

To compare the imaging performance of the algorithms. A feature resolution test is developed to understand an algorithms ability to distinguish high density objects in close proximity to one another. A size resolution test is developed to understand the smallest object that can be observed by a given tomography algorithm. An array of 20 cuboid uranium target objects was simulated, each with sides of 10 cm in the Y and Z dimension. Starting at a X dimension thickness of 10 cm, the thickness and spacings in the X dimension are reduced by a factor of 75% for each successive target object. The objects were placed inside a 88 cm high and 57 cm wide nuclear waste drum filled with concrete. Figure 4.1 shows the reconstructed images after 25 days of muon exposure. The analysis used 1 cm^3 voxels.

All algorithms find it difficult to easily separate features smaller than 1.6 cm. The PoCA algorithm with its higher inherent noise can also only observe 6 clear objects. If a muon undergoes a number of additional small scatters as it leaves the high density target material, the scattering vertex can be reconstructed just outside of the target. This mixing effect leads to the high density objects merging in the output density maps when they are placed in close proximity. It is also worth pointing out that as the size of the Uranium cuboids decreases, so does the average discriminator in the ASR map, showing a discriminator value comparable to steel for the smallest objects. The PoCA and BC algorithms however both show regions with high discriminators despite their ability to finely separate the presence of individual uranium sheets.

In the previous test the spacing between the objects was reduced. Due to the mixing effects in the reconstruction and analysis, the objects start to merge. To find the thinnest object an algorithm can detect, the same uranium objects were used but the spacing kept large. The results are shown in figure 4.2. The PoCA algorithm is only capable of clearly resolving 5 objects, corresponding to a smallest observable object of 0.95 cm, comparable to the voxel size. In contrast, the ASR and BC algorithms both show much cleaner, rectangular features for all 8 objects, resolving the presence of a target object down to 4mm.

The tests developed here were used to directly compare the imaging performance of different muon tomography techniques. It clearly showed that the ASR and BC have similar performance for these tests, while both are performing much better than PoCA.

4.1.2. Contrast to Noise ratio

An alternative way to compare algorithms is the contrast to noise ratio (CNR)³. The CNR method is applied to compare two regions in the reconstructed image of the investigated drum, such as a region containing high-Z material against another region containing a background signal. It evaluated the capability of an algorithm to differentiate between low-contrast, medium-contrast, and high contrast regions inside the investigated volume. CNR is defined as:

$$CNR = \frac{|\mu_A - \mu_B|}{\sqrt{\sigma_A^2 + \sigma_B^2}} \quad (4.1)$$

A high value CNR indicates the algorithm is able to distinguish between the two regions under comparison. A study was done with different materials in the waste drum. The true geometry and materials list and the reconstructed images are shown in figure 4.3. From these images the CNR was calculated for each algorithm for different materials and sizes ranging between 7 and 13 cm, see figure 4.4. The BC and ASR algorithms demonstrate very similar performance when comparing the regions that contained a high-Z material (uranium) cube against the background regions. In the case of a 10 cm cube the BC method produces a slightly lower CNR value of 7.1 ± 0.34 compared to the CNR value of 7.9 ± 0.25 produced by the ASR algorithm. The PoCA algorithm shows consistently worse performance. The ASR algorithm is the most capable of differentiating between medium-Z and high-Z materials with a CNR value of 5.35 ± 0.1 , which is approximately 34% better than the CNR value produced for the comparable regions by the BC method.

³ This work is a CHANCE output. Part was presented at WM2021 [34] and can be found in Appendix A.3. A second paper has been submitted to the Journal for Instrumentation.

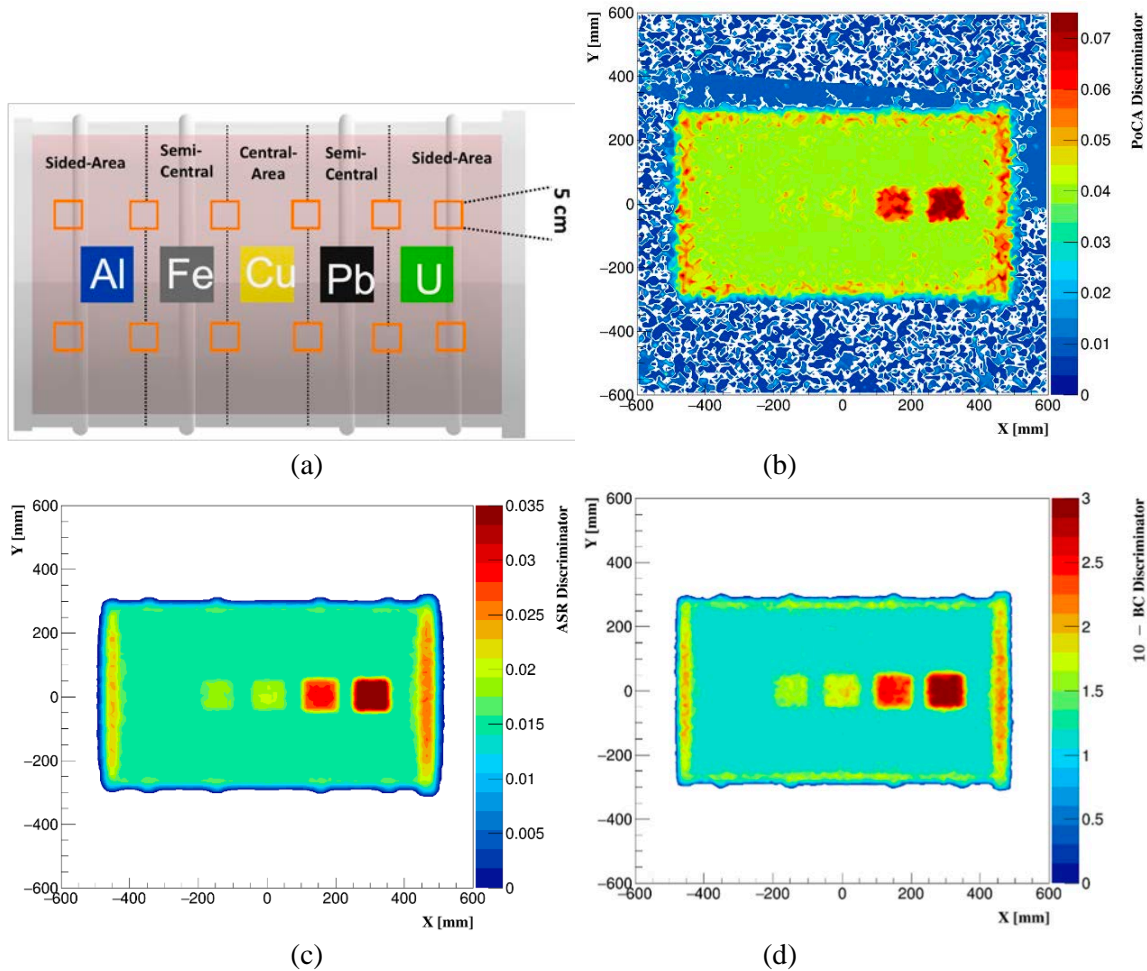


Figure 4.3: Test images after 30 days of simulated cosmic ray exposure. The true geometry and material list is shown in (a). Reconstructed image using the PoCA (b), the ASR (c) and the BC (d) algorithm.

A study of the CNR value as a function of equivalent exposure time was undertaken as well. The results are shown in figure 4.5. It showed that producing good tomographic images of the target materials can be achieved with fewer cosmic muons by using the ASR algorithm. By using the ASR method, the MST system can separate uranium and lead from background regions in only six hours of muon exposure time with CNR values of 3.1 ± 0.2 and 2.5 ± 0.2 respectively.

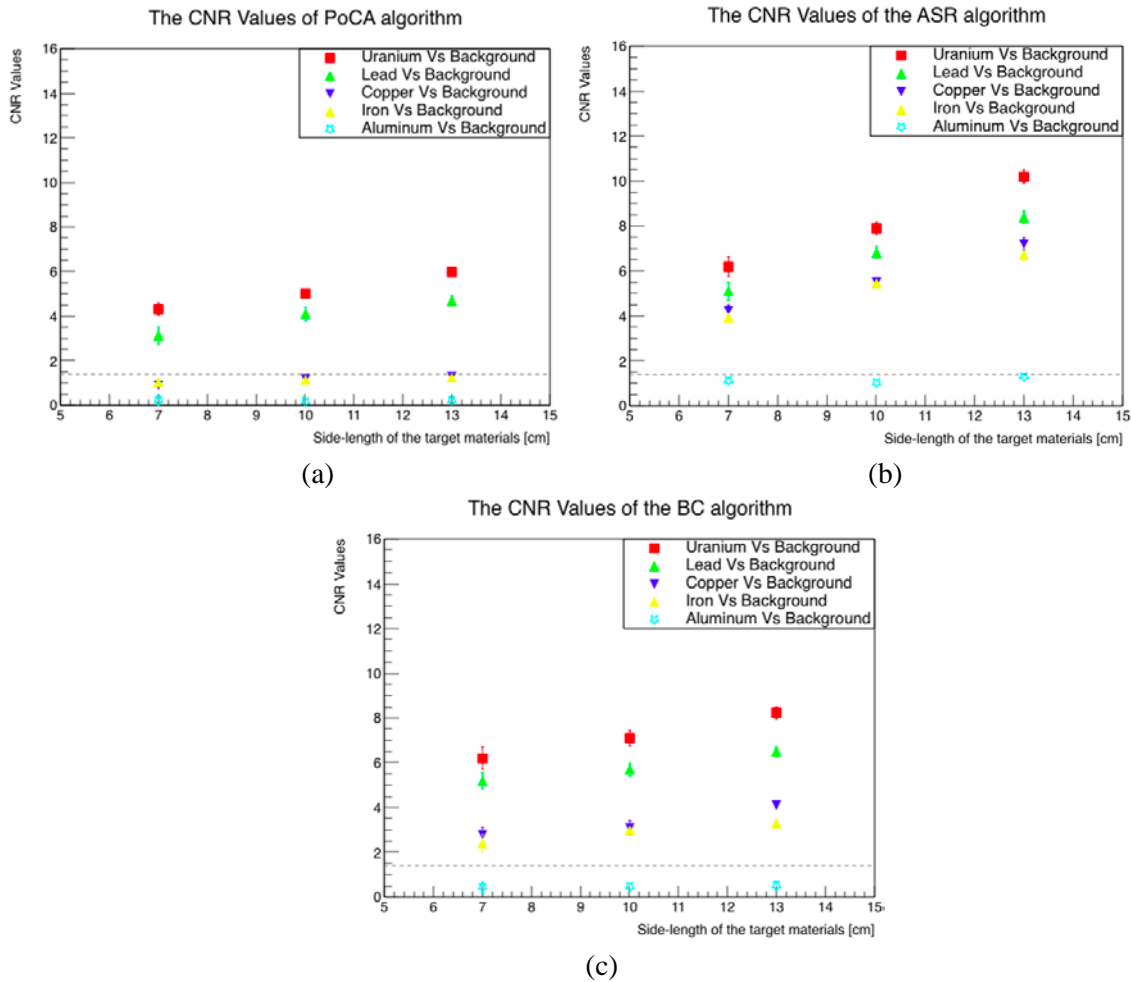


Figure 4.4: Comparison of the CNR values of the (a) PoCA, (b) ASR and (c) BC algorithms when differentiating between different target materials and background for target materials with side lengths of 7, 10, and 13 cm. Results are for 30 days of muon exposure time. The vertical dashed line represents the minimum CNR value used to distinguish the target material inside the drum.

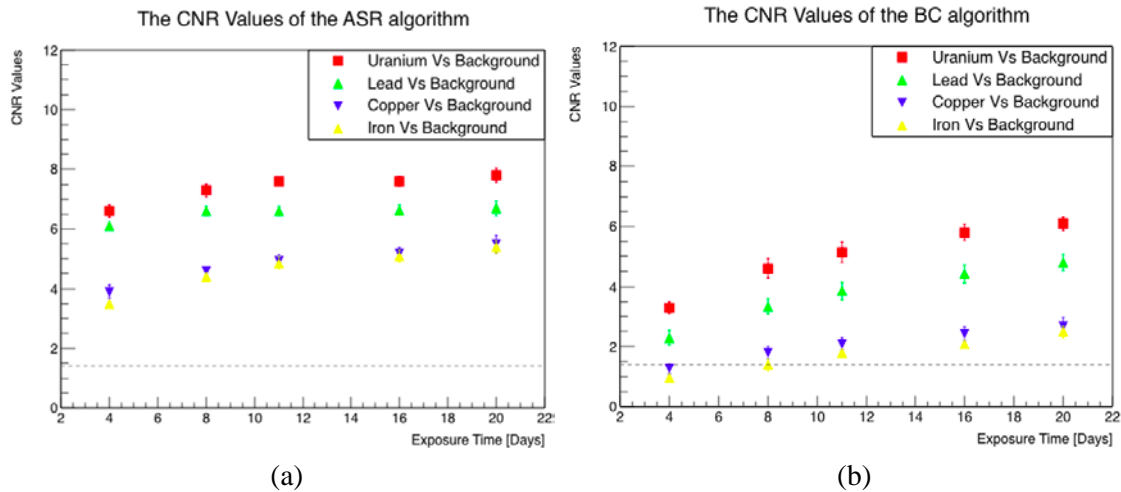


Figure 4.5: Comparison of the CNR values produced by the (a) ASR and (b) BC algorithms for different materials of 10 cm side-length as a function of the muon exposure time. The vertical dashed line represents the minimum CNR value used to distinguish the target material inside the drum.

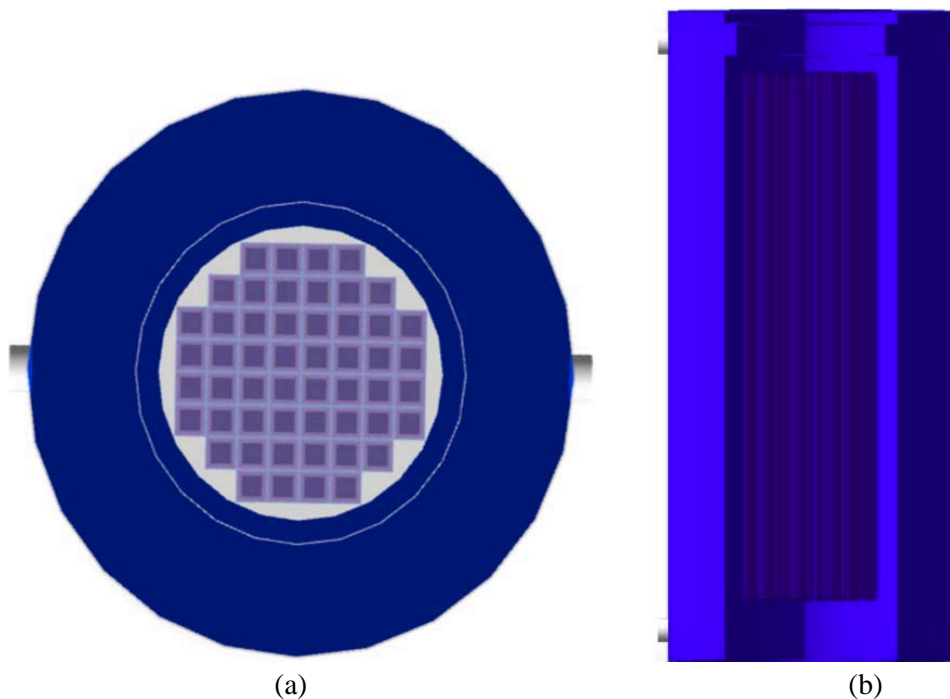


Figure 4.6: (a) top and (b) side views of the simulated V/52 CASTOR cask accommodating the 52 waste baskets. The lid and the base removed for visualisation purposes.

Applying CNR to a large V/52 CASTOR drum

The CASTOR V/52 cask is designed for the transport and storage of spent fuel assemblies from boiling water reactors. A sketch is shown in figure 4.6. The cylinder-shaped V/52 cask is made of ductile-iron (~94% iron, 0.033% carbon, 0.004% copper) with a height of 5.54 m and a total diameter of 2.44 m. A cavity of 1.42 m diameter and 4.55 m height inside the centre of the cask is designed to accommodate the baskets for the fuel assemblies, which are surrounded by nearly 1 m of ductile-iron shielding. The cavity is designed to store 52 baskets that accommodate UO₂ (~88.2% uranium and 11.8 oxygen) fuel assemblies that originate from Boiling Water Reactors (BWR). The simulated box-shaped baskets have a length of 4.48 m and are arranged across a grid of eight columns and eight rows. A pair of trunnions is also simulated at the top and the end bottom of the CASTOR. These trunnions are bolted and only be used for the attachment of handling equipment.

The CNR test was used to detect anomalies in the contents of the CASTOR. This is of particular interest to state nuclear waste repository operators who are required to consider nefarious material diversion scenarios. All CASTOR baskets were filled with UO₂, except four, see figure 4.7. An empty basket, a half-loaded basket, a basket filled with copper and a basket filled with lead were introduced. Comparing the empty basket with the eight surrounding fully loaded baskets produces CNR value of 5.0±0.3 when considering the 25% quantile of each voxel distribution. The CNR values for half-unloaded baskets are just above the minimum distinguishable CNR level of 1.9±0.2. The regions of the basket filled with lead pellets and the surrounding baskets are not distinguishable due to the similarity of lead and UO₂ densities.

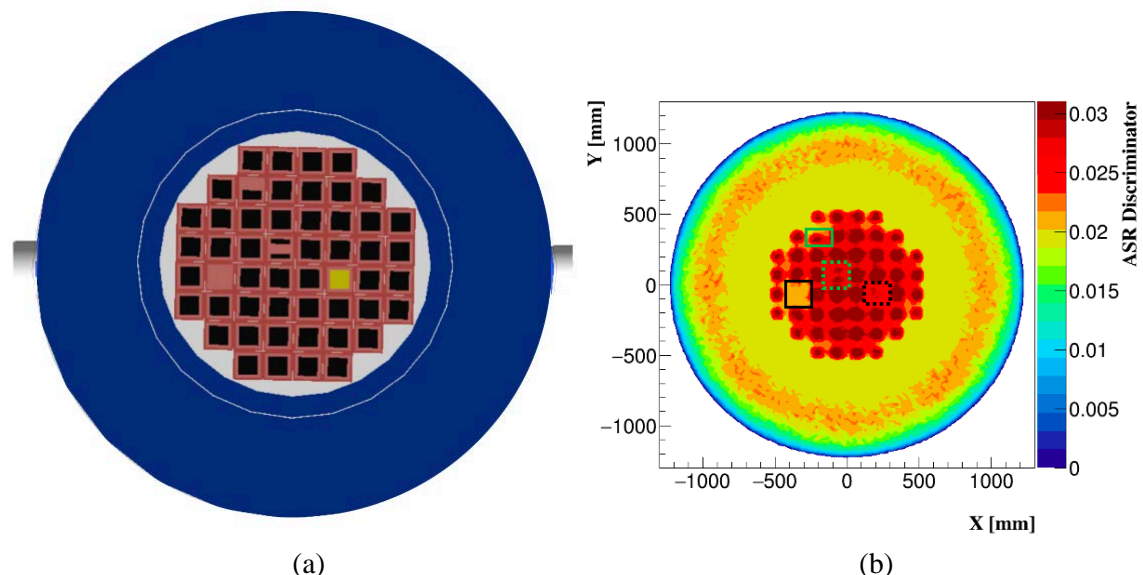


Figure 4.7: (a) top-view of the V/52 CASTOR showing four baskets contain irregularity in their contents. Image produced by the ASR algorithm when considering 25% of the ASR discriminator in each voxel (b). The solid and dashed green boxes indicate the half-loaded baskets, while the solid and dashed black boxes indicate the baskets that contain no pellets and copper pellets, respectively. The exposure time was 30 days equivalent.

4.1.3 A Robust Method to Find Gas Bubbles

In waste drums the waste is enclosed in concrete and/or bitumen. The radioactive decays can lead to the build up of gas bubbles, in particular H₂. The presence of H₂ gas bubbles inside nuclear waste containers can present a serious safety issue during interim storage. The issue is the most prominent for bitumen matrices, and we studied such cases. We have previously shown that it was possible to reconstruct bubbles of a total gas volume of 2 L or more with a resolution of 15±0.77% in 16 days of data taking using muon tomography [35]. For this study we used standard concrete with a density of 2.3 g/cm³. Here we compared the performance with different types of bitumen: Eurobitum and STE3. Eurobitum consists of ~60 wt% of pure bitumen Mexphalt R85/40 and ~40 wt% of radioactive salts and metal (hydro)oxides, of which NaNO₃ (20 - 30 wt%) and CaSO₄ (4 - 6 wt%) are the most important ones. STE3 consists of a pure bitumen Viatotal 70/100 mixed with NaNO₃ (28 wt%), Na₂SO₄ (5 wt%), CoS (10 wt%), BaSO₄ (46 wt%) and PPFenNi (9 wt%).

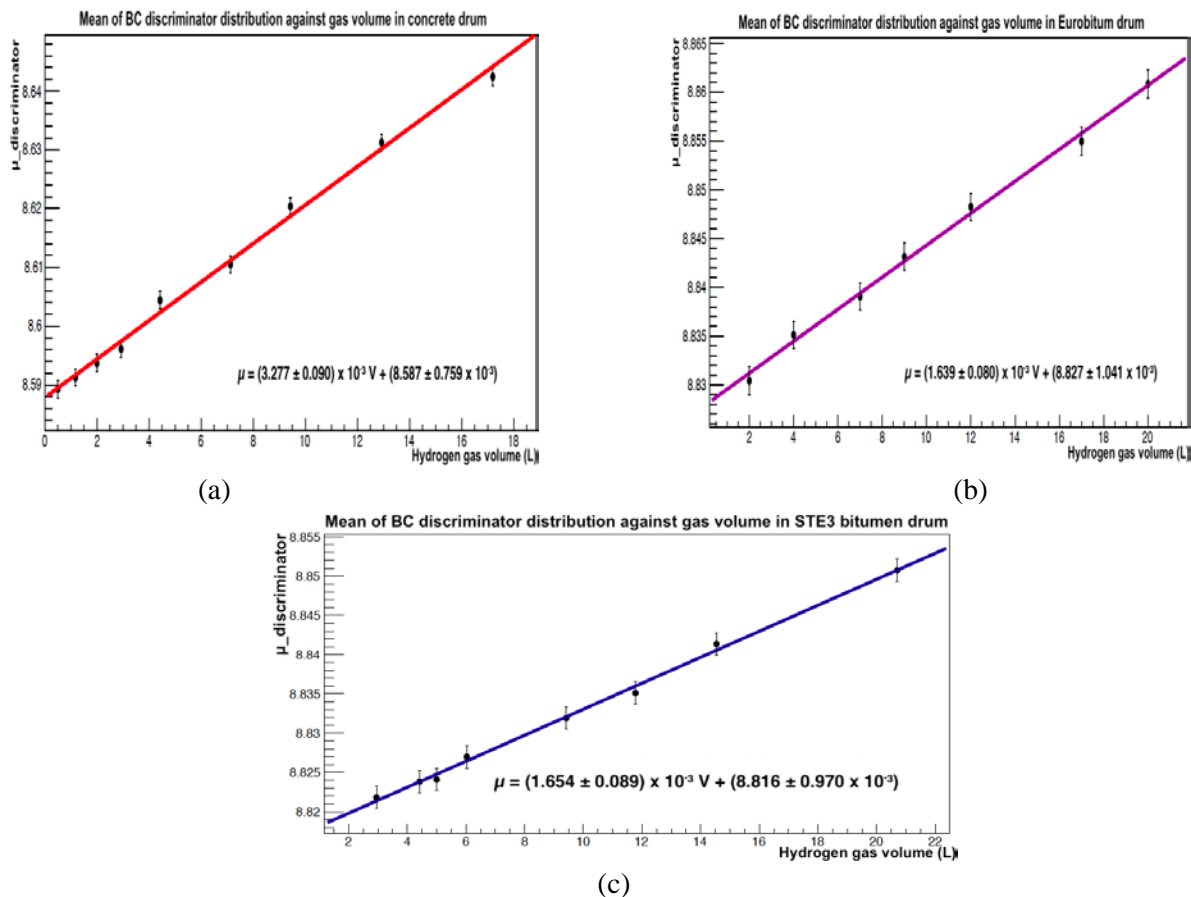


Figure 4.8: The H₂ volume values against the corresponding discriminator value μ with linear regression fits for a Concrete filled drum (a) and a Eurobitum filled drum (b) and a STE3 bitumen filled drum (c).

The method exploits the BC algorithm. Varying amounts of hydrogen are included into the matrix and the discriminator for the entire drum is calculated, see section 2.1.3. Figure 4.8 shows the discriminator as a function of the total H₂ volume. The graphs show that the discriminator depends linearly on the amount of hydrogen in the drum. The slope is proportional to the density of the bitumen.

Using the slopes the volume of H₂ in a drum can be determined. Figure 4.9 shows the relative uncertainty in the total H₂ volume for the three types of concrete. For bubbles larger than 2L the relative uncertainty on the H₂ volume was below 10%. This increases rapidly for smaller bubbles. The accuracy of volume reconstruction for the smallest bubbles considered in our studies is better for higher density matrices.

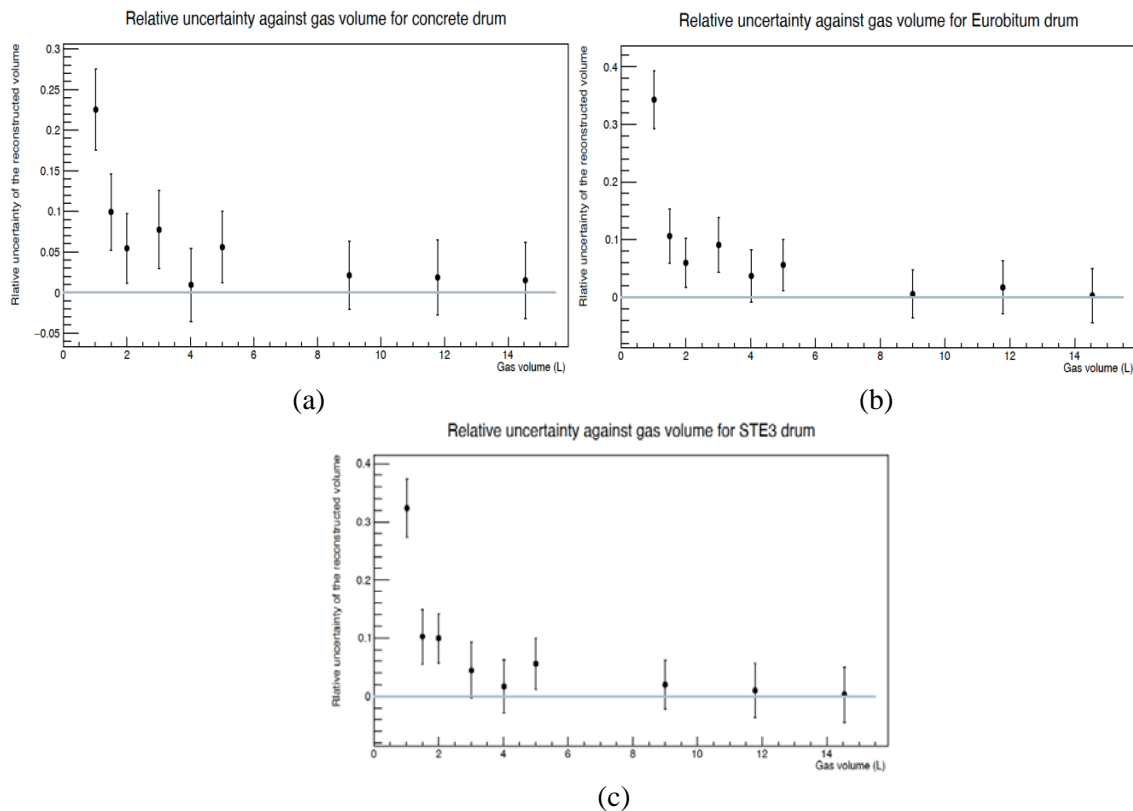


Figure 4.9: The relative uncertainty on the reconstructed H₂ bubble volumes against the true H₂ gas volume for a concrete filled drum (a) and Eurobitum filled drum (b) and a STE3 bitumen filled drum(c).

Improving bubble detection limit

To further reduce the minimum detection level for bubbles, a new algorithm is being developed⁴. The drum is divided into 3×3×3 cm³ voxels. For each voxel the BC discriminator is determined. Figure 4.10(a) shows the distribution of the discriminator for voxels filled with hydrogen and filled with

⁴ This work is a CHANCE output. A paper is in preparation.

concrete. Next a threshold value is determined to decide whether a voxel contains hydrogen or concrete. Figure 4.10(b) shows the efficiency and purity of the decision as a function of the threshold value. The efficiency of hydrogen detection is better than 90% for each of these regions, with false-positive rate lower than 10%.

Figure 4.11(a) shows a 3D image of two reconstructed hydrogen bubbles, which were simulated within the bituminized waste drum. Their location matches well the simulated objects. To evaluate the precision of the method and its detection limits, we simulated different hydrogen volumes within waste container filled with bitumen. Figure 4.11(b) shows the obtained reconstructed volume vs the simulated (true) one. The data points show the results calculations, the line represent a linear function fit together with its uncertainties (one- and two-standard-deviation contours). The relative uncertainty on hydrogen volume measurement using this approach is below 10% for bubbles larger than 0.85 L. The detection limit of this method is 0.55 litre at a 95% confidence level.

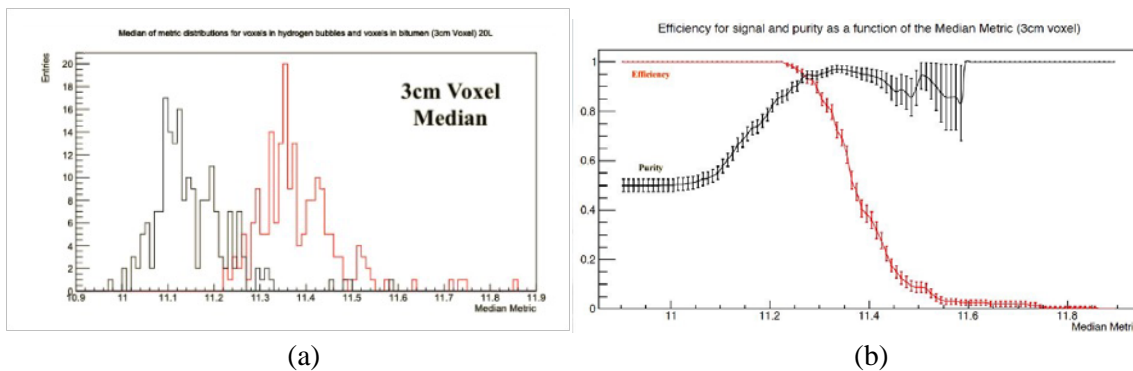


Figure 4.10: Distribution of Median Metric for matrix material (bitumen, in black) and hydrogen (in red) for 3 cm voxels (a) and the efficiency and purity of hydrogen detection in the bituminized waste container as a function of decision threshold of Median Metric (b).

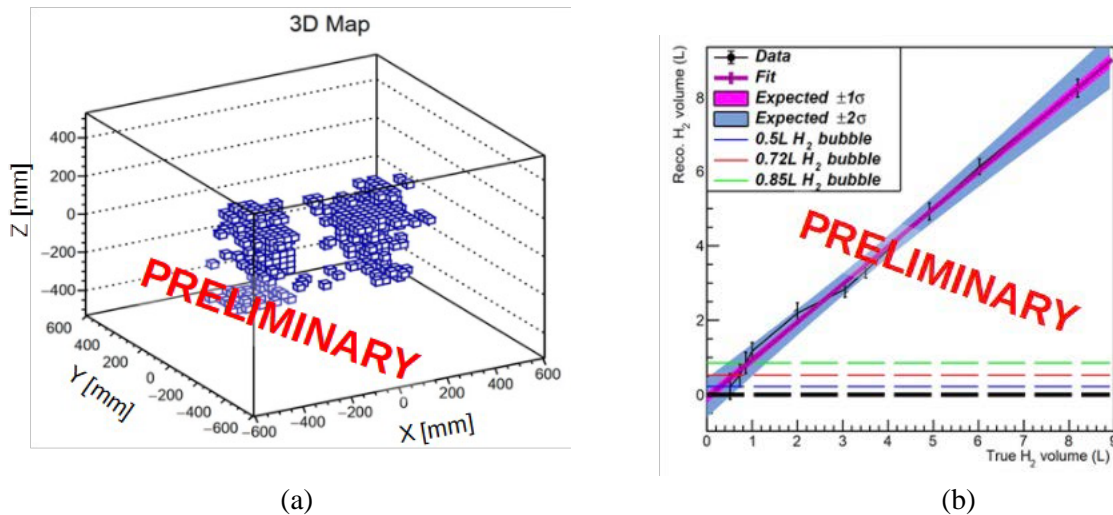


Figure 4.11: 3D image of two 4-L hydrogen bubbles, extracted for a case where a bitumen-filled drum with two bubbles was simulated (a) and the reconstructed hydrogen volume vs simulated amount of gas for a bituminized waste container (b).

4.2 Material identification

Previously, we have shown that it is possible to identify materials that are encased in the concrete [3]. To improve the performance, a new approach utilizing machine learning was developed⁵. First, the BC algorithm is run on the data. This produces for each voxel, a set of $m_{i,j}$ metric values. A normalised histogram of the $\log m_{i,j}$ values are passed to Multi Variate Analysis (MVA) classifiers. Those were trained to recognize four different materials: concrete, iron, lead and uranium. The training sets were simulated drums containing 20 cm cubes of each material, centred in the drum. A 10-day exposure of each was simulated, then the BC algorithm was applied to the results which provides a best material match for each voxel. Next the voxels are clustered and filtered. Figure 4.12 shows the results for a 10-day simulation of a drum containing 15 cm cubes of iron, lead and uranium.

⁵ This work is a CHANCE output. The initial paper was presented at WM2021 [37] and improved results were published in [4]. Both papers can be found in Appendix A.5.

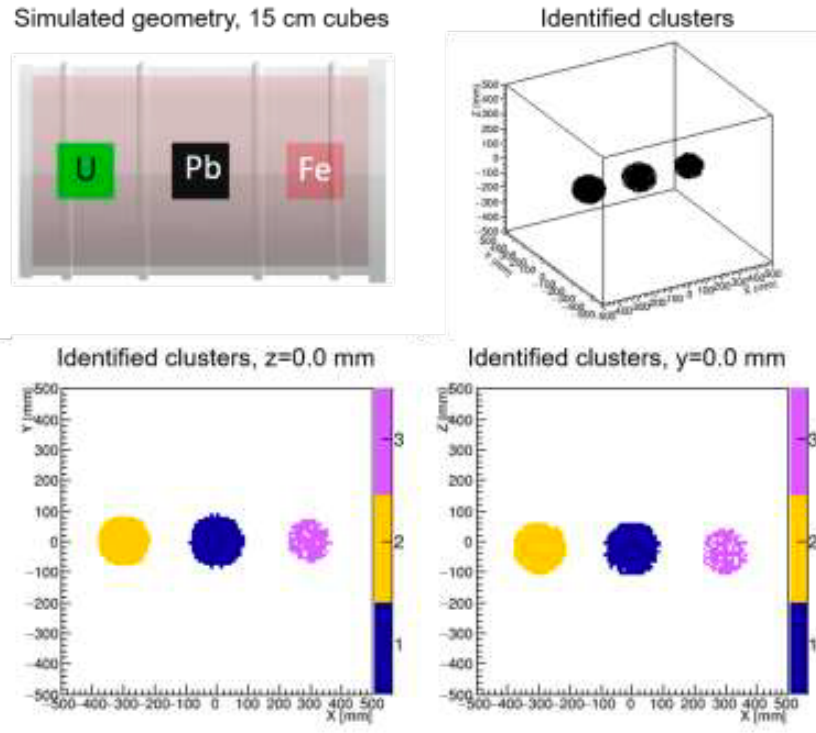


Figure 4.12: Result of applying filtering and clustering algorithms to a simulated drum containing three cubes. Clockwise from top left: the simulated drum geometry, a 3D view of the filtered image, xz slice of the filtered image showing clustering solution, xy slice of the filtered image.

The voxels in the BC algorithm output image corresponding to the stored cubes have been successfully isolated and clustered. Two further MVA classifiers are now applied to these identified objects to obtain material information. These are a non-binary classifier with iron as the ‘signal’ case and lead and uranium as ‘background’ cases, and a binary lead-uranium classifier (with uranium as ‘signal’). The results are shown in figure 4.13. For objects of similar volume to the 20 cm cubes used for training the classifiers, the largest value corresponds to the correct material, and objects of different materials are clearly distinguished by the three material values. Test on different geometries were run as well and the results are not affected by the geometry of the object.

Smaller volumes were investigated. With smaller volumes, the performance is still very good. With a sample set of randomly generated drum geometries, we were able to correctly identify uranium objects on a scale of ~ 10 cm with an efficiency of $0.90^{0.07}_{-0.12}$ and a corresponding false positive rate of $0.12^{0.12}_{-0.07}$, indicating that this approach is effective at identifying uranium objects stored inside waste drums. The identified vulnerabilities include objects of materials with very different Z values, such as iron and uranium, that are close together; uranium objects can be misidentified in such cases.

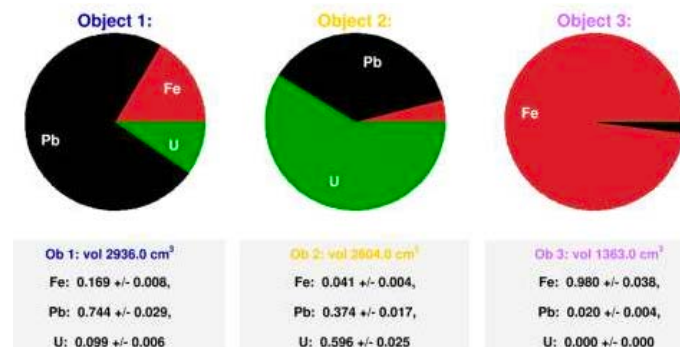


Figure 4.13: Calculated material values for successfully identified clusters corresponding to three stored 15 cm cubes of uranium, lead and iron. In each case, the largest value corresponds to the true material.

4.3 Summary

In order to prepare for the expected experimental data and further the development of data analysis algorithms, many Monte Carlo studies were performed using a simulation tuned to the expected performance of our system. Using the simulations, we have furthered the field significantly. We have developed new algorithms which have improved material identification, lowered the detection threshold for the detection of hydrogen bubbles in waste drums with a bitumen matrix and used our techniques not only on standard waste drums but also to detect anomalies in the contents of CASTOR V/52 drums. This work was scientifically a great success. It has led to 9 publications, 1 more was submitted recently and 1 more is in preparation, and 13 talks and three PhD theses are in preparation.

5. Hot test plans

The initial programme foresaw a hot test at the end of the project. We planned to move the MST system to one or more nuclear waste storage facilities outside of the UK to characterize some real, large waste containers and spent fuel casks. At the start of the project, we did not have a WMO partner lined up. We approached several potential partners for this. The most advanced discussions were held with BGZ and Zwiilag. However, due to restrictions on international travel from February 2020 onward and strict rules on working arrangements which minimised the number of people on site, it was not possible to complete the intended overseas work for the so-called hot test programme of work as originally was planned after characterisation of the dummy drums.

5.1 BGZ

In June 2019, the team visited the Bundesgesellschaft Gesellschaft für Zwischenlagerung mbH in Essen (Germany). BGZ were interested in using muon tomography to investigate the structural integrity of fuel rods stored in CASTOR drums. We proposed a prior simulation study before deployment to study the expected precision and sensitivity of our measurements. We requested more details to be able to undertake the study. BGZ decided that they did not want to go ahead at that particular moment.

5.2 Zwilag

In September 2019, the team visited Zwilag (Switzerland) to discuss a potential deployment of the muon system to image a special set of waste drums. Zwilag has a set of large drums that were filled when cleaning up the Lucens reactor accident. The current contents and state of the contents is not well known. Muon tomography is an excellent technology to image the contents of the drums. A potential deployment was discussed and a first Monte Carlo simulation study was undertaken. The slides of the results can be found in Appendix A.6.

The results of the simulation study were very positively received by Zwilag. We had a follow up meeting in January 2020. Our presentations on the first simulation study were very well received. A key issue was that more simulation studies were needed to have a more detailed view of the potential results of a deployment. We requested resources to do this, but ran into an issue that there were potential funds for a deployment available but not for a feasibility study. During the discussions Covid hit and we could not proceed with a potential deployment.

6. Awareness and future of muon tomography

The WP4 consortium has worked hard to engage with external partners, specifically end users such as national European bodies which are responsible for the disposal of nuclear waste. The aim of these interactions has been to heighten awareness of the muon tomography technique and its suitability to a wide range of applications in the nuclear waste disposal community, including material characterisation as well as nuclear waste safety and safeguards.

6.1 IAEA workshop on muon tomography

In September 2019 CHANCE WP4 was represented by Anna Kopp and Lee Thompson at the IAEA at small focussed by-invitation only workshop entitled “IAEA Technical Meeting on Non-destructive Testing Using Muon Radiography”. The conclusions of this workshop have been written up as a so-called IAEA TECDOC which will soon be published on the IAEA website and will be used to educate member state engagement with muon tomography in the future.

6.2 BGE & FZJ

Following on from the IAEA meeting in Vienna in 2019, there was significant interest in the muon tomography technique from BGE (the German state-funded organisation for nuclear waste disposal) and FZJ (the German nuclear physics laboratory) which has resulted in regular fortnightly/monthly meetings throughout the COVID pandemic. This collaboration resulted first in Thompson being invited to deliver an in-person presentation on muon tomography at the “Interdisciplinary research symposium on the safety of nuclear disposal practices, organised by BASE” in Berlin in November 2021.

6.3 Nagra & NWS

Following the talk from BASE there has been significant interest in the muon tomography technique from the Swiss (NAGRA) and UK (RWM, now NWS) state companies. Throughout late 2021 and early 2022 Thompson has worked with these companies to draw up a proposal for an ambitious programme of muon tomography proof of principle experiments at the Grimsel Test Site (GTS) in Switzerland. The proposal shown in Appendix A.7 was recently formally submitted to the GTS for consideration for financial support in the summer of 2022.

6.4 Euratom

Furthermore, Thompson has been invited by Euratom inspectors to present the muon tomography technique at the ESARDA conference in May 2022.

6.5 Geoptic

In addition to the above, a University of Sheffield spin-out company, specialising in muon tomography, has been formed during the course of the CHANCE project, the company, Geoptic (www.geoptic.co.uk) specialises in the use of muon radiography in searching for hidden voids in railway infrastructure.

6.6 IAEA expert mission

As a result of the CHANCE work, Velthuis was invited on an IAEA expert mission (Slater EVT6310 RER9146 Expert Mission on Methods for Localization of Radioactive Sources in a Large Concrete Structure). The mission took place in January 2020. Velthuis advised on the potential role muon tomography could play in the decommission of a particular nuclear site. This work is covered by an NDA.

6.7 IRSN

Also as a result of CHANCE we have been discussing a potential muon tomography project for IRSN Institut de Radioprotection et de Surete Nucleaire (France) in the fall of 2021. They were very interested in monitoring the escape of hydrogen bubbles from waste drums with a bitumen matrix.

This was one of the things we studied and published within CHANCE. The IRSN group we were in touch with was mostly interested in measuring the speed at which the hydrogen moves in case of fire. We performed some feasibility studies for the experimental programme they wanted to undertake. IRSN planned to have very small bitumen filled containers (paint tin size) and heat them up. After our feasibility study, we found that we could measure the hydrogen distribution inside the waste drums, but not within the time frame required for degassing in the case of fire in the small size drums they are planning to use. They are now considering alternative technologies or will decide to redesign their experiments and use large waste drums.

6.8 Cavendish Nuclear Ltd

Inspired by CHANCE, the Bristol team was approached by Cavendish Nuclear Ltd, a daughter of Babcock, about the potential of muon tomography to image rebars inside concrete walls and floors, mainly with an eye on decommissioning of civil nuclear installations. This project also started with a Monte Carlo simulation feasibility study. The results have been published in several publications, see e.g. [10, 38]. Using muon tomography, it is possible to detect the location of the thinnest commercially in use rebars in 50cm thick walls. This project is continuing and a deployment is on the horizon.

6.9 Summary

As a result of the CHANCE project, a lot of interest in muon tomography was generated. Many new projects were started as a result of the CHANCE work. The future of muon tomography is looking very positive.

7. Conclusion

Muon Scattering Tomography (MST) has been shown to be a powerful technique for the non-invasive imaging of objects from a safe distance without the introduction of radiation. It exploits the natural background radiation. By measuring the incoming and outgoing radiation, the contents of the object under inspection can be determined. The technique can be used to address many challenges including imaging the contents of nuclear waste drums.

Within CHANCE we built and operated a mobile muon tomography system based on drift chambers and RPCs. To prepare for data and to further develop imaging algorithms, a large Monte Carlo study effort was undertaken. We delivered a working system. Muon tracks have been found and reconstructed. However, the experimental part of the project was extremely challenging. Brexit and Covid made any maintenance and any purchase extremely complicated. The largest problem we encountered was a ban on R-134a. R-134a is the gas of choice for operation of our type of RPCs. Just before the project started, it became impossible to purchase this gas and illegal to use it. We decided to run with CO₂ instead until an alternative for R-134a became available. CO₂ provides a signal 5–10 times lower than R-134a. This led to a low hit efficiency. This was a major issue because to reconstruct the path of a scattered muon, we needed to record a hit of that muon in each of the layers. This led to a very low track efficiency and thus to a very small track sample, too small to perform detailed imaging. An alternative for R-134a was published in November 2021, which was too late in the project to switch. Our gas supplier still does not deliver it and we would still need to apply for a permit, which takes ~3 months. Nevertheless, despite all these issues that have made the practical part of the project extremely challenging, we did manage to deliver a working system.

To prepare for the expected experimental data and further the development of data analysis algorithms, many Monte Carlo studies were performed using a simulation tuned to the expected performance of our system. Using the simulations, we have furthered the field significantly. We have developed new algorithms which have improved material identification, lowered the detection threshold for the detection of hydrogen bubbles in waste drums with a bitumen matrix and used our techniques not only on standard waste drums but also to detect anomalies in the contents of CASTOR V/52 drums. This work was scientifically a great success. It has led to 9 publications, 1 more was submitted recently and 1 more is in preparation, and 13 talks and three PhD theses are in preparation.

As a result of the CHANCE project, a lot of interest in muon tomography was generated. Many new projects were started as a result of the CHANCE work. The future of muon tomography is looking bright.

8. Bibliography

- [1] M. Dobrowolska et al. “A novel technique for finding gas bubbles in the nuclear waste containers using Muon Scattering Tomography”. In: *Journal of Instrumentation* 13.05 (May 2018), P05015–P05015. doi: 10.1088/1748-0221/13/05/p05015.
- [2] C. Thomay et al. “Passive 3D imaging of nuclear waste containers with Muon Scattering Tomography”. In: *Journal of Instrumentation* 11.03 (Mar. 2016), P03008–P03008. doi: 10.1088/1748-0221/11/03/p03008.
- [3] L. Frazão et al. “Discrimination of high-Z materials in concrete-filled containers using muon scattering tomography”. In: *Journal of Instrumentation* 11.07 (July 2016), P07020–P07020. doi: 10.1088/1748-0221/11/07/p07020.
- [4] M.J. Weekes et al. “Material identification in nuclear waste drums using muon scattering tomography and multivariate analysis”. In: *Journal of Instrumentation* 16.05 (May 2021), P05007. doi: 10.1088/1748-0221/16/05/p05007.
- [5] C. Thomay et al. “A binned clustering algorithm to detect high-Z material using cosmic muons”. In: *JINST* 8 (2013), P10013. doi: 10.1088/1748-0221/8/10/P10013.
- [6] L. J. Schultz et al. “Statistical Reconstruction for Cosmic Ray Muon Tomography”. In: *IEEE Transactions on Image Processing* 16.8 (Aug. 2007), pp. 1985–1993. doi: 10.1109/TIP.2007.901239.
- [7] P. Checchia et al. “Muon tomography demonstrator: past and recent results with an eye to near-future activities”. In: *Phil. Trans. R. Soc. A* 377 (2019), p. 20180065.
- [8] E. Niederleithinger et al. “Muon tomography of a reinforced concrete block first experimental proof of concept, *Journal of Nondestructive Evaluation*”. In: 40 (2021), p. 65.
- [9] J.M. Durham et al. “Tests of cosmic ray radiography for power industry applications”. In: *AIP Advances* 5:067111 (2015).
- [10] M.J. Dobrowolska et al. “Development of muon scattering tomography for a detection of reinforcement in concrete”. In: *Engineering Research Express* 3, 035037 (2021).

- [11] J. Beringer et al. “Review of Particle Physics”. In: Phys. Rev. D 86 (1 July 2012), p. 010001. doi: 10.1103/PhysRevD.86.010001. url: <https://link.aps.org/doi/10.1103/PhysRevD.86.010001>.
- [12] D. Reyna. A Simple Parameterization of the Cosmic-Ray Muon Momentum Spectra at the Surface as a Function of Zenith Angle. 2006. doi: 10.48550/ARXIV. HEP-PH/0604145.
- [13] Simon Eidelman et al. “Review of particle physics”. In: Physics Letters B 592.1 (2004).
- [14] C.L. Morris et al. “Tomographic Imaging with Cosmic Ray Muons”. In: Science and Global Security 16 (2008), pp. 37–53.
- [15] A. Kopp et al. “Non-destructive assay of nuclear waste containers using muon scattering tomography in the Horizon2020 CHANCE project”. In: EPJ Web Conf. ANIMMA 2019 – Advancements in Nuclear Instrumentation Measurement Methods and their Applications 06008 (2020).
- [16] A. Simpson et al. “Muon tomography for the analysis of in-container vitrified products”. In: Appl. Rad. Isot. 157, 109033 (2020).
- [17] M. Stapleton et al. “Angle Statistics Reconstruction: a robust reconstruction algorithm for Muon Scattering Tomography”. In: JINST 9 (2104), P11019.
- [18] P Baesso et al. “Toward a RPC-based muon tomography system for cargo containers.” In: Journal of Instrumentation 9.10 (2014), p. C10041.
- [19] P Baesso et al. “A high resolution resistive plate chamber tracking system developed for cosmic ray muon tomography”. In: Journal of Instrumentation 8.08 (2013), P08006.
- [20] P. Baesso et al. “Degradation in the efficiency of glass Resistive Plate Chambers operated without external gas supply”. In: Journal of Instrumentation 10 (June 2015), P06001–P06001. doi: 10.1088/1748-0221/10/06/P06001.
- [21] D. Cussans et al. “A readout system for a cosmic ray telescope using Resistive Plate Chambers”. In: JINST 8 C03003 (2013).
- [22] S. Blin et al. “MAROC, a generic photomultiplier readout chip”. In: IEEE Nucl. Sci. Symp. Conf. Rec. 1690 (2010).
- [23] R. Frazier et al. “Software and firmware for controlling CMS trigger and readout hardware via gigabit ethernet”. In: proceedings of the 2nd International Conference on Technology and Instrumentation in Particle Physics (TIPP 2011), Phys. Proc. 37 1892 (2012).
- [24] Rick Bitter, Taqi Mohiuddin, and Matt Nawrocki. LabVIEW: Advanced programming techniques. Crc Press, 2006.
- [25] G. Saviano et al. “Properties of potential eco-friendly gas replacements for particle detectors in high-energy physics”. In: Journal of Instrumentation 13 (2018), P03012.
- [26] Archana Sharma. “Properties of some gas mixtures used in tracking detectors”. In: SLAC-J-ICFA-16-3, SLAC-JOURNAL-ICFA-16-3 (July 1998).
- [27] X. Fan et al. “Precise measurement of gas parameters in a realistic RPC configuration: The currently used R134a gas and a potential alternative eco-gas”. In: Nuclear Instruments and Methods in Physics Research Section A: Accelerators, Spectrometers, Detectors and Associated Equipment 1024 (2022), p. 166124. issn: 0168-9002. doi: <https://doi.org/10.1016/j.nima.2021.166124>. url: <https://www.sciencedirect.com/science/article/pii/S0168900221010202>.



- [28] G. Rigoletti et al. “Studies of RPC detector operation with eco-friendly gas mixtures under irradiation at the CERN Gamma Irradiation Facility”. In: Proceedings of Science 364 (2020).
- [29] M. Kang et al. “Study of eco-friendly gas mixtures for SHiP RPCs”. In: J. Korean Phys. Soc. 80 (2022), pp. 1–12.
- [30] G. Proto et al. “On a new environment-friendly gas mixture for Resistive Plate Chambers”. In: JINST 17 (2022), P05005.
- [31] S. Agostinelli et al. “Geant4 a simulation toolkit”. In: Nucl. Instr. Meth. A 506(3) (2003), pp. 250–303.
- [32] Chris Hagmann, David Lange, and Douglas Wright. “Cosmic-ray shower generator (CRY) for Monte Carlo transport codes”. In: 2007 IEEE Nuclear Science Symposium Conference Record. Vol. 2. 2007, pp. 1143–1146. doi: 10.1109/NSSMIC.2007.4437209.
- [33] P. Stowell et al. “Figures of Merit for the Application of Muon Tomography to the Characterization of Nuclear Waste Drums”. In: WM2019 conference proceedings (2019).
- [34] A. Alrheli et al. “A Muon Scattering Tomography Method for Verification of Fuel Assemblies Stored in V/52CASTOR”. In: WM2021 conference proceedings (2021).
- [35] M. Dobrowolska et al. “A novel technique for finding gas bubbles in the nuclear waste containers using Muon Scattering Tomography”. In: Journal of Instrumentation 13.05 (May 2018), P05015–P05015. doi: 10.1088/1748-0221/13/05/p05015.
- [36] M. Mhaidra et al. “A Robust Method to Find Gas Bubbles Inside Large Nuclear Waste Containers Using Muon Tomography”. In: WM2021 conference proceedings (2021).
- [37] M. Weekes et al. “Material Identification of Bodies Stored in Nuclear Waste Drums using Muon Scattering Tomography and Machine Learning”. In: WM2021 conference proceedings (2021).
- [38] M.J. Dobrowolska et al. “Towards an application of muon scattering tomography as a technique for detecting rebars in concrete”. In: Smart Materials and Structures 29 (2020).

9. Appendix



9.1 The system

EPJ Web of Conferences **225**, 06008 (2020)
ANIMMA 2019

<https://doi.org/10.1051/epjconf/202022506008>

Non-destructive assay of nuclear waste containers using muon scattering tomography in the Horizon2020 CHANCE project

Anna Kopp^{1*}, Ahmad Alrheli², Daniel Kikoła³, Mohammed Mhaidra^{1,3}, Patrick Stowell²,
Holger Tietze-Jaensch⁴, Lee Thompson², Jaap Velthuis¹, Michael Weekes²

¹ School of Physics, University of Bristol, UK

² Department of Physics and Astronomy, University of Sheffield, UK

³ Warsaw University of Technology, Poland

⁴ Forschungszentrum Jülich, Germany

* anna.kopp@bristol.ac.uk

Abstract—Methods for the non-destructive assay of nuclear waste drums are of great importance to the nuclear waste management community, especially where loss in continuity of knowledge about the content of drums happened or chemical processes altering the contents of the drums may occur. Muon scattering tomography has been shown to be a promising technique for the non-destructive assay of nuclear waste drums in a safe way. By measuring tracks of muons entering and leaving the probed sample and extracting scattering angles from the tracks, it is possible to draw conclusions about the contents of the sample and its spatial arrangement. Within the CHANCE project, a newly built large-scale mobile detector system for scanning and imaging the contents of nuclear waste drums using atmospheric muons is currently undergoing commissioning.

I. INTRODUCTION

Non-destructive methods to assay nuclear waste drums are of great interest to the nuclear waste management community. It has been observed that chemical processes like oxidation of metals may occur within drums, possibly leading to the formation of gas bubbles or cracks. Furthermore, knowledge about the contents of legacy waste drums is not always preserved. Muon scattering tomography (MST) is a promising technique to address these problems. It allows to scan and image nuclear waste drums in a safe, non-destructive way using natural background radiation. Compared to other methods like X-ray or gamma-ray scanning it does not introduce additional artificial radiation or any additional hazards to personnel or equipment. Fitting the tracks of muons entering and leaving the probed sample allows to reconstruct approximated scattering vertices and to e.g. differentiate between various materials.

II. MUON SCATTERING TOMOGRAPHY

Muon scattering tomography uses secondary cosmic radiation to probe volumes from a safe distance. Compared to other scanning methods using e.g. X-rays or gamma rays it does not rely on a radiation source but uses atmospheric muons, particles resulting from primary cosmic radiation. These are ubiquitous and abundant at a rate of about 10 000/(m²minute) at sea level, spread over a wide range of momenta and

incidence angles. Muons are highly penetrating particles; it is almost impossible to stop them and they are thus ideally suited for scanning nuclear waste drums, where the nuclear waste is often embedded in concrete.

As charged particles, they undergo multiple Coulomb scattering processes when traversing matter. The projected scattering angle distribution depends on the atomic number Z of the traversed material and can be approximated as a Gaussian distribution [1] with mean zero and a standard deviation σ_μ of

$$\sigma_\mu \approx \frac{13.6 \text{ MeV}}{pc\beta} \sqrt{X/X_0(1 + 0.038 \ln(X/X_0))}, \quad (1)$$

where p is the muon's momentum, βc its velocity, X the thickness of the scattering material and X_0 the material-specific radiation [2] length given by

$$X_0 \approx \frac{A \cdot 716.4 \text{ g/cm}^2}{Z(Z+1) \ln(287/\sqrt{Z})}. \quad (2)$$

Here, A is the atomic weight given in g/mol. As can be seen from equations 1 and 2, the width of the projected scattering angle distribution varies approximately with Z , making the technique particularly sensitive to materials with high atomic numbers.

Thus scattering angles from muons scattering off materials with large atomic numbers Z are more likely to be large than those from scatters in low- Z materials.

By placing multiple detector planes above and below the probed sample and measuring where the muons hit these, the trajectories of the incoming and outgoing muons are reconstructed and fitted. A scattering vertex is then reconstructed where these two trajectories meet. The assumption here that for each muon all scattering processes happen in the same location, the vertex, is not strictly correct but has been shown to be a good approximation. Scattering angles for all muons are derived from their fitted tracks.

Then, the volume under investigation is divided into voxels as described in ref. [4]. In each voxel with at least N



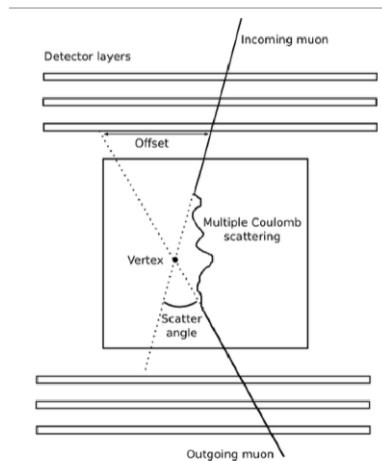


Fig. 1. Illustration of the muon trajectory and the reconstructed scattering vertex [3].

reconstructed vertices, a metric discriminator m_{ij} is calculated for each pair of tracks i and j of the N most scattered tracks,

$$m_{ij} = \frac{\|v_i - v_j\|}{\langle \theta_i p_i \rangle \langle \theta_j p_j \rangle} \quad (3)$$

Here, v_i is the location of the vertex pertaining to muon track i with momentum p_i and θ_i is the associated scattering angle. The median of this weighted metric distribution per voxel is an indicator of the predominant material in that voxel: large values are more likely to result from materials with high Z than from materials with low Z .

In the past, this has been exploited for various discrimination and identification studies in simulation: to differentiate between different high- Z materials [3], [5] or to locate gas bubbles in bitumen-filled drums [6].

III. THE CHANCE PROJECT

The CHANCE project ("Characterization of conditioned nuclear waste for its safe disposal in Europe", <http://www.chance-h2020.eu>), is funded by the EU's Horizon2020 research programme. It started on June 1st 2017, runs over 4 years and has 11 partners in 7 countries. Collaborators include universities and research institutes as well as government agencies and industrial partners. Within the project, three different techniques to assay nuclear waste drums in non-destructive ways are investigated: calorimetry, muon scattering tomography and cavity ring down spectroscopy.

IV. MUON SCATTERING TOMOGRAPHY WITHIN THE CHANCE PROJECT

Three universities mainly contribute to the MST program within CHANCE: University of Sheffield, University of Bristol, both in the UK and Warsaw University of Technology, Poland. A large, mobile muon scattering tomography detector shown in figure 2 has been recently built in a non-laboratory environment outside of Bristol, UK. It is placed in a building, so it is rain-protected but the building is neither temperature nor humidity-controlled. Thus the environmental conditions are the same as they are likely to be in an actual field deployment. The active area measures approximately $1.8 \times 1.8 \text{m}^2$. As the detector system is modular, it is easy to dis- and reassemble and even to change the configuration to adapt it to the requirements in a potential deployment.

The detector system combines two different kinds of gas detectors, namely drift chambers and resistive plate chambers (RPCs). A coincidence between two layers of plastic scintillators is used as trigger to start the read-out process.

The RPCs were designed and built at University of Bristol. A smaller prototype of these chambers has been operated on a mixture of freon (R134-a) and isobutane in the past. Due to recent legislation restricting the usage of freon, the chambers are currently run on CO_2 . Other, environmentally friendly gas mixtures will be tested in the future. The drift chambers are operated on a mix of methane, argon and CO_2 . They were built at University of Sheffield.

During the construction of the detector system the data analysis effort had been focussed on simulation studies. The detector layout was optimized and a figure of merit was developed for comparing the smallest observable separations between features or the smallest observable features in concrete-filled waste drums using different reconstruction algorithms [7]. The latter is especially relevant considering the heterogeneity of real nuclear waste drums. Commissioning of the full detector system has started in early June and is ongoing, with first test data having been taken. Full data taking is expected to start soon while further simulation studies are continuing in parallel.

The Detector System

Both RPCs and drift chambers provide information in 3D space about where a muon hit the detector. As the muon traverses a detector chamber, the gas inside it gets ionized. With a high voltage applied between the top and bottom side for the RPCs or the anode wire and cathode for the drift chambers, respectively, this creates a signal, which is read out and digitized. The spatial resolution of the RPCs is in the sub-millimeter range [8], while that of the drift chambers is in the order of mm. The time resolution for RPCs with a 2mm gap as the ones used here is on the order of nanoseconds.

In both the detector stack above and below the sample space, two space points from the RPCs and three from the drift chambers are measured and read out. Hence it is possible to fit tracks and extract scattering angles with high precision. The detectors are fast, with data acquisition per event taking

EJWC Web of Conferences **225**, 06008 (2020)
ANIMMA 2019

<https://doi.org/10.1051/epjconf/202022506008>

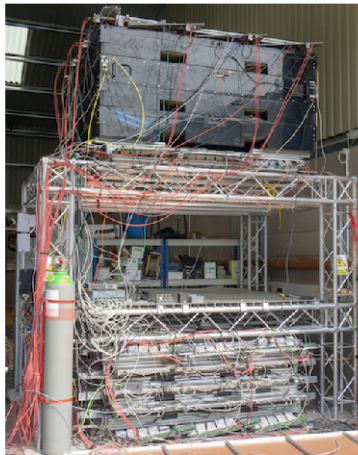


Fig. 2. The muon scattering tomography detector system of the CHANCE project. Shown are the detector systems above and below the empty sample space consisting of three layers of drift chambers and two RPC layers. The top stack additionally contains two layers of plastic scintillators used as triggers. The detectors cover an area of approximately 1.8 × 1.8 m².

on the order of a few 10 μ s and have a low cost per unit area, making them ideal for large-scale detectors. For both the RPCs and drift chambers, three individual detectors with widths of 58 and 60 cm, respectively, are placed next to each other to cover the whole active area. The support structure holding the individual chambers can be seen as empty space in the data as shown for one layer of RPCs in figure 3. Since the footprint of the active area is larger than the drums that will be scanned, it is nonetheless possible to scan whole drums and avoid dead areas by moving the drum to different locations within the sample space.

V. CONCLUSIONS AND OUTLOOK

Muon scattering tomography is a non-destructive technology well suited to investigate the contents of nuclear waste drums in a safe way, without introducing any additional radiation to the samples or personnel. A large, mobile MST detector has been built in a non-laboratory environment close to Bristol, UK, within the CHANCE project and first test data have been taken. Once the detector system is fully commissioned, full data taking will commence.

As the scattering behavior of atmospheric muons in many materials is well known from simulation studies, data with blocks of high-Z materials like lead or tungsten will be taken in a first step. Subsequently, ‘blind tests’ with drums mimicking nuclear waste drums will be carried out. Our collaboration partners at SCK-CEN, Belgium, filled drums

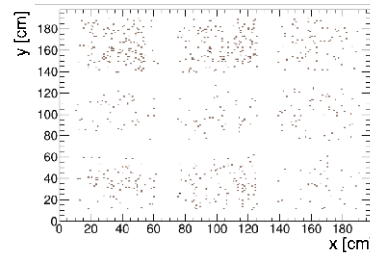


Fig. 3. Hits in one layer of RPCs. The pattern is due to the support structure holding the individual detector chambers. Each entry corresponds to one hit, showing the x and y coordinates.

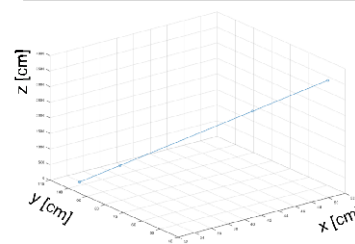


Fig. 4. Muon track fitted through all four layers of RPCs. No sample is placed between the upper and lower detectors so no scattering is expected or seen.

with non-radioactive materials otherwise similar to what could be found in nuclear waste drums but did not reveal the contents. Scanning the drums and applying the reconstruction algorithm described above will then show their contents. The access and application to real waste drums is currently being investigated.

ACKNOWLEDGMENT

This project has received funding from the European Union’s Horizon2020 research and innovation programme under grant agreement number 755371.

REFERENCES

[1] M. Tanabashi et al., “Review of particle physics,” *Phys. Rev. D*, vol. 98, p. 030001, Aug 2018. [Online]. Available: <https://link.aps.org/doi/10.1103/PhysRevD.98.030001>
 [2] T. A. Lainsky et al., “Review of particle properties particle data group,” *Rev. Mod. Phys.*, vol. 45, pp. S1-S175, Apr 1973. [Online]. Available: <https://link.aps.org/doi/10.1103/RevModPhys.45.S1>

EPJ Web of Conferences **225**, 06008 (2020)
ANIMMA 2019

<https://doi.org/10.1051/epjconf/202022506008>

- [3] L. Frazão, J. Velthuis, C. Thomay, and C. Steer, "Discrimination of high-z materials in concrete-filled containers using muon scattering tomography," *Journal of Instrumentation*, vol. 11, no. 07, pp. P07020–P07020, Jul 2016. [Online]. Available: <https://doi.org/10.1088/1748-0221/11/07/p07020>
- [4] C. Thomay, J. J. Velthuis, P. Baesso, D. Cussans, P. A. W. Morris, C. Steer, J. Burns, S. Quillin, and M. Stapleton, "A binned clustering algorithm to detect high-z material using cosmic muons," *Journal of Instrumentation*, vol. 8, no. 10, pp. P10013–P10013, Oct 2013. [Online]. Available: <https://doi.org/10.1088/1748-0221/8/10/P10013>
- [5] C. Thomay, J. Velthuis, T. Poffley, P. Baesso, D. Cussans, and L. Frazão, "Passive 3d imaging of nuclear waste containers with muon scattering tomography," *Journal of Instrumentation*, vol. 11, no. 03, pp. P03008–P03008, Mar 2016. [Online]. Available: <https://doi.org/10.1088/1748-0221/11/03/p03008>
- [6] M. Dobrowolska, J. Velthuis, L. Frazão, and D. Kikola, "A novel technique for finding gas bubbles in the nuclear waste containers using muon scattering tomography," *Journal of Instrumentation*, vol. 13, no. 05, pp. P05015–P05015, May 2018. [Online]. Available: <https://doi.org/10.1088/1748-0221/13/05/p05015>
- [7] J. Stowell, J. Velthuis, H. Tietze-Jaensch, A. Kopp, A. Alrheli, M. Mhaidra, L. Thompson, and D. Kikola, "Figures of merit for the application of muon tomography to the characterization of nuclear waste drums," *Waste Management Symposia 2019*, no. 19253, March 2019.
- [8] P. Baesso, D. Cussans, C. Thomay, and J. Velthuis, "Toward a RPC-based muon tomography system for cargo containers," *Journal of Instrumentation*, vol. 9, no. 10, pp. C10041–C10041, Oct 2014. [Online]. Available: <https://doi.org/10.1088/1748-0221/9/10/c10041>



9.2 Figure of Merit Studies

WM2019 Conference, March 3 - 7, 2019, Phoenix, Arizona, USA

Figures of Merit for the Application of Muon Tomography to the Characterization of Nuclear Waste Drums-19253

Patrick Stowell *, Ahmad Alrheli *, Daniel Kikola ****, Anna Kopp **, Holger Tietze-Jaensch ***, Mohammed Mhaidra ****, Lee Thompson *, Elie Valcke *****, Jaap Velthuis **, Michael Weckes *

* University of Sheffield

** University of Bristol

*** Forschungszentrum Jülich GmbH

**** Warsaw University of Technology

***** SCK·CEN, Belgian Nuclear Research Centre

ABSTRACT

Muon Tomography (MT) has been shown to be a viable candidate for the assay of nuclear storage containers. In this paper we present the development of methods to calculate Figures Of Merit for different MT systems and algorithms based on their ability to image and separate small objects inside legacy nuclear waste drums. These testing methods are then applied to three different tomography algorithms to understand how different cosmic ray muon exposure times and target materials can affect performance.

INTRODUCTION

Significant potential of MT has been discussed recently in combination with the numerical forecast of Spent Nuclear Fuel (SNF) properties propagation depending on the reactor operational history parameters [1]. Namely for the medium to long-term dry-cask storage of SNF, the possibility of non-destructive assay of very large volume and heterogeneous waste containers has been identified of considerable relevance. By reconstructing the trajectories of muons both entering and exiting a volume of interest, a 3D density map can be built from the reconstructed scattering angle distributions. This technique is therefore particularly useful when imaging shielded containers where discontinuity of knowledge or loss of pointer cannot be ruled out, capable of non-destructively confirming the contents of a container whilst avoiding the cost and safety concerns involved with explicitly opening it. The European Commission has recently granted R&D funds to the CHANCE Horizon-2020 project [2, 3] to develop a mobile muon tomography system for nuclear waste characterization of (large volume) heterogeneous rad-waste and storage containers.

It has already been demonstrated that this technique is capable of discriminating nuclear materials inside a concrete support matrix [4]. However, work is still needed to understand the different experimental factors that can affect material discrimination. In particular, a suitable Figure Of Merit (FOM) is needed for waste characterization that can be used to compare the performance of competing detector systems and algorithms for the detection and evaluation of radioactive material hidden inside large waste volume containers. In the past, Receiver Operating Characteristic (ROC) curves have been used to understand the performance of automated binary classifiers that search for uranium in cargo crates without human. Whilst these automated decisions could be used to flag storage containers with higher than expected density "hotspots", the interpretation of the reconstructed 3D density map also provides important information. For example, a low density irregularity in the concrete matrix, or a warping of a cask support structure, may mean the container needs to be flagged for additional study, despite passing a simple nuclear material binary classification. It is therefore necessary to develop additional FOMs that encapsulate how the intrinsic detector resolution, and choice of tomography algorithm, can impact the detail in a reconstructed density map. We present our work on the application of "optical" resolution tests (see [5]) to understand size and feature resolution in a muon tomography system.

WM2019 Conference, March 3 - 7, 2019, Phoenix, Arizona, USA

By imaging test objects with decreasing features sizes, the number of easily distinguishable objects is an indicator of the resolution of a given tomography technique when interpreting the output density matrix. This method allows comparisons to be made between significantly different algorithms by converting their qualitative outputs into discrete figures of merit.

First a number of different muon tomography algorithms are reviewed, before a detailed Monte-Carlo (MC) simulation of muons scattering inside nuclear waste drums is described. A method to quantify the resolution of tomography algorithm is then developed, before being used to understand the feature and size resolution of available imaging techniques as a function of exposure time and target materials.

MUON TOMOGRAPHY ALGORITHMS

Three commonly used muon tomography algorithms, the simple Point-of-Closest Approach, the Angle Statistics Reconstruction, and the Binned Clustering Algorithm, are considered in this work. Each of these algorithms divide the volume of interest up into a 3D grid of cubic voxels with a side length of 1cm. A discriminator score is then derived from all muon trajectories that pass through a given voxel so that regions of high and low density can be mapped inside a waste drum.

The Point-of-Closest Approach (PoCA) algorithm [6] simply assumes that any muon must have undergone a single scattering inside the volume of interest. Since large scattering angles indicate the presence of high density materials, each voxel is weighted by the median angle of all muon trajectories whose point of closest approach is inside the given voxel. This is one of the simplest muon tomography algorithms available but benefits from being the least computationally intensive.

The Binned Clustering (BC) algorithm [4] assumes that in low density material, scattering vertices inside a single voxel will be more distributed than in high density materials such as uranium. A high momentum muon is also more likely to undergo large scatters only when passing through a dense material. A discriminator is calculated based on these two assumptions by calculating the metric distance between pairwise combinations of different muon points of closest approach, r , inside a voxel.

$$m_{ij} = \frac{\|\vec{r}_i - \vec{r}_j\|}{\theta_i p_i \theta_j p_j}$$

Where \vec{r}_i is the point-of-closest approach for muon i , and θ_i and p_i is the muon scattering angle and momentum respectively. The median of all calculated metric distances in each voxel can be used to discriminate different materials. Since the metric distances are calculated from pairwise combinations of vertices, the median varies as a function of the number of tracks in a voxel. To ensure voxels are comparable to one another only the first N_r most scattered tracks are included in the median calculation. The choice of N_r is derived from the maximum value in which a block of steel is easily resolvable after 8 days of cosmic ray exposure in a given detector. The choice of N_r for all other exposures is chosen so that the discriminator value of steel is constant as a function of exposure. This corresponds to $N_r = 6$ for 4 days exposure, $N_r = 12$ for 8 days exposure, $N_r = 24$ for 16 days exposure, and $N_r = 38$ for 25 days exposure. Since the BC algorithm considers the spatial distribution of vertices within a voxel it can be sensitive to high density features that are smaller than the chosen voxel size.

In reality, as a muon traverses a waste drum, it is more likely to undergo a number of small scatters instead of a single large, localized scatter as assumed in the PoCA algorithm. The PoCA algorithm is therefore prone to additional noise if a muon trajectory is mis-reconstructed so that it appears as an extreme scattering vertex inside a single voxel. The Angle Statistics Reconstruction (ASR) algorithm [7] tries to account for this by considering all voxels that lie within a chosen minimum range of the muon trajectories reconstructed before and after the volume of interest. This removes the assumption that a muon scatters inside only a single voxel, leading to reduced noise in the output density map.

WM2019 Conference, March 3 - 7, 2019, Phoenix, Arizona, USA

A set of scores $s_1 = \theta_{xp}$ and $s_2 = \theta_{yp}$ are calculated from the scattering angles in the X and Y dimension and added to a distribution of scores inside each voxel within 10 mm of the incoming and outgoing muon trajectories. The 75% quantile of each voxel distribution is then assigned as a discriminator score to identify voxels where high density features may be present.

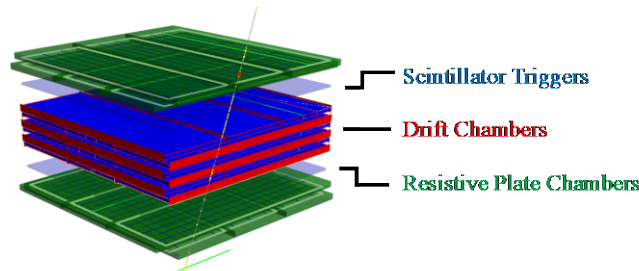


Figure 1. Diagram of the muon tracking system simulated in this study. The geometry represents a system currently being commissioned at the University of Bristol for the CHANCE H2020 project. The scintillator trigger panels provide an indicator of a muon passing through the system, whilst the drift chambers and resistive plate chambers record the hit positions of the muon as it traverses the system.

MONTE-CARLO SIMULATIONS

The performance of each muon tomography algorithm discussed in the previous section was evaluated by applying them to MC simulations data of cosmic ray muons passing through a typical 88 cm high and 57 cm wide nuclear waste drum filled with concrete. The detector was built in the GEANT4 high energy particle physics simulation package as a representation of a system currently being commissioned at the University of Bristol for the CHANCE Horizon-2020 project. The system consists of two identical detector systems placed 105 cm apart, above and below the volume of interest. Each individual detector system consists of 6 layers of drift chambers (~2 mm resolution) and 4 layers of resistive plate chambers (0.3 mm resolution), providing 10 muon trajectory hit points in total, 5 in the X plane, and 5 in the Y plane. These hit points are used to reconstruct the muon trajectory above and below the volume to be scanned.

To compare the outputs of each of the algorithms discussed in the previous section, a waste drum containing a 10 cm cube of uranium surrounded in concrete was simulated for an extreme case of 25 days of cosmic ray muon exposure. Muons were generated using the CRY cosmic ray generator library. This resulted in over 40 million muon tracks reconstructed in the detector at sea level. The reconstructed muon tracks were passed into each of the algorithms discussed in the previous section to produce reconstructed density maps. The output density maps for each algorithm are shown in Figure 3 for 25 days exposure. After 25 days, each algorithm provides a clear identification of the central Uranium feature, although the PoCA algorithm has significantly reduced contrast compared to the other algorithms. The ASR algorithm images the drum with the greatest clarity, as assigning weights to multiple voxels avoids outlier events with extreme scattering angles introducing noise into the plots. However, this same weighting procedure leads to a stretching of the outside of the drum as regions on the edge of the detector acceptance prefer highly scattered tracks where multiple voxels would be filled.

WM2019 Conference, March 3 - 7, 2019, Phoenix, Arizona, USA

Whilst these comparisons demonstrate the feasibility of each muon tomography imaging techniques, they offer limited quantifiable information on the performance of each individual algorithm. Since the outputs of each algorithm are so different it is not possible to compare the discriminator values from each one directly. Therefore, in the following sections, a method to quantify the feature and size resolution for each imaging technique is presented to aid detector and algorithm optimization.

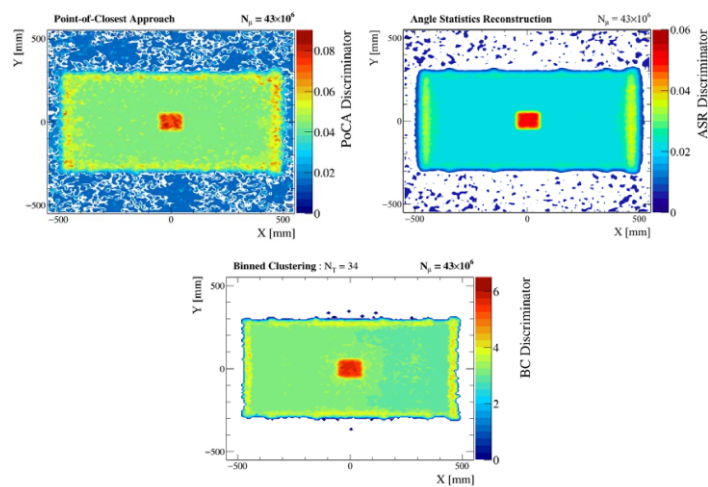


Figure 2. Comparison of the different algorithm outputs when imaging a 10 cm long Uranium cube for 25 days of muon exposure. The inclusion of momentum information and metric distances in the BC algorithm leads to an image with higher contrast and clarity than a simple PoCA approach.

FEATURE AND SIZE RESOLUTION

In this section two figure of merit tests are developed so that the imaging performance of the algorithms considered so far can be compared to one another. A feature resolution test is developed to understand an algorithms ability to separate distinguish high density objects in close proximity to one another. A size resolution test is developed to understand the smallest object that can be observed by a given tomography algorithm.

To understand feature resolution, an array of 20 cuboid uranium target objects was simulated, each with sides of 10 cm in the Y and Z dimension. Starting at a X dimension thickness of 10 cm, the thickness and spacings in the X dimension are reduced by a factor of 75% for each successive target object as shown in Figure 3. Scanning from left to right, the number of observable features gives a metric for the smallest observable feature and separation combination achievable when the given analysis technique is applied to the muon trajectories reconstructed in the detector under consideration. If N_o is the number of objects clearly observable, the minimum feature size is

$$x_{min} = 10 \text{ cm} \times 0.75^{N_o-1}$$

WM2019 Conference, March 3 - 7, 2019, Phoenix, Arizona, USA

Figure 3 shows the output density maps for each algorithm after 25 days of cosmic ray muon exposure when taking a slice through the 3D density map along the centre of the drum. To remove human bias when reading the outputs from each algorithm, the quantity N_o can be inferred by calculating the average discriminator values in the signal and background slices for each object. In this study the background slice is taken as the slice of concrete immediately to the right of each target object.

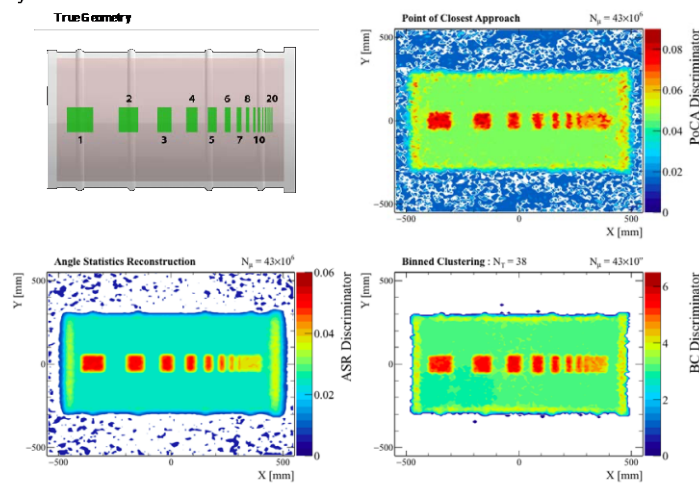


Figure 3. Uranium feature resolution test images after 25 days of simulated cosmic ray exposure. The number of observable objects gives an indicator on the resolution of each imaging technique. It is only possible to observe 6 separated objects using the PoCA algorithm, whilst the ASR and BC algorithms can both make out an additional feature.

As shown in Figure 4, as the feature size becomes smaller, it becomes more difficult to clearly separate the signal and background slices based on their discriminator values. The point of convergence of these two histograms can be used to infer the maximum number of clearly observable features in each density map.

WM2019 Conference, March 3 - 7, 2019, Phoenix, Arizona, USA

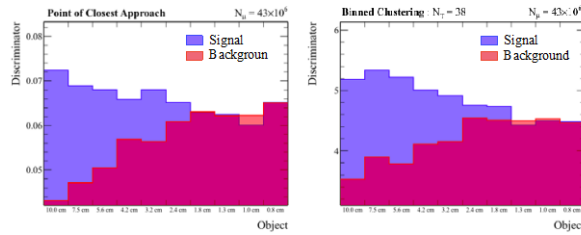


Figure 4. Comparison of the average discriminator in signal and background slices for the PoCA and BC algorithms. The smallest “observable” feature is inferred from the point where the signal discriminator becomes comparable to the background. This is 2.4 cm and 1.8 cm for the PoCA and BC algorithms respectively.

All algorithms considered find it difficult to easily separate features smaller than 1.6 cm. Whilst they can identify there is a region of higher density at high X, they cannot distinguish individual sheets of uranium. The PoCA algorithm with its higher inherent noise can also only observe 6 clear objects, corresponding to a feature resolution of $x_{min} = 1.8$ cm, almost double the voxel size. If a muon undergoes a number of additional small scatters as it leaves the high density target material, the scattering vertex can be reconstructed just outside of the target. This mixing effect leads to the high density objects merging in the output density maps when they are placed in close proximity. It is also worth pointing out that as the size of the Uranium cuboids decreases, so does the average discriminator in the ASR map, showing a discriminator value comparable to steel for the smallest objects. The PoCA and BC algorithms however both show regions with high discriminators despite their ability to finely separate the presence of individual uranium sheets.

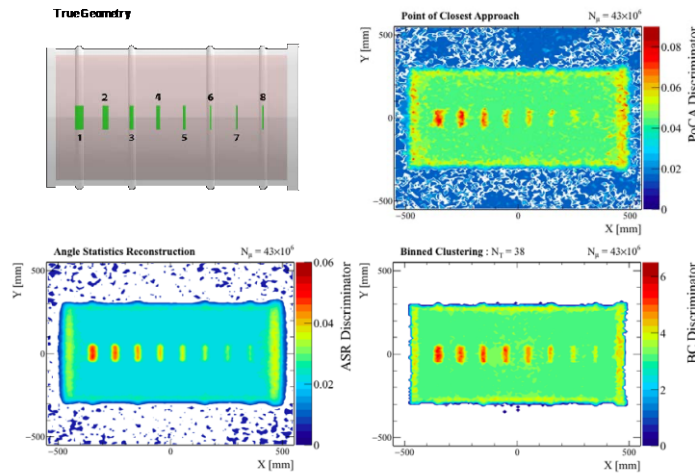


Figure 5. Uranium size resolution test images after 25 days of simulated cosmic ray exposure. The number of observable objects gives an indicator on the resolution of each imaging technique. Noise in the PoCA algorithm outputs means it is difficult to clearly identify the four smallest target objects.

WM2019 Conference, March 3 - 7, 2019, Phoenix, Arizona, USA

To understand size resolution, an array of 8 cuboid uranium target objects was simulated, each with sides of 10 cm in the Y and Z dimension. Starting at a X dimension of 3 cm, the thickness in the X dimension is then scaled by a factor of 75% for each successive target object, as shown in Figure 5, whilst the object spacing is kept fixed. Scanning from left to right, the number of observable features gives a metric for the smallest observable feature when objects are not in close proximity to one another. If N_0 is the number of objects clearly observable, the smallest observable object is given by

$$S_{min} = 3 \text{ cm} \times 0.75^{N_0 - 1}$$

As shown in Figure 5, the PoCA algorithm is only capable of clearly resolving 5 objects, corresponding to a smallest observable object of 0.95cm, comparable to the voxel size. In contrast, the ASR and BC algorithms both show much cleaner, rectangular features for all 8 objects, resolving the presence of a target object down to 4mm.

EXPOSURE/MATERIAL DEPENDENCE

Using a standardized figure of merit procedure like that defined in the previous section it is possible to quickly evaluate how detector performance may change different operating conditions. Figure 6 shows a comparison of the BC output density maps for the feature and size resolution tests after shorter cosmic ray exposures. After 4 days of exposure, noise in the density maps means only 5 objects are clearly distinguishable, whilst little difference is found between 16 and 25 days of exposure. This highlights that eventually a statistical limit is reached in which the output image is constrained only by the angular resolution of the detector itself.

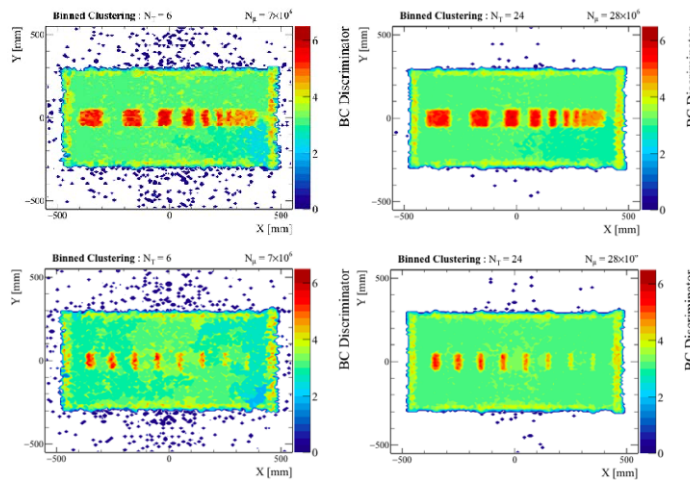


Figure 6. Uranium feature (top) and size (bottom) resolution test images after 4 days (left) and 16 days (right) of simulated cosmic ray exposure. The feature and size resolution improves with longer exposure times, eventually reaching a limit where the detector angular resolution defines the minimum observable feature.

WM2019 Conference, March 3 – 7, 2019, Phoenix, Arizona, USA

Since the number of highly scattered vertices is material dependent, so is the detector resolution, with small objects of lower density materials having fewer reconstructed scattering vertices that can be used to build a discriminator. This is evident in Figure 7, where the BC algorithm is applied to the tests derived in the previous section but with lead and steel replacing the target object material. As the density increases so does the ability to distinguish close proximity features from one another, with only 5 objects ($x_{min} \sim 3.2$ cm) and 4 objects ($x_{min} \sim 4.2$ cm) being observable in lead and steel respectively. Similarly, even when the spacing between objects is large, the size resolution is strongly dependent on the target material, with only 6 lead objects being distinguishable from the background ($S_{min} \sim 0.7$ cm), and no steel objects being distinguishable from background.

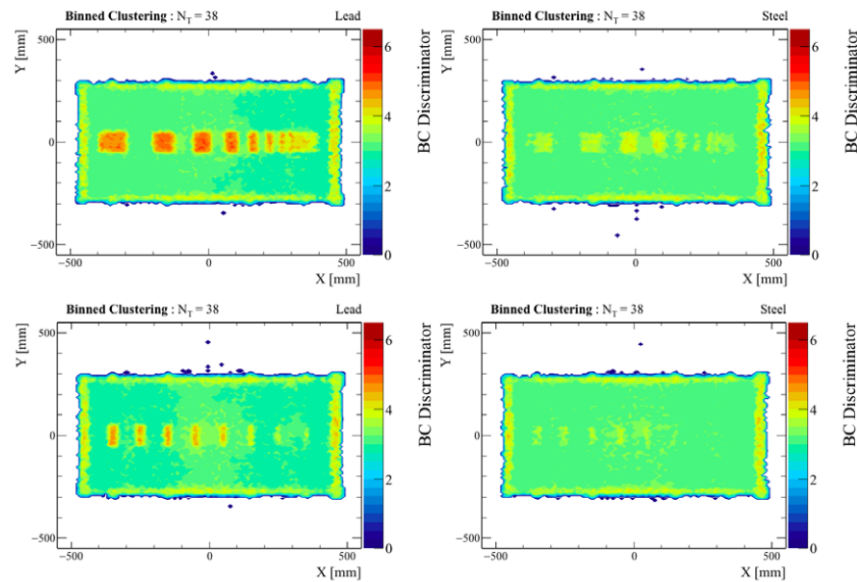


Figure 7. Uranium feature (top) and size (bottom) resolution test images for lead and steel targets. The resolution has a strong correlation with the target material density as the presence of higher density materials results in more scattering vertices in the volume of interest.

CONCLUSIONS

The figure of merit tests developed here make it possible to directly compare the imaging performance of different muon tomography techniques. This can be used to optimize algorithms and detector designs, but also provides a standardized figure of merit that can be used to quantitatively assess the benefits of different analysis techniques. Future work will focus on using these tests to understand the correlation between material dependence and algorithm performance, whilst simultaneously working towards an experimental application of these figure of merit tests to a real muon tomography detector prototype currently being commissioned for the CHANCE Horizon-2020 project.

WM2019 Conference, March 3 – 7, 2019, Phoenix, Arizona, USA

REFERENCES

- [1] Tietze-Jaensch, H., Fast, I., Frazao, L., Velthuis, J. (2018). Numerical Assessment of SNF Parameter Bandwidths and Muon Tomography Assay for Large Volume Casks. *WM2018 Conference, March 18 – 27, 2018, Phoenix, Arizona, USA, paper #18185*
- [2] CHANCE 2020 : <http://chance-h2020.eu>
- [3] Ricard, D., Plumeri, S., Boucher, L., Rizzo, A., Tietze-Jaensch, H., Mathonat, C., Bruggeman, C., Velthuis, J., Thompson, L., Genoud, G., Bucur, C., Kikola, D., Zakrzewska-Koltuniewicz, G. (2018). The CHANCE project “Characterization of conditioned nuclear waste for its safe disposal in Europe”. *DEM 2018 - Dismantling Challenges: Industrial Reality, Prospects and Feedback Experience, France, Avignon – 2018, October 22 – 24*
- [4] Thomay, C., Velthuis, J. J., Baesso, P., Cussans, D., Morris, P. A. W., Steer, C., ... & Stapleton, M. (2013). A binned clustering algorithm to detect high-Z material using cosmic muons. *Journal of Instrumentation*, 8(10), P10013.
- [5] Camera Optics ISO Testing : <https://www.techradar.com/news/photography-video-capture/cameras/camera-testing-resolution-charts-explained-1027585>
- [6] Jonkmans, G., Anghel, V. N. P., Jewett, C., & Thompson, M. (2013). Nuclear waste imaging and spent fuel verification by muon tomography. *Annals of Nuclear Energy*, 53, 267-273.
- [7] Stapleton, M., Burns, J., Quillin, S., & Steer, C. (2014). Angle Statistics Reconstruction: a robust reconstruction algorithm for Muon Scattering Tomography. *Journal of Instrumentation*, 9(11), P11019.

ACKNOWLEDGEMENTS

This work was funded jointly by the European NFRP7 program, grant no. 755371 (CHANCE project), and the UK STFC NuSec network.

9.3 Use of the CNR method in muon tomography

WM2021 Conference, 8 - 12 March 2021, Phoenix, Arizona, USA

A Muon Scattering Tomography Method for Verification of Fuel Assemblies Stored in V/52 CASTOR 21123

Ahmad Alrheli*, Anna Kopp **, Daniel Kikola***, Chiara De Sio**, Dominic Barker*, Mohammed Mhaidra***, Patrick Stowell*, Lee F. Thompson*, Jaap Velthuis**, Michael Weekes*

* University of Sheffield, Department of Physics and Astronomy, UK
** University of Bristol, School of Physics, UK
*** Warsaw University of Technology, Poland

ABSTRACT

Muon Scattering Tomography (MST) has been reported as a powerful technique for imaging well-shielded or hidden objects. In this paper, we present the application of the MST technique to investigate a large nuclear waste cask, namely, a CASTOR V/52. Furthermore, we develop and evaluate the use of the projected scattering angle method for imaging a large nuclear waste cask. Contrast-to-Noise Ratio values are calculated to examine the ability of the algorithmic methods used to monitor and image the fuel assemblies inside the CASTOR cask. These values are compared at different regions inside the cask, such as the region that contains a fully loaded basket and the region that contains an empty basket, to evaluate the method quantitatively.

INTRODUCTION

Muon Tomography (MT) in both scattering and transmission modes has been shown to be a valuable method for nuclear waste characterisation. The efficacy of using MT as an imaging method for well-shielded objects is ascribed to the higher penetrating level of cosmic muons compared with that of conventional methods, such as X-rays. The non-artificial source of cosmic muons and the great availability of $10,000 \text{ muons m}^{-2} \text{ min}^{-1}$ at sea level constitute some of the benefits of MT technology. Moreover, in the nuclear waste industry, MT makes possible the non-invasive assay of nuclear waste packages, reduces the costs involved in opening them and mitigates concerns of exposure to radiation. As the MT technique relies on a shower of cosmic muons, the muons' tracks are reconstructed as they enter and exit the investigation area by placing muon detectors above and below them. This study is part of the EU H2020-funded CHANCE project that aims to develop several non-destructive techniques, including MT detector systems, to investigate the interior of heterogeneous conditioned radioactive waste inside nuclear waste packages [1,2].

In recent years, many studies have demonstrated good performance of the MT method in distinguishing materials that have high atomic numbers (Z) from shielding materials, such as uranium cubes, inside a cemented nuclear waste drum [3]. Nonetheless, extended studies need to be done to understand the different factors that might affect MT performance, e.g., a thicker and higher-density shielding matrix. Studying the reconstructed images of the materials of interest quantitatively enables us to understand the limitations of each algorithmic method. For instance, simple regional classification can be done in the results to group the different regions, that is, which region contains a high-Z material and which only contains background signal. In particular, the Contrast-to-Noise Ratio (CNR) is a statistical method that could be used to evaluate the ability of several algorithmic methods to differentiate between two different regions inside the investigated objects.

WM2021 Conference, 8 - 12 March 2021, Phoenix, Arizona, USA

Several conventional statistical methods are commonly used to evaluate the methods that are used in classifying hazardous materials like uranium inside an investigated object. For example, the automated Receiver Operating Characterisation Curve (ROC) has been used to analyse the performance of the automated binary classifier in detecting the hazard correctly. However, these binary classifications might be falsely misinterpreted, leading to the delivery of information that reports a potential hazard. This automated method can be easily affected by irregularities in the shielding matrix or the body support of the cask. Valuable information can be extracted from a reconstructed three-dimensional (3D) density map of the investigated object. Therefore, a numerical test that can convey important information on how the detector resolutions and choices of several algorithmic methods affect the reconstructed 3D density map should be developed.

To apply the CNR test on the 3D density map outputs, we consider six different regions based on several factors. The factors considered in this study are: 1) presence of a radioactive material, 2) replacing the hazardous material with a non-hazardous material that has almost the same atomic number, 3) fully or partially missing hazardous material, and 4) the location of these materials inside the investigated cask. This method helps convert the qualitative outputs to numerical values that can be used to compare the different algorithms used to produce the 3D output.

First, different muon tomography algorithms will be explained. Then, a Monte Carlo simulation study of the muon scattering method inside a well-shielded V/52 CASTOR cask (see Figure 1) is described. A single high-Z material inside a small cemented nuclear waste drum is imaged to understand the resolutions of the algorithmic methods. A quantitative method is then developed to compare the results obtained from imaging the six regions of interest inside the CASTOR cask in terms of feature resolution and exposure time.

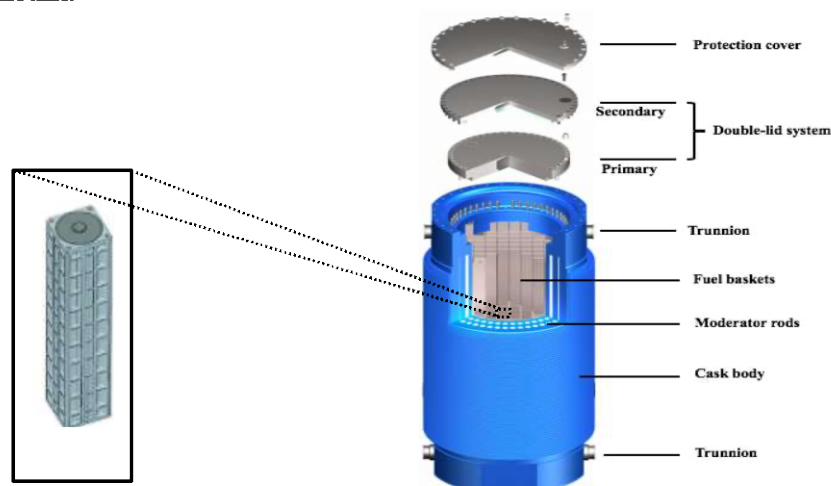


Figure 1. A cutaway view of the V/52 cask accommodating 52 baskets is illustrated on the right hand side. On the left hand side, a schematic illustration of the special quiver designed by GNS to be accommodated inside the baskets [4].

WM2021 Conference, 8 - 12 March 2021, Phoenix, Arizona, USA

IMAGE RECONSTRUCTION ALGORITHM

The simplicity of the Point of Closest Approach (PoCA) algorithm is the reason that it is commonly used in muon tomography as an algorithmic reconstruction imaging method [5]. Therefore, we use PoCA as the first algorithm in our work. The Alternative Angle Statistics Reconstruction (ASR) algorithm has also been considered, especially for large nuclear waste packages [6]. Both methods divide the investigated volume into 3D cubic voxels. The discriminator score is extracted from the muon trajectories that travel through the voxels, in which the density for each voxel is calculated to indicate the final discriminator score. From this score, we can locate the regions that contain dense materials.

The PoCA algorithm assumes that every muon that enters the 3D voxel map (the volume of interest) undergoes a single scattering angle. In theory, the large scattering angle of the muons inside the volume of interest indicates that a high-Z material is present inside the volume. For each voxel, a voxel value is weighted by the average angle for all the muon tracks whose PoCA point is located inside the voxel. The PoCA algorithm is a straightforward method and is considered to be the least complex in terms of computational analysis.

However, the PoCA assumption of a single large scatter is not realistic and leads to the addition of more noise because the muon tracks within the volume of interest might be mistakenly extrapolated. Logically, while muons traverse the investigated area, they are expected to go through many small scatterings that are sometimes interpreted as extreme scattering density inside one voxel.

The ASR algorithm is developed to remove the effects of the PoCA single-scatter approximation. This is achieved by only considering the muon trajectories that enter and exit the volume of interest in the voxels that lie within a chosen minimum distance of these trajectories. Consequently, a noise reduction in the reconstructed density map becomes apparent after cancelling the PoCA assumption.

For each voxel on the map, the projected scattering angles on the X-axis and Y-axis are calculated to obtain a set of scores (S_1 , S_2), see Equations 1 and 2. Then, the final score is assigned to each voxel. We consider several quantiles (ASR [0.50] and ASR [0.25]) of the distributions inside each voxel to determine the final discriminator values that convey information about the object inside the volume of interest.

$$S_1 = (\theta_x p) \quad (\text{Eq.1})$$

$$S_2 = (\theta_y p) \quad (\text{Eq.2})$$

where θ_x is the projected scattering angle on the X-axis, θ_y is the projected scattering angle on the Y-axis and p is the muon momentum.

WM2021 Conference, 8 - 12 March 2021, Phoenix, Arizona, USA

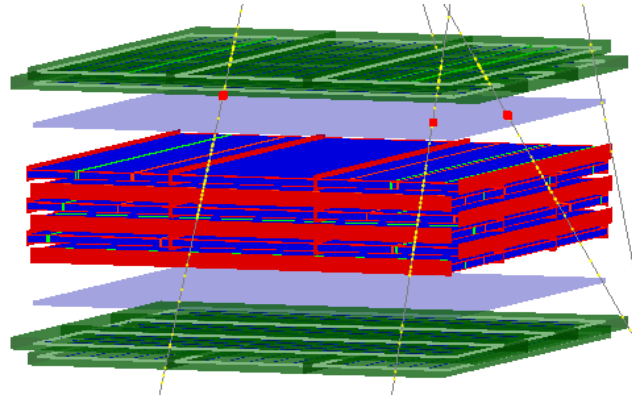


Figure 2. Diagram of one of the identical detector tracking systems placed above and below the volume of interest. The light blue sheets indicate the scintillator panels as they are triggered when muons (the yellow lines) pass through the system. The detectors (RPCs in green and DCs in blue) provide information about the positions where the muon hit the detectors.

BENCHMARKING METHOD

Monte Carlo Simulation Analysis

The algorithmic methods explained in the previous section are applied in the Monte Carlo simulation to investigate the fuel assemblies stored inside the large V/52 CASTOR (see Figure 4). For validation purposes, the 5.5 m-high V/52 CASTOR is simulated by the GEANT4 high-energy particle physics package. It stores 52 baskets accommodating the UO_2 fuel assemblies that come from the Boiling Water Reactors. Its body is made of ductile iron, with an outer diameter of 2.44 m. The box-shaped basket has length, width and height of 13 cm, 13 cm and 448 cm, respectively [4].

The detector system is simulated using GEANT4 and consists of two identical detector systems designed for the CHANCE MT experiment, which is now fully operational at the University of Bristol in a non laboratory environment. The detectors are made from a combination of Drift Chambers (DC) and Resistive Plate Chambers (RPC) with spatial resolutions of ~ 2 mm and ~ 0.3 mm, respectively (see Figure 2). The tracking systems are positioned above and below the volume of interest, with a gap between the two systems of 105 cm for scanning the small drum and of 580 cm for scanning the large CASTOR, if needed. In order to reconstruct the muons' path precisely, each tracking system's 10-layer composites (4 layers of RPC and 6 layers of DC) are arranged in five layers to provide the muon hit positions on the X-Z plane and five layers to give the muon hit positions on the Y-Z plane. The muon passing through the investigated drums are generated by the CRY cosmic ray shower generator library [7].

Before imaging the large CASTOR, the algorithmic methods explained are tested by reconstructing an image of a 10 cm^3 single cube of tungsten embedded in the centre of a small concrete-matrix drum with diameter and length of 57 cm and 88 cm, respectively. The muon tracks are summed using the PoCA and the ASR algorithms discussed in the previous section to reconstruct a 3D density map of the tungsten cube inside the nuclear waste drum and finally projected to the 2D projection plot (see Figure 3).

WM2021 Conference, 8 - 12 March 2021, Phoenix, Arizona, USA

Both methods achieve a good discrimination level of the tungsten cube from the background in 25 days' exposure time. Furthermore, the ASR output shows much less noise than the PoCA result due to the fact that ASR avoids accounting for the outlier events with extreme scattering by assigning the weight to multiple voxels. The next two sections will present the feasibility of using these methods to image the fuel assemblies inside the higher-shielding cask (V/52 CASTOR) in terms of target type and exposure timing.

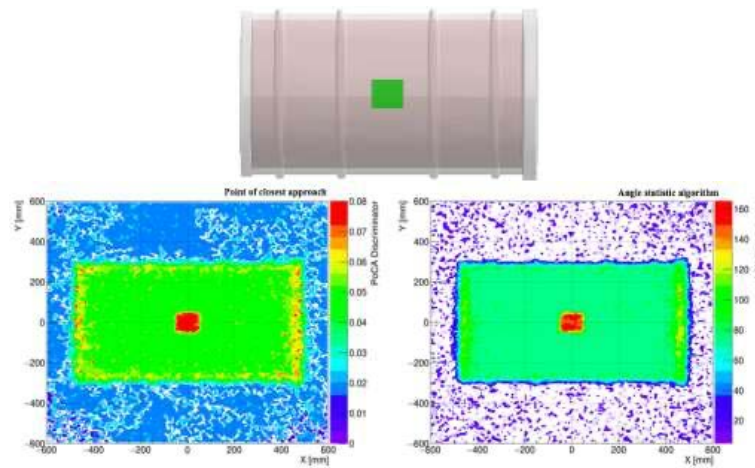


Figure 3. A 10 cm³ tungsten cube positioned in the centre of a simulated cement matrix nuclear waste drum (top). The 2D projection output of the tungsten cube inside the small drum in PoCA (bottom left). The output of ASR for the same tungsten cube (bottom right).

Feature and Size Resolutions

In order to compare the performance of the algorithmic methods in imaging the fuel assemblies inside the CASTOR cask, simple tests are used to compare the different regions inside the CASTOR quantitatively. The feature resolution test is used to examine the ability of the algorithms to distinguish the contents of each basket individually and separate these from those of the neighbouring baskets. A chosen number of baskets have been filled up to 50% of their normal capacity and located randomly throughout the CASTOR to test the size resolution. A CNR method is developed and applied to the regions containing different baskets accommodating the fuel assemblies:

- A fully loaded basket.
- A half-loaded basket (the central UO₂ pellets inside the basket are removed on purpose).
- A half-loaded basket (the UO₂ pellets to the side of the basket are removed on purpose).
- A lead basket (the UO₂ pellets are replaced with Pb pellets for testing purposes).
- An empty basket.

The CNR method is used to assess the ability of each algorithm to differentiate between the two regions of interest, e.g., the region containing the fully loaded basket and the region containing the empty basket.

WM2021 Conference, 8 - 12 March 2021, Phoenix, Arizona, USA

This method reveals which algorithm can locate either fully missed or partially missed of the fuel assemblies stored inside the CASTOR. The method that produces a higher value of CNR is more capable of detecting the irregularity of the fuel assembly situations.

The CNR is defined as the difference in the signal contributions between different regions inside the reconstructed image divided by the standard deviations of the two signals:

$$CNR = \frac{|\mu_1 - \mu_2|}{\sqrt{\sigma_1^2 + \sigma_2^2}} \quad (\text{Eq.3})$$

where μ_1 is the mean of region 1's signal and μ_2 is the mean of region 2's signal. Meanwhile, σ_1 and σ_2 are the standard deviations of the signal in region 1 and region 2, respectively.

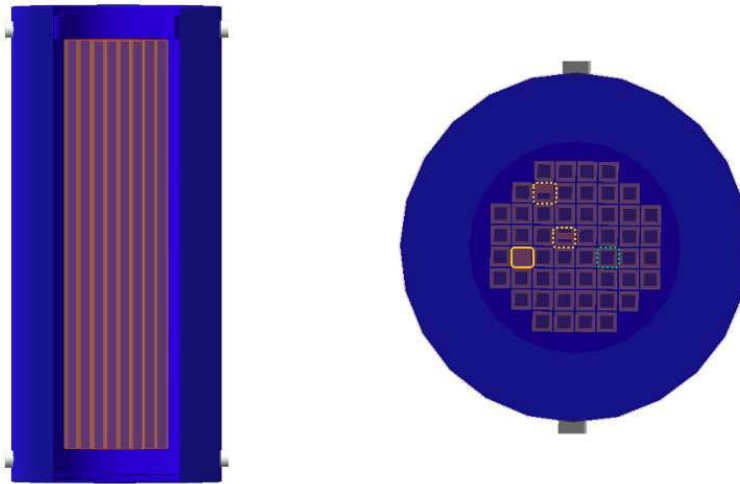


Figure 4. The top and the side views of the simulated V/52 CASTOR accommodating 52 baskets. The yellow-dashed lines represents the half-loaded baskets and the green-dashed line represents the baskets that accommodate Pb pellets and the yellow-solid line represents the empty basket.

WM2021 Conference, 8 - 12 March 2021, Phoenix, Arizona, USA

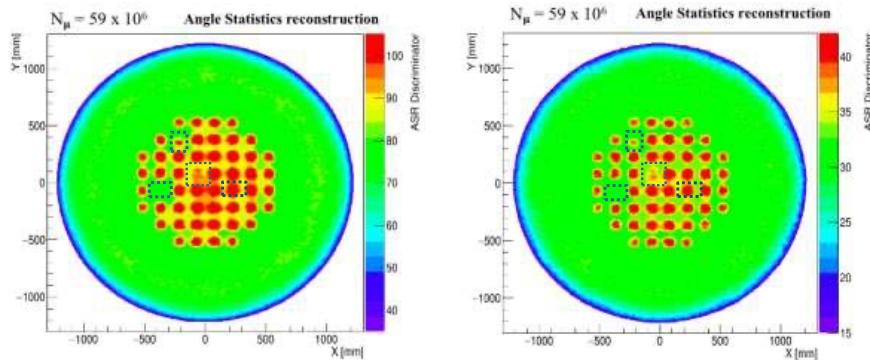


Figure 5. The left is the ASR output of the fuel assembly feature resolution when 50% of the ASR distribution in each voxel is considered. The right figure shows the result of accounting for only 25% of the ASR distribution in each voxel.

Figure 5 indicates a reconstructed X-Z slice through the 3D density map of the fuel assemblies using the ASR algorithm with 50% and 25% quantiles of the ASR distributions in each voxel. The output of the ASR algorithm in general can distinguish and locate the empty basket with CNR values of 19 and 15 for ASR [0.50] and ASR [0.25], respectively, if we compare the empty basket region with the fully loaded one.

This ASR method achieves clarity in the image reconstructed as it prevents outsider events with large scattering angles from being integrated into the voxel’s weighting. Notably, the negative consequence of using this method is that it affects the shape of the object that was reconstructed. Specifically, the edges of the cask will be stretched abnormally because the detector acceptance on the edges of the detector prefers high-scatter tracks, resulting in the voxels being filled and stretching at the cask’s edges.

The PoCA algorithm fails to locate the empty basket with a CNR value of 1.03 due to a smearing caused by the scattering vertices that are reconstructed outside the target. This smearing occurs because the muon experiences additional scatters when it leaves the target. Therefore, the fuel assemblies extend and merge with their neighbours’ baskets. Both methods could not differentiate between the two regions of the fully loaded UO₂ basket and the basket with Pb pellets, which, in theory, is expected as they have almost the same density. i.e., 10.97 g/cm³ and 11.34 g/cm³ for UO₂ and Pb, respectively.

In terms of size resolution, the ability of the ASR [0.25] method to locate and distinguish the missing half of the fuel assemblies inside the two baskets located in the centre and the sides of the cask is clearly shown in Figure 4. Comparing a half-loaded basket (centre fuel assemblies removed) with a fully loaded basket, the CNR values are decreased to 4.0 and 3.0 when ASR [0.50] and ASR[0.25] are used to reconstruct the two regions, respectively. Meanwhile, comparing the half-loaded basket (side fuel assemblies removed) with a fully loaded UO₂ basket shows a 12.5% increase in CNR value at 4.5 when ASR [0.50] is used to reconstruct the two regions. While, the CNR value remains the same when ASR[0.25] is used.

WM2021 Conference, 8 - 12 March 2021, Phoenix, Arizona, USA

Exposure Time Reliance

The CNR method used in the previous section helps in understanding the performance of the detector system and the algorithmic method on imaging the fuel assemblies inside the V/52 cask shielded by ductile iron. However, other factors might have influenced the feature resolution of the 3D density map of the cask content, for instance, the exposure time or the number of muons that passed through the cask. A number of cosmic muon simulations are considered to understand the effects of the exposure time on the quality of the reconstructed images of the fuel assemblies. Figure 5 shows the output density maps produced by the ASR [0.25] discriminator for an exposure time that started from 45 days and was reduced to 30 days, 15 days, and then to only 6 days. There is no significant difference between the outputs of 45, 30 and 15 days in terms of the feature and size resolutions. However, the feature resolutions decline when the time is shortened to 6 days, at which time the reconstructed assemblies start to smear to the surrounding ones, making it difficult to see the half-loaded baskets. There are no noticeable changes in the ability of the system to locate the empty baskets even when the exposure time is as short as 6 days.

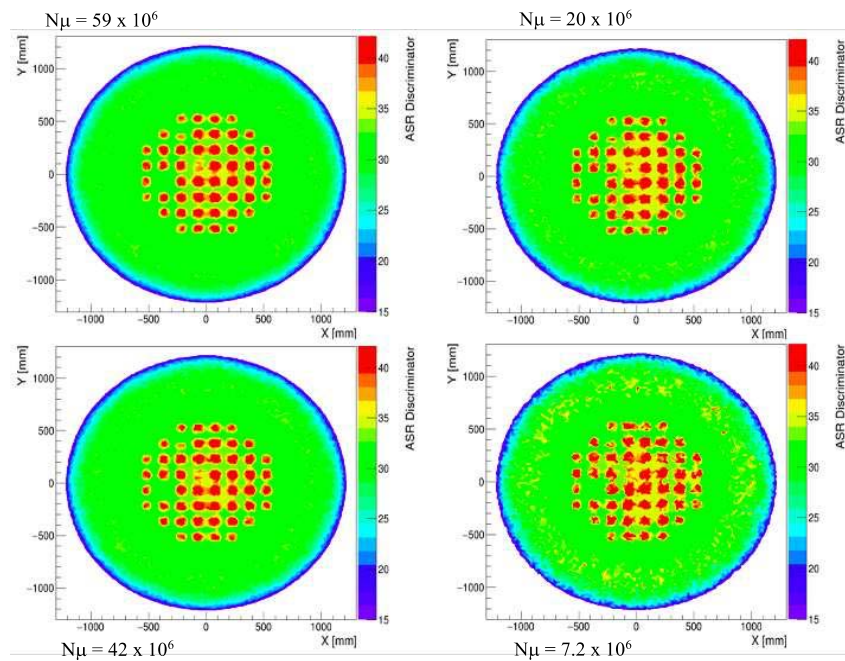


Figure 6. The X-Z slices of the reconstructed image of the V/52 CASTOR using ASR[0.25] in 45 days' exposure time (top left), 30 days' exposure time (bottom left), 15 days' exposure time (top right) and 6 days' exposure time (bottom right).

WM2021 Conference, 8 - 12 March 2021, Phoenix, Arizona, USA

CONCLUSION

A method has been developed to understand the performance of the MT detector system and the algorithmic methods used to differentiate between two specific regions inside the reconstructed density map of the investigated CASTOR cask. Comparing the regions within the reconstructed image can provide information about the limitation of the system and the method that reconstructs the image.

The CNR test is used to examine the capability of the system in detecting any irregularities within the fuel assemblies, such as fully missing or partially missing UO₂ pellets. The results in terms of feature and size resolution of the reconstructed density map indicate that the commonly used PoCA algorithm has failed to detect the missing fuel assemblies inside the empty basket, as the CNR value is almost equal to the CNR value of the fully loaded basket. Notably, the ASR method can impressively locate both the empty basket and the half-loaded basket and distinguish them from the fully loaded baskets with CNR values of 19 and 4.5 when considering 50% of the ASR discriminator distributions inside each voxel. This method is capable of detecting the fully missing basket within a short time of six days' exposure.

REFERENCES

- [1] CHANCE 2020 : <http://chance-h2020.eu>
- [2] Ricard, D., Plumeri, S., Boucher, L., Rizzo, A., Tietze-Jaensch, H., Mathonat, C., Bruggeman, C., Velthuis, J., Thompson, L., Genoud, G., Bucur, C., Kikola, D., Zakrzewska-Koltuniewicz, G. (2018). The CHANCE project "Characterization of conditioned nuclear waste for its safe disposal in Europe". *DEM 2018 - Dismantling Challenges: Industrial Reality, Prospects and Feedback Experience, France, Avignon – 2018, October 22 – 24*
- [3] Thomay, C., Velthuis, J. J., Baesso, P., Cussans, D., Morris, P. A. W., Steer, C., ... & Stapleton, M. (2013). A binned clustering algorithm to detect high-Z material using cosmic muons. *Journal of Instrumentation*, 8(10), P10013.
- [4] CASTOR® V/52 - GNS", *Gns.de*, 2020: <https://www.gns.de/language=en/21553/castor-v-52>.
- [5] Jonkmans, G., Anghel, V. N. P., Jewett, C., & Thompson, M. (2013). Nuclear waste imaging and spent fuel verification by muon tomography. *Annals of Nuclear Energy*, 53, 267-273.
- [6] Stapleton, M., Burns, J., Quillin, S., & Steer, C. (2014). Angle Statistics Reconstruction: a robust reconstruction algorithm for Muon Scattering Tomography. *Journal of Instrumentation*, 9(11), P11019.
- [7] C. Hagmann, D. Lange and D. Wright, "Cosmic-ray shower generator (CRY) for Monte Carlo transport codes," 2007 IEEE Nuclear Science Symposium Conference Record, Honolulu, HI, 2007, pp. 1143-1146, doi: 10.1109/NSSMIC.2007.4437209.

WM2021 Conference, 8 - 12 March 2021, Phoenix, Arizona, USA

ACKNOWLEDGEMENT

This study is funded jointly by the European NFRP7 programme under Grant No. 755371 (CHANCE project) and the UK STFC NuSec Network.



9.4 A Robust Method to Find Gas Bubbles

WM2021 Conference, March 8 - 12, 2021, Phoenix, Arizona, USA

A Robust Method to Find Gas Bubbles Inside Large Nuclear Waste Containers Using Muon Tomography– 21151

M. Mhaidra* & **, A. Kopp**, A. Alrheli***, C. de Sio**, D. Barker***, P. Stowell***,
M. Weekes***, M. Dobrowolska**, D. Kikoła*, L. Thompson**, J. Velthuis*** & ****

* Warsaw University of Technology, Poland

** School of Physics, University of Bristol, UK

*** Department of Physics and Astronomy, University of Sheffield, UK

**** School of Nuclear Science and Technology, University of South China, PRC

ABSTRACT

Radioactive waste has been stored for many years in drums with both concrete and bitumen matrices. The continuous radiation leads to production of radiolysis gases, mostly Hydrogen. The presence of Hydrogen gas inside the bituminized containers can present serious safety issues. Muon Tomography has been shown to have a huge potential to play an essential role in the characterization of nuclear waste. In this paper we present a robust method to successfully detect and localize hydrogen bubbles as small as 4.42L starting from 6 days muon exposure in different shapes and different matrices. We also show that the volume reconstruction for the smallest bubbles considered in our studies is better for concrete matrix with a density of 2.3 g/cm³.

INTRODUCTION

Radioactive waste generated from nuclear power plants is later solidified in concrete or bitumen. For many years, the bitumen containers have been extensively used for storage of nuclear waste. In several countries, nuclear waste was stored either in pure bitumen or a mixture of pure bitumen and radioactive salts. In homogeneous bituminized waste such as the Belgian Eurobitum, the mixture consists of ~ 60 wt% of pure bitumen Mexphalt R85/40 and ~ 40 wt% of radioactive salts and metal (hydro)oxides, of which NaNO₃ (20 - 30 wt%) and CaSO₄ (4 - 6 wt%) are the most important ones [1, 2]. However, in the other hand, the solidified radioactive liquid concentrates like the one from COGEMA La Hague plant in France (called STE3) consist of a pure bitumen Viatotal 70/100 mixed with NaNO₃ (28 wt%), Na₂SO₄ (5 wt%), CoS (10 wt%), BaSO₄ (46 wt%) and PPFNi (9 wt%) [3].

In presence of continuous α , β and γ irradiation, the high Z materials such as Uranium and other metals present in nuclear waste can oxidize, producing bubbles of mostly hydrogen gas. The produced hydrogen can dissolve in the bitumen matrix or form small gas bubbles that tend with time to accumulate into large bubbles and move upwards because of the lower density. It has already been observed in experiments [6, 7] that when oxidized bitumen Mexphalt R85/40 is gamma irradiated, the radiolytic gases cause mechanical tension resulting in pore formation or cracks and easier gas release.

Similar experiments [5, 8, 9, 10] confirm higher swelling of pure bitumen and bituminized waste products (BWP) with increasing γ irradiation dose.

The swelling caused by this process of hydrogen generation can present important safety issues during interim storage. Since small H₂ bubbles can dissolve in the bituminized waste drum and agglomerate to large bubbles, it is important to detect bubbles as small as possible. For this reason, it is of high importance to have a better knowledge of the volume and size of hydrogen gas bubbles, as well as their position and migration in the nuclear waste drum. In this paper we present a robust method to find the gas bubbles in the nuclear waste containers. The method uses Muon Tomography to measure the volume of the gas bubbles as well as the shape and location. We have previously shown that it was possible to reconstruct bubbles of a total gas volume of 2 L or more with a resolution of $1.55 \pm 0.77\%$ in 16 days of data taking [11]. In this work apply our improved method was applied to bituminized waste and we demonstrated that it is capable to detect and localize hydrogen bubbles as small as 4.42 L starting from 6 days muon exposure in different shapes and different bituminized waste drums. The results of our method

WM2021 Conference, March 8 - 12, 2021, Phoenix, Arizona, USA

of bubble detection in nuclear waste drums demonstrated that Muon Tomography is a very suitable technique to address the problem of hydrogen accumulation in a variety of waste drums.

Muon tomography

Muon tomography (MT) is a technique that uses secondary cosmic radiation to scan volumes from a safe distance [12]. MT has been successfully applied in many fields, such as archaeology, geosciences, civil engineering, security, and nuclear safety [13]. In comparison with other scanning techniques e.g. gamma rays or X-rays, MT uses highly penetrating particles, does not rely on any radiation source, and has a flux of around 10000/(m² minute). As muons are charged particles, they undergo multiple Coulomb scattering while traversing matter.

As can be seen from Eqs. 1 and 2 the width of the projected scattering angle distribution varies with Z. This is the mean idea behind MT, which has been exploited since 2003 [12] for applications where a difference between a high-Z material and a lower-Z background can be seen (e.g., special nuclear materials (SNM) hidden in shipping containers, or high-Z materials within bitumen or concrete matrices).

The distribution of the scattering angle can be estimated as a Gaussian distribution with a mean of zero [14] and standard deviation σ_μ as:

$$\sigma_\mu = \frac{13.6 \text{ MeV}}{\beta \cdot c \cdot p} \sqrt{\frac{x}{X_0}} \left[1 + 0.038 \cdot \ln \frac{x}{X_0 \cdot \beta} \right], \quad (\text{Eq. 1})$$

where p is the muon momentum, β is muon's speed divided by the speed of light c , x is the path length from entry to exit and X_0 is the radiation length. X_0 can be approximated with good precision as [15]

$$\frac{1}{X_0} \approx \frac{Z(Z+1)}{A} \cdot \ln\left(\frac{287}{\sqrt{Z}}\right), \quad (\text{Eq. 2})$$

where A is mass number, and Z is the atomic number.

To perform MT it is enough to place multiple detectors above and below the volume to be scanned and reconstruct the incoming and outgoing muons trajectories. When these two trajectories meet, a scattering vertex can be reconstructed. This vertex is not a physical location, but it is a very useful assumption.

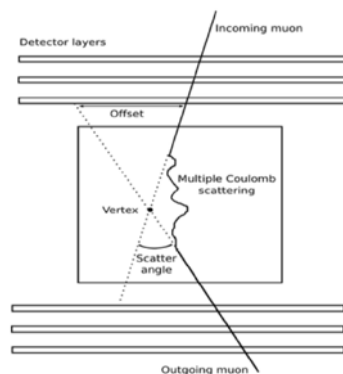


Figure 1. Illustration of muon's trajectory measured before and after traversing the volume of interest and the reconstructed scattering vertex [11].

WM2021 Conference, March 8 - 12, 2021, Phoenix, Arizona, USA

Since the exact trajectories of the muons inside the scanned volume are unknown, many estimation algorithms have been applied to measurements, which include the most likely path (MLP) [18], Straight line path (SLP) and point of closet approach (PoCA) [17].

After the trajectory estimation, MT results are usually presented in a three dimensional voxelized map where each voxel contains information about the scanned material properties.

The materials properties are estimated from the variance of the scattering angles in each voxel. To calculate the scattering densities in each voxel, various algorithms have been proposed [17, 19]. In this paper, the binned clustering (BC) algorithm is used [20], and it has been used already for multiple studies to discriminate between high-Z [21, 22] and low-Z materials [11].

Binned clustering algorithm

In this study, the binned clustering (BC) algorithm is used to discriminate low-Z materials from the high-Z materials and the matrix background. The main idea behind the algorithm is to divide the scanned volume into many voxels with 10 mm sides and select only the most scattered tracks in each voxel. The default minimum value of scattered tracks in each voxel was chosen to be 5. The algorithm is based on the fact that there is a large density of high angle scatters in high-Z materials, thus the distance between two reconstructed vertices, divided by their scatter angle, will be smaller. For each voxel with at least N reconstructed vertices, a weighted metric distance m_{ij} is calculated as

$$m_{ij} = \frac{\|v_i - v_j\|}{(\theta_i)(\theta_j)}, \quad (\text{Eq. 3})$$

Where v_i is the reconstructed vertex position of the muon i and its scatter angle θ_i . In low-Z materials, there are less high angle scattering events than in high-Z materials. As a result, for the lowest Z materials inside the scanned volume, the highest median of metric (discriminator) values are found.

It has been shown already that the mean value of the discriminator distribution has a monotonic dependence on the volume of the low-Z materials inside a nuclear waste drum [11].

In this study, we will use the mean value of the discriminator distribution μ_d to find the total H_2 gas volume in different backgrounds. Then the discriminator difference between a voxel with gas inside and one filled with bitumen can be used to localize the gas bubbles.

METHODS

The study presented here is based on simulation. Simulations of the MT detector system of the CHANCE project [24] were performed using Geant4 [25], which is a toolkit developed to simulate the particle passage through matter. The Geant4 version used was 10.5, including physics process like ionization, Bremsstrahlung, muon process of multiple scattering and pair production. The cosmic muons were generated using the CRY library [26], by simulating primary protons with energies between 1 GeV and 100 TeV, and creating showers of secondary particles.

The particle distributions depend on the altitude. Sea level was chosen from the three available altitudes in CRY. The particle distributions also depend on the effect of the magnetic at different latitudes, so the latitude of 52.22° was chosen, corresponding to the coordinate of the Physics department at Warsaw University of Technology. In the analysis presented here, all simulations were 28 days' worth of muon exposure. It was chosen to simulate three types of filled drums, a concrete filled drum with a density of 2.3 g/cm³, a Eurobitum bitumen filled drum with a density of 1.35 g/cm³, and finally a STE3 bitumen filled drum with a density of 1.41 g/cm³. Different sizes and shapes of H₂ bubbles were simulated, with a density of 1.2 · 10⁻³ g/cm³.

WM2021 Conference, March 8 - 12, 2021, Phoenix, Arizona, USA

A large, mobile MT detector shown in Fig. 2 (a) has been recently built in a non-laboratory environment in Bristol, UK [27]. It is rain protected but neither humidity nor temperature controlled; hence the environmental conditions are likely similar to the ones in the real field deployment.

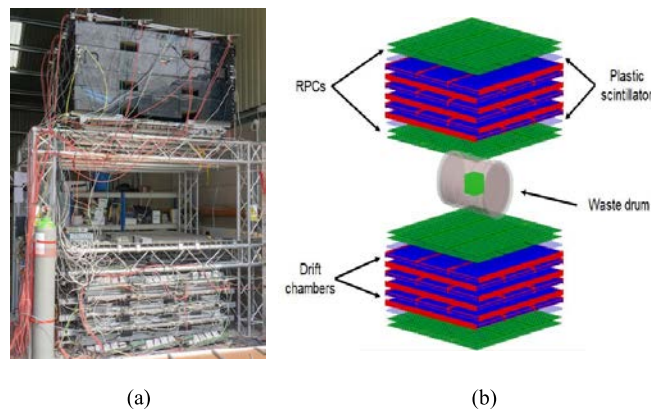


Figure 2. (a) The muon scattering tomography detector system of the CHANCE project. Shown are the detector systems above and below the empty sample space consisting of three layers of drift chambers and two RPC layers. The top stack additionally contains two layers of plastic scintillators used as triggers. The detectors cover an area of approximately $1.8 \times 1.8 \text{ m}^2$. (b) Visualization of the CHANCE detector system using a GEANT4 simulation framework. (Online version in color.)

MT requires the reconstruction of the incoming and the outgoing muon trajectories; hence the detectors need to be placed below and above the scanned volume.

The MT system is a combination of both Resistive Plate Chambers (RPC) and drift chambers, connected to a set of scintillator trigger paddles. The scintillator paddles are used as a trigger to start the readout process. The RPCs were designed and built at the University of Bristol [28], and currently are run on CO_2 gas. Each RPC layer is a combination of three large $60 \times 180 \text{ cm}$ area detector providing a hit position in one dimension with a resolution of approximately $350 \mu\text{m}$. The next layer is 90° rotated around the Z-axis to reconstruct three-dimensional hit positions at the upper and lower part of the detector as shown in Fig. 2 (b). In a similar way, three layers of drift chambers are arranged in along the X-axis while another three are arranged along the Y-axis. The total six layers provide muon hit positions with resolution of approximately 2 mm . The combination of the information about the muon hits from both the drift chambers and RPCs provide an excellent tracking and measurement of the scattering angles with high precision. The full MT detector is now operational, the first test data have been taken, and mystery drums provided by SCK•CEN are being scanned.

RESULTS

To evaluate the MT system ability to find the position of H_2 bubbles, as well as their volume, a robust algorithm was developed. In the next sections, a set of tests were developed that will show the effectiveness of the proposed method to reconstruct the total amount of gas inside different types and sizes of nuclear waste drum.

WM2021 Conference, March 8 - 12, 2021, Phoenix, Arizona, USA

Reconstruction of the H₂ gas volume in large nuclear waste drums

To evaluate the effectiveness of method to measure the H₂ gas volume inside a nuclear waste drum, many simulations were performed, introducing several H₂ bubbles sizes inside different container types. In each simulation, the bubbles were cylindrical with a length varying from 5 cm to 36 cm, a radius varying from 2 cm to 12 cm and they were aligned with the drum central axis. The simulated drums have a 2.5 cm thick steel wall, an external diameter of 61.5 cm and a height of 88 cm. For each drum type, the mean of the BC discriminator (μ_d) for each bubble size was extracted and then plotted against the correspondent H₂ gas volume. As shown in Fig. 3, for all three set of simulated drums, the μ_d displays a monotonic dependence on the H₂ gas volume. Our additional studies show that this linear behaviour holds for other shapes and location of the bubbles. This monotonic dependence was fitted with a straight line. The results are

$$\mu_d (\text{Concrete}) = (3.277 \pm 0.090) \times 10^{-3}V + (8.587 \pm 0.759 \times 10^{-3}). \quad (\text{Eq.4})$$

$$\mu_d (\text{Eurobitum}) = (1.639 \pm 0.080) \times 10^{-3}V + (8.827 \pm 1.041 \times 10^{-3}). \quad (\text{Eq.5})$$

$$\mu_d (\text{STE3}) = (1.654 \pm 0.089) \times 10^{-3}V + (8.816 \pm 0.970 \times 10^{-3}). \quad (\text{Eq.6})$$

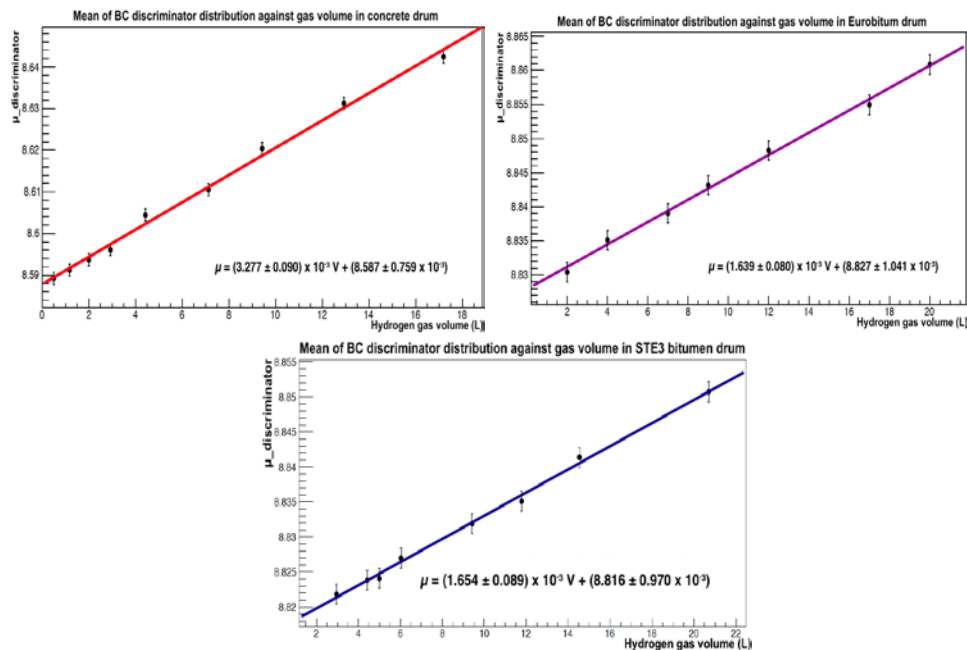


Figure 3. The H₂ volume values against the corresponding μ_d value with linear regression fits for a Concrete filled drum (top left) and a Eurobitum filled drum (top right) and a STE3 bitumen filled drum (bottom). The simulated bubbles are cylindrical and aligned with the central axis of the drum.

WM2021 Conference, March 8 - 12, 2021, Phoenix, Arizona, USA

To evaluate the accuracy of the method, for each of the drums new simulations were made with new bubbles volumes. The μ_d was extracted and then using the fit results from Fig. 3, the total volumes were reconstructed. The reconstructed H_2 volumes are plotted as a function of the true volumes, see in Fig. 4.

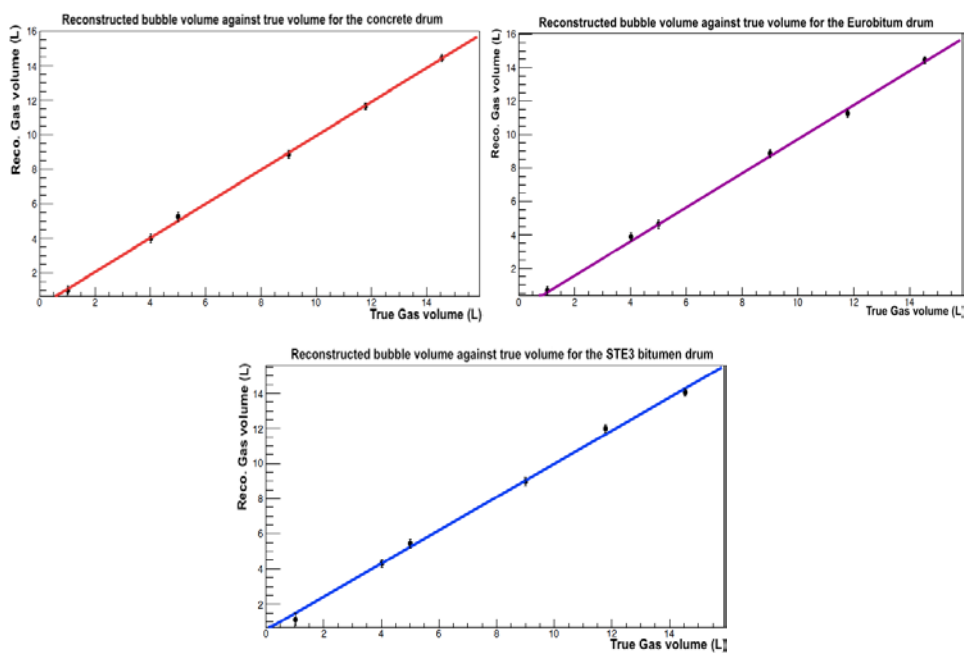


Figure 4. The true H_2 volume values against the reconstructed H_2 volume for a Concrete filled drum (top left) and a Eurobitum filled drum (top right) and a STE3 bitumen filled drum (bottom). The simulated bubbles are cylindrical and aligned with the central axis of the drum.

Fig. 5 shows the relative uncertainty on the reconstructed H_2 volume as a function of the true volumes for concrete filled drum, Eurobitum filled drum and STE3 bitumen filled drum respectively.

WM2021 Conference, March 8 - 12, 2021, Phoenix, Arizona, USA

It can be seen that for bubbles larger than 2L the relative uncertainty on the H_2 volume was below 10%. This increases rapidly for smaller bubbles. This shows that it is possible to successfully reconstruct even a small gas volume and with a good resolution, and for small bubbles the accuracy for volume reconstruction of the smallest gas bubble (about 1 L) is better for matrix with higher density.

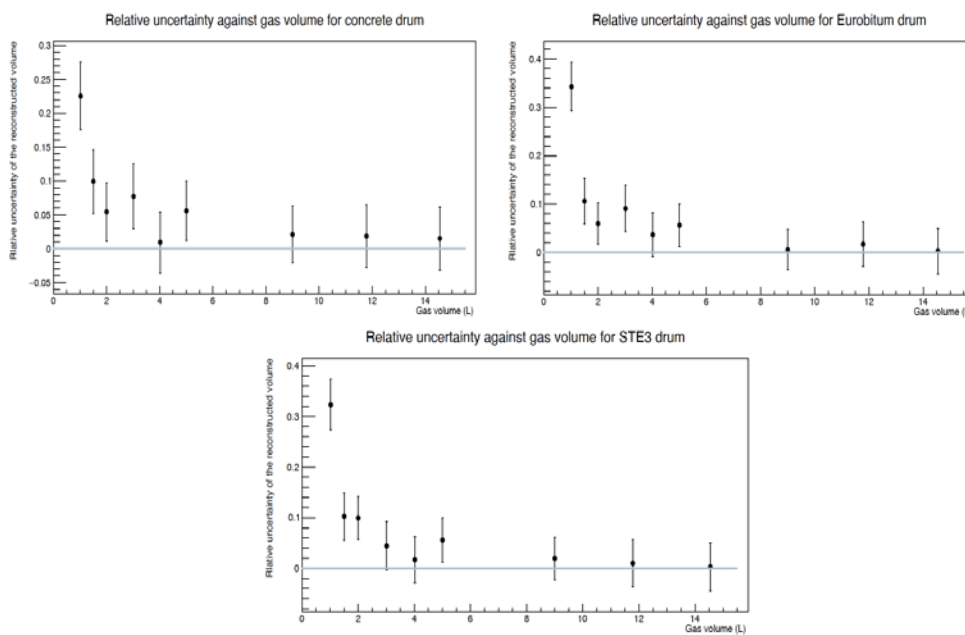


Figure 5. The relative uncertainty on the reconstructed H_2 bubble volumes against the true H_2 gas volume for a concrete filled drum (top left) and Eurobitum filled drum (top right) and a STE3 bitumen filled drum(bottom). The simulated bubbles are cylindrical and aligned with the central axis of the drum.

In the three sets of simulations, the measurement of the total H_2 gas volume was performed for cylindrical bubbles only. However, it is crucial to check if the results are dependent on the shape of the bubbles and their location inside the nuclear waste drum. To study this, simulations using varying numbers of spherical bubbles randomly distributed inside an Eurobitum drum were performed.

WM2021 Conference, March 8 - 12, 2021, Phoenix, Arizona, USA

Table 1 shows the geometries used and the results of the study. In each simulation the μ_d was extracted and then using the fit for the Eurobitum bitumen filled drums, the total gas volumes were successfully reconstructed within their uncertainties. This study provides a strong evidence that the method does not depend on the shape of the bubbles or their locations inside the nuclear waste drum.

Eurobitum drum filled with H ₂ Bubbles	Real gas volume	Reconstructed gas volume
	4.42L	4.19 ± 0.52L
	12.39L	12.20 ± 0.35L
	3.13L	3.90 ± 0.48L
	3L	3.40 ± 0.36L
	1.5L	1.23 ± 0.38L
	0.66L	0.91 ± 0.35L

Table 1. Real and reconstructed gas volume for Eurobitum drum filled with H₂ bubbles. (Online version in color.)

Since the slope of μ_d as function of H₂ gas volume changes between concrete and bitumen waste drums, we performed an additional study to see how the slope parameter varies with density of the matrix. Fig. 6 shows the slope of fitted line plotted as a function of density of bitumen drum. Each set of simulated bitumen drums was filled with cylindrical H₂ bubbles and aligned with the central axis of the drums.

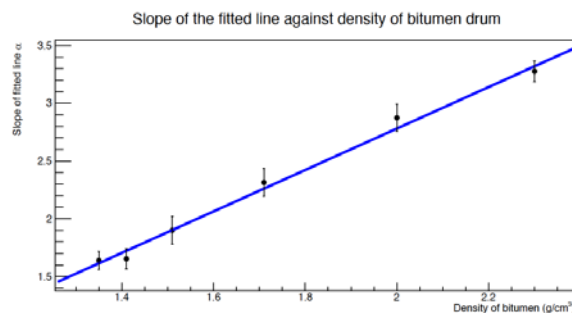


Figure 6. Slope of fitted line plotted against density of a bitumen drum. Each point corresponds to 8 simulations of 28 days moon exposure of a bitumen drum filled with hydrogen bubbles inside.

WM2021 Conference, March 8 - 12, 2021, Phoenix, Arizona, USA

The H_2 bubbles have a length varying from 5 cm to 36 cm, a radius varying from 2 cm to 12 cm. It can be seen that the slope value of the fit equation has a monotonic dependence on the density of the matrix. This result has two important implications. Firstly, the volume reconstruction method can be in principle used for other matrix densities without time-consuming calibration studies as the slope can be obtained from the fit in Fig. 6. Second, the accuracy of our method increases with increasing matrix density since the relative accuracy of reconstruction of small H_2 bubbles is better for higher slope values.

All the simulations in the three sets of drums were performed using one size of nuclear waste drum. In order to determine if the size of the drum would influence the method, two other sets of simulated drums were used. Each time the size of the drum was reduced by around 20% of the previous one. The volume of the included gas bubbles was reconstructed using the fit result for the original size drum. Fig. 7 shows that the relative uncertainty in the reconstructed gas volume does not depend on the drum size. The relative uncertainty on the reconstructed bubbles is less than 10% for the three sizes. This shows the robustness of the method and its applicability to real nuclear waste drums of different sizes.

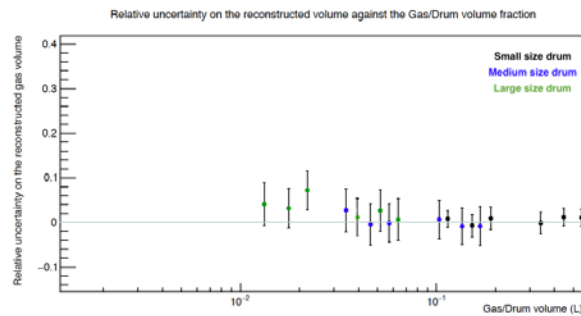


Figure 7. The relative uncertainty on the reconstructed bubble volumes as a function of the gas/drum volume for a medium, small and large size drum. (Online version in color.)

Localization of the H_2 gas bubbles using the difference of μ_d

In the previous sections, it was shown that the total H_2 gas volume in a nuclear waste container can be measured with high precision, independently of the shape and location of the bubbles, and in different sizes and types of nuclear waste containers. For the risk assessment of each nuclear waste container, it is useful to have a good knowledge of the location of the H_2 bubble and its migration inside the container. To reveal the location of the H_2 bubbles, we compare a drum of interest with a reference one, filled with matrix only (the background container). Then the mean of the BC discriminator in the containers with bubbles subtracted from the mean of the discriminator in background containers only ($\Delta \mu_d$), was plotted against the H_2 volume and then fitted with a straight line. The simulations performed for this study used cylindrical bubbles.

WM2021 Conference, March 8 - 12, 2021, Phoenix, Arizona, USA

Fig. 8 shows that $\Delta \mu_d$ is linearly dependent on the H_2 gas volume, hence it is sensitive to a presence of bubbles inside the nuclear waste drums.

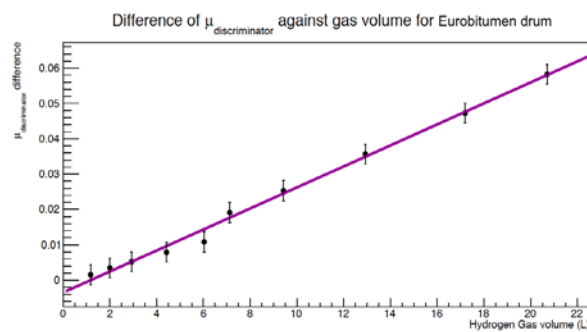


Figure 8. The H_2 volume values against the corresponding $\Delta \mu_d$ value with a linear regression fit for Eurobitumen filled drum.

To localize gas bubbles, we first divide the drum into slices along the x direction. For each slice we calculated μ_d for drum of interest and the background drum. Then we obtained $\Delta \mu_d$ for each of the slice and divide it by its uncertainty to show discrimination power of this method.

The Fig. 9 shows a scanned Eurobitumen bitumen filled drum with 4.42 L H_2 bubbles inside, divided into slices along the X axis. Each slice was 2 cm wide. Since the $\Delta \mu_d / Error$ is around 1 outside the H_2 bubble region, which is consistent with statistical fluctuations. The $\Delta \mu_d / Error$ shows a signal at a level of $\Delta \mu_d \sim 2-4$ in the range where the gas bubble is expected.

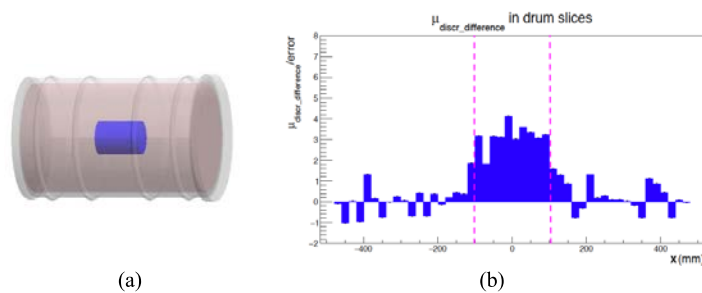


Figure 9. (a) Sketch of a simulated Eurobitumen drum filled with 4.42L cylindrical H_2 bubble. (b) $\Delta \mu_d$ divided by the error in each slice, between 4.42L H_2 bubble and a Eurobitumen filled drum along the X axis. The dashed lines indicate the true bubble position. (Online version in color.)

WM2021 Conference, March 8 - 12, 2021, Phoenix, Arizona, USA

This provides an evidence that the method is sensitive to the bubble location. For further studies of the minimal time needed to detect a bubble a threshold value of $\Delta \mu_d > 3$ was chosen.

The shown results allow to determine the total volume of H_2 gas bubbles inside nuclear waste containers, by calculating the $\Delta \mu_d$ in drum slices and find where the H_2 bubbles are localized.

Time needed to detect H_2 gas bubbles

To determine the amount of time needed to find H_2 gas bubbles inside a scanned nuclear waste container, the $\Delta \mu_d / Error$ was calculated in the simulated STE3 bitumen filled drum with a 4.42 L cylindrical bubble inside, and then plotted against the scanning time.

A STE3 bitumen filled drum with 4.42L bubble and two STE3 bitumen filled drums were simulated for 3 to 30 days. In each set of simulations, a cut on the minimum number of tracks in each voxel was chosen, from a default cut equal 5 to high cut equal 40. With a default minimum number of tracks equal 5, most of the scattering tracks in each voxel are included.

In the Fig.10, the $\Delta \mu_d / Error$ as a function of scanning time is shown. The STE3 bitumen only (background) is fluctuating at level of $\Delta \mu_d / Error \sim 1$.

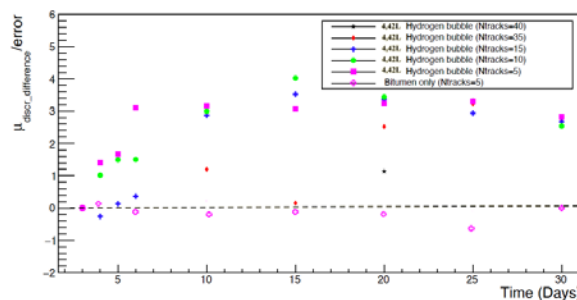


Figure 10. $\Delta \mu_d / Error$ for Eurobitum filled drum with a 4.42L H_2 gas bubble and a STE3 bitumen filled drum for different exposure times and different cuts on the minimum number of tracks (Ntracks) in each voxel. (Online version in color.)

If a threshold value to detect a H_2 gas bubbles of 3 is chosen, then for a low minimum number of tracks equal to 5, it takes around 6 days to detect a 4.42L H_2 bubble. For longer scanning times the ratio of the $\Delta \mu_d / Error$ will remain approximately constant, as the difference measurement itself does not improve anymore. Scanning times less than 6 days do not give enough data to detect the H_2 bubble. However, we are investigating techniques to exclude the presence of bubbles with less data taking time.

CONCLUSIONS

The presence of H_2 gas bubbles inside nuclear waste containers can present a serious safety issues during interim storage. MT is a non-destructive technology which can scan the contents of nuclear waste drums from a safe distance and without introducing any additional radiation. In this paper it has been shown, through the CHANCE MT simulations, that it is possible to reconstruct precisely H_2 bubbles volume in different shapes and location inside different size bitumen and concrete filled nuclear waste drums and

WM2021 Conference, March 8 - 12, 2021, Phoenix, Arizona, USA

determine H₂ bubbles location using our analysis method. For bubbles larger than 2L the relative uncertainty on the H₂ volume was below 10%. This increases rapidly for smaller bubbles.

In general, the method works well for both bituminized and concrete drums, but we found that the accuracy of volume reconstruction for the smallest bubbles considered in our studies is better for higher density matrices. The muon exposure time needed to detect a 4.42 L bubble was found to be about 6 days.

The CHANCE MT detector has been already built in a non-laboratory environment in Bristol, UK, the first data has been taken, and a blind test with drums from SCK•CEN filled with voids and non-radioactive materials similar to what could be found in real nuclear waste drums is ongoing.

ACKNOWLEDGEMENTS

This project has received funding from the European Union's Horizon 2020 research and innovation program under grant agreement number 755371.

References

- [1] E. Valcke et al., (2010). *Osmosis-induced swelling of Eurobitum bituminized radioactive waste in constant total stress conditions*, Journal of Nuclear Materials, 304 - 316.
- [2] A. Mariën et al., (2013). *Osmosis-induced water uptake by Eurobitum bituminized radioactive waste and pressure development in constant volume conditions*, Journal of Nuclear Materials, 348 - 365.
- [3] Gwinner, B. et al., (2006). *Modelling of bituminized radioactive waste leaching. Part II: Experimental validation. The Journal of Nuclear Materials*, 349, 107118.,
- [4] Sercombe, J. et al., (2006). *Modelling of bituminized radioactive waste leaching. Part I: Constitutive equations. The Journal of Nuclear Materials*, 349, 96106.,
- [5] Mouazen, M. et al., (2011). *Effect of γ irradiation on nuclear bituminized waste products (BWP): X-ray microtomography and rheological characterization. The Journal of Nuclear Materials*, 419.,
- [6] Phillips, D.C., Hitchon, J.W., et al., (1983). *Irradiation Swelling of Bituminised Radioactive Wastes, Rep. AERE-R-10925, United Kingdom Atomic Energy Authority, Harwell.*,
- [7] Johnson, D.I., Hitchon, J.W., Phillips, D.C., (1986). *Further Observations of the Swelling of Bitumens and Simulated Bitumen Waste Forms during Gamma-Irradiation, Rep. AERE-R-12292, United Kingdom Atomic Energy Authority, Harwell.*,
- [8] GROUPE CEA, (1983). *Bitumes et Ciment, Etudes et Essais, Groupe CEA, Commissariat à l'énergie atomique, Paris.*,
- [9] IAEA. (1993). *Bituminization processes to condition radioactive wastes, TRS-352. Vienna: IAEA.*,
- [10] IAEA. (1970). *Bituminization of radioactive waste, TRS 116 (136 p.). Vienna: IAEA.*,
- [11] M. Dobrowolska, J. Velthuis, L. Frazão and D. Kikola, *A novel technique for finding gas bubbles in the nuclear waste containers using Muon Scattering Tomography.*, Journal of Instrumentation, vol.13, May 2018
- [12] K.N. Borozdin et al., *Radiographic imaging with cosmic-ray muons*, Nature 422 (2003) 277.

WM2021 Conference, March 8 - 12, 2021, Phoenix, Arizona, USA

- [13] Lorenzo Bonechi and Raffaello D'Alessandro and Andrea Giammanco, *Atmospheric muons as an imaging tool*, physics.ins-det (2019).
- [14] M. Tanabashi et al., *Review of particle physics*, Phys. Rev. D, vol. 98, p. 030001, Aug 2018.
- [15] Yung-Su Tsai, *Pair production and bremsstrahlung of charged leptons.*, Rev. Mod. Phys., 46:815, 1974.
- [16] Z. Papandreou, R. Hakobyan, and N.Kolev, *BCAL radiation length calculations.*, Technical Report 439, GlueX, 2005.
- [17] L. Schultz, *Cosmic ray muon radiography.*, PhD thesis, Portland State University, 2003.
- [18] R. W. Schulte, S. N. Penfold, J. T. Tafas and K. E. Schubert, *A maximum likelihood proton path formalism for application in proton computed tomography.*, Medical Physics 35 (2008) 4849–4856.
- [19] L. J. Schultz, G. S. Blanpied, K. N. Borozdin, A. M. Fraser, N. W. Hengartner, A. V. Klimenko et al., *Statistical reconstruction for cosmic ray muon tomography.*, IEEE Transactions on Image Processing 16 (2007) 1985–1993.
- [20] C. Thomay et al., *A binned clustering algorithm to detect high-z material using cosmic muons.*, 2013 JINST 8 P10013.
- [21] L. Frazão, J. Velthuis, C. Thomay, and C. Steer, *Discrimination of high-z materials in concrete filled containers using muon scattering tomography.*, Journal of Instrumentation, vol.11, no.07, pp. P07020–P07020, Jul 2016.
- [22] C. Thomay, J. Velthuis, T. Poffley, P. Baesso, D. Cussans and L. Frazão, *Passive 3D imaging of nuclear waste containers with Muon Scattering Tomography.*, Journal of Instrumentation, vol.11, March 2016.
- [23] CHANCE 2020. *CHANCE 2020*, <http://chance-h2020.eu>.
- [24] Geant4 Collaboration. *Geant4.*, <https://cern.ch/geant4>.
- [25] C. Hagmann, D. Lange, and D. Wright, *Cosmic-ray shower generator (CRY) for Monte Carlo transport codes.*, In Nuclear Science Symposium Conference Record, 2007. NSS'07. IEEE, volume 2, pages 1143–1146. IEEE, 2007.
- [26] A. Kopp et al., *Non-destructive assay of nuclear waste containers using muon scattering tomography in the Horizon2020 CHANCE project.*, Advancements in Nuclear Instrumentation Measurement Methods and their Applications, ANIMMA, EPJ Web of Conferences 225, 06008, 2020.
- [27] P. Baesso et al., *A high resolution resistive plate chamber tracking system developed for cosmic ray muon tomography.*, Journal of Instrumentation 8.08 (2013): P08006.

9.5 Material identification using machine learning

WM2021 Conference, March 8 - 12, 2021, Phoenix, Arizona, USA

Material Identification of Bodies Stored in Nuclear Waste Drums using Muon Scattering Tomography and Machine Learning – 21102

Michael Weekes*, Ahmad Alrheli*, Dominic Barker*, Daniel Kikola**, Anna Kopp***, Mohammed Mhaidra****, Patrick Stowell*, Lee F Thompson*, Jaap Velthuis*****

* Department of Physics and Astronomy, University of Sheffield, UK

** Warsaw University of Technology, Poland

*** School of Physics, University of Bristol, UK

**** School of Nuclear Science and Technology, University of South China, PRC

ABSTRACT

Muon Scattering Tomography (MST) is a non-destructive assay technique for the characterization of sealed heterogeneous nuclear waste packages. Using MST in combination with machine learning techniques allows for a greater understanding of a waste drum's contents. Here we describe a method that uses multivariate analysis classifiers in combination with MST data to identify objects stored in a waste drum and determine their most likely material composition. We test our method through simulation studies using a generic MST detector system and establish that a wide range of objects can be correctly identified after a 10-day exposure. We also determine the system's efficiency at detecting small uranium objects as $0.90^{+0.07}_{-0.12}$.

INTRODUCTION

Developing techniques to investigate the contents of nuclear waste drums without opening them is vital for proper waste management and safeguarding. Legacy waste drums may be lacking extant documentation of their contents, and even well documented drums may need their contents verified. Such techniques are known as Non-Destructive Assay (NDA), and include calorimetry and cavity ring-down spectroscopy as well as MST. The advantage of NDA techniques is that there is very little risk of the release of hazardous material; 'passive' NDA methods such as MST that do not introduce additional radiation (unlike e.g. X-ray radiography) are even safer, and in general more cost-effective. MST makes use of a flux of muons incident on the Earth's surface that originate from cosmic rays, and so no particles need to be artificially introduced into the system.

BACKGROUND

Muon scattering tomography

Interactions between cosmic rays and the Earth's atmosphere produces a flux of muons. At sea level the muon flux is around $1 \text{ cm}^{-2} \text{ min}^{-1}$ [1] and approximately follows a $\cos^2 \theta$ angular distribution, where θ is zenith angle. Due to their high mass and lack of strong interactions, muons can penetrate a significant distance through matter. Their attenuation interactions can be exploited for muon radiography, allowing the imaging of large structures; this technique has been used to great effect in recent years to image the interiors of volcanoes [2] and ancient pyramids [3]. Muons also undergo scattering interactions in matter, with the strength of the scatterings being highly dependent on the atomic number Z and the density of the medium. This relationship between muon scatterings in a medium and its material characteristics is the underlying principle of MST.

Within dense matter, muons undergo multiple elastic Coulomb scatterings. The distribution of the projected scattering angles is approximately Gaussian, with a width σ given by [4]

$$\sigma \approx \frac{13.6 \text{ MeV}}{\beta c p} \sqrt{X/X_0} \quad (\text{Eq. 1})$$

where β is the ratio of muon speed to the speed of light in a vacuum, c ; p is the muon momentum, X is the material thickness and X_0 is the radiation length of the material.

WM2021 Conference, March 8 - 12, 2021, Phoenix, Arizona, USA

This is defined as the width of material for the energy of a beam of electrons to be reduced by a factor of $1/e$, and is given by

$$x_0 = \rho L_0 \approx \frac{716.4A}{Z(Z+1) \log(287/4Z)} [\text{g cm}^{-2}] \quad (\text{Eq. 2})$$

where L_0 is the path length (defined by radiation length divided by material density ρ) and A is atomic mass. The dependence of the scattering angle distribution on Z allows high- Z material to be distinguished from lower- Z material, making MST a suitable technique for detecting high- Z special nuclear materials such as uranium. With exposure times of several days, full high-resolution images of a waste drum can be produced if required.

To exploit this scattering to assay some volume of interest, such as a waste drum, MST systems generally consist of two sets of particle detectors, with the volume in between (see fig. 1). Each set must consist of multiple layers of detectors, enabling a particle's trajectory to be calculated from the detector hits. This allows the incoming and outgoing trajectories of each muon to be calculated and hence details of the muon's scatterings within the volume, such as scattering angle, to be obtained.

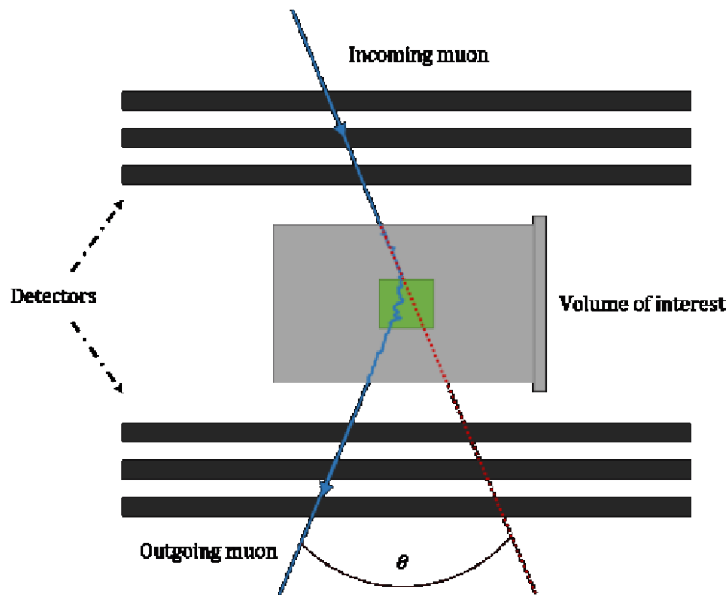


Fig 1: Schematic demonstrating the principle of MST. Particle detectors above and below a waste drum reconstruct the incoming and outgoing muon trajectories, allowing the scattering angle θ (here greatly exaggerated) to be calculated. The muon scatterings are stronger in high- Z material (here green).

METHODS

Simulation setup

Our simulations were performed using CRESTA, a muon tomography simulation platform built on the Geant4 particle transport toolkit [5] and the CRY cosmic ray shower generator [6].

WM2021 Conference, March 8 - 12, 2021, Phoenix, Arizona, USA

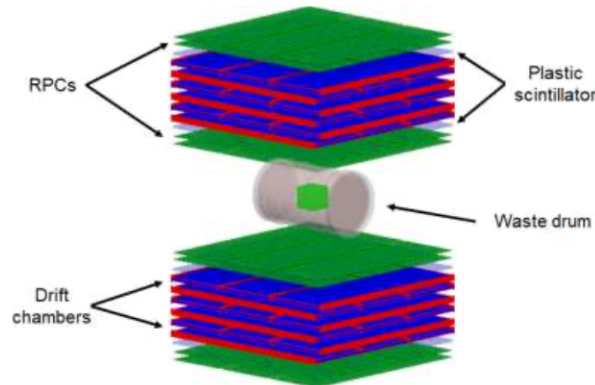


Fig 2: Simulated MST detector system in CRESTA. The detector modules reconstruct muon tracks before and after encountering the central waste drum.

Within CRESTA, we simulated a ‘generic’ MST detector system consisting of two detector modules, each with an active area of approximately 2 m by 2 m, and a space between them suitable for a ~1 m long waste drum (see fig 2).

Each detector module consists of layers of Resistive Plate Chambers (RPCs), polystyrene scintillator trigger planes, and drift chambers. The RPCs have a spatial resolution of ~ 350 μm , and the drift chambers ~ 2 mm. The detectors are arranged in alternating x and y layers which allows a set of muon hits to be recorded and hence the muon trajectory reconstructed. The waste drum is made of steel and approximately 25 mm thick, ~960 mm long and has a radius of ~300 mm. The drum is filled with homogeneous concrete with density 2.3 g cm^{-3} ; the user can place objects of other materials into the concrete at any position or rotation. In CRESTA, cosmic ray muons are generated from a $2 \times 2 \text{ m}$ plane above the upper detection module, with appropriately distributed incident angles and energies sampled for muons at ~sea level. They are then propagated through the system, undergoing the appropriate degree of attenuation and scattering for the material they are in, with hits recorded whenever they encounter the detectors. From these hits the incoming and outgoing tracks (for muons that encounter both detector modules) are reconstructed. To account for the experimental difficulty in measuring the muon momentum precisely, the simulated muon momentum is obtained by adding a smearing factor to the Monte Carlo truth momentum. Following the method of [7], the smearing factor is drawn from a Gaussian with a mean of 0 and a width of 50% the true momentum.

Binned clustering algorithm

There are multiple MST algorithms in use for generating images from scattering angle data. The simplest is the Point of Closest Approach (PoCA) algorithm [8]. The volume of interest is initially divided into a matrix of cubic voxels. PoCA models each muon’s multiple scatterings as if they occurred at a single point, designated the ‘scattering vertex’. This point is found by extrapolating the incoming and outgoing muon tracks into the volume, and calculating the point which minimizes the distance to each. The image is produced by assigning a weight to the voxel containing the point such that higher angle scatterings are weighted more strongly. The assumption of each muon scattering only once is greatly simplifying and in general PoCA produces poor resolution images.

A more advanced MST algorithm is the binned clustering algorithm [9], which builds on PoCA by exploiting the spatial density of the scattering vertices. A higher density of scattering vertices in a voxel corresponds to the presence of high-Z material, as large-angle muon scatterings occur at a higher rate in these materials. In our analysis, we use the binned clustering algorithm in the following form:

1. The volume is divided into cubic voxels of side length 1 cm.

WM2021 Conference, March 8 - 12, 2021, Phoenix, Arizona, USA

2. The incoming and outgoing trajectories of each muon are calculated from the detector hits, from which the corresponding scattering angles are obtained.
3. The positions of each muon's scattering vertex are calculated by finding the point at which the distance between the extrapolated tracks is minimal (as in the PoCA algorithm).
4. All the scattering vertices inside each 1 cm³ voxel are sorted into descending order by the scattering angle of the corresponding muon. The first *n* entries in the list are kept and the rest discarded. Voxels that contain less than *n* scattering vertices are discarded.
5. For each pair of vertices *i, j* in each voxel, a metric value *m_{i,j}* is calculated as

$$m_{i,j} = \frac{|\mathbf{v}_i - \mathbf{v}_j|}{(\theta_i p_i)(\theta_j p_j)} \tag{Eq. 3}$$

where \mathbf{V}_i , θ_i and p_i are, respectively, the scattering vertex position, scattering angle, and (smeared) momentum of muon *i*. The momentum information is necessary to exclude high-angle scattering of low-momentum muons mimicking high-angle scattering by high-Z material. Smaller metric values correspond to a higher density of scattering vertices, and larger scattering angles, indicating high-Z material.

6. For each voxel, the distribution of $\log(m_{i,j})$ values is obtained and the median calculated. This median is the discriminator value for that voxel; the final image is a map of these discriminators. Images from simulation studies of concrete-filled waste drums made with this algorithm (see fig. 3) show that high-Z objects are clearly visible when viewing slices of the final 3D image.

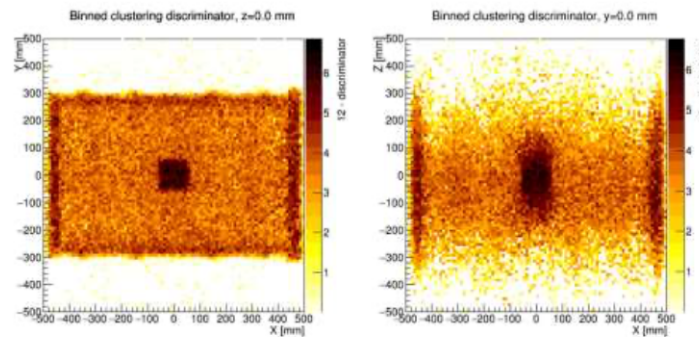


Fig 3: xy (left) and xz (right) slices from a binned clustering output image of a concrete-filled 1 m long waste drum containing a 10 cm uranium cube, centred. The exposure time was 10 days and the algorithm's parameter *n* was set to 5.

Multivariate analysis

Machine learning techniques can be used in conjunction with MST to allow deeper analysis of a waste drum's contents. One approach is to design Multi-Variate Analysis (MVA) classifiers: machines trained to recognize from some set of variables whether the set is more likely to belong to a previously defined 'signal' class or one or more 'background' classes. Previously MVA classifiers have been used to discriminate, on a global level, drums containing blocks of lead or uranium [10]. To allow for a 'local' approach, i.e. to obtain material information down to the scale of the 1 cm voxels, we passed a set of variables calculated from the binned clustering algorithm to the MVA classifiers. These had the advantage that a set of variables could be calculated for every voxel individually.

WM2021 Conference, March 8 - 12, 2021, Phoenix, Arizona, USA

As explained in the previous section, the binned clustering algorithm produces, for each voxel, a set of m_j metric values. By default the median only of the distribution of $\log(m_j)$ values was determined and used to produce an image. In our approach, we instead bin the $\log(m_j)$ values, and use the (normalized) bin counts (see fig. 4) as a set of variables that are then passed to MVA classifiers.

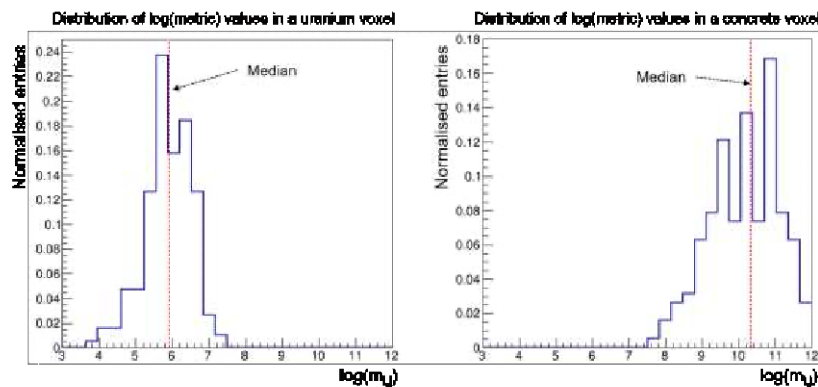


Fig 4: Comparison of $\log(\text{metric})$ distributions for voxels corresponding to uranium (left) and concrete (right). The median of each distribution is used as the discriminator in the binned clustering algorithm. The normalized bin counts (as well as the median) are used as the MVA classifier input variables.

Our MVA classifiers were created and applied using TMVA [11], a ROOT-integrated [12] machine learning platform. TMVA allows the user to create classifiers that use multiple machine learning methods, such as Fisher's linear discriminant or a multi-layer perceptron, simultaneously. One can then determine from the results which classifier is best suited to the problem. In our case, we found that a gradient-boosted decision tree method gave the best results whilst also being among the least computationally intensive. A trained decision tree-based classifier uses a linked series of cuts on the set of variables to attempt to correctly classify the set. 'Gradient-boosted' refers to a method of combining many trees to improve the accuracy of the overall classifier.

MVA training

Our MVA classifiers were trained to recognize four different materials: concrete, iron, lead and uranium. The training sets were simulated drums containing 20 cm cubes of each material, centred in the drum. A 10-day exposure of each was simulated, then the binned clustering algorithm (with its n parameter set to 20) was applied to the results. From the algorithm output the MVA variables for the voxels inside the cubes were obtained and passed to the classifiers. Initially, we used a single non-binary classifier and designated the concrete set as 'signal', and the iron, lead and uranium sets as 'backgrounds'. Trained in this way, this classifier will produce an output value when applied to other voxels, and designate them as being 'signal-like' or 'background-like' based on whether the output value is above or below the classifier's calculated optimum cut (see fig. 5). The effectiveness of this classifier can be quantified through a Receiver Operating Characteristic (ROC) curve. This is a plot of the achieved true positive rate against false positive rate for different cuts on the classifier output; the point of maximum curvature on the ROC curve corresponds to the optimum cut. The Area Under the Curve (AUC) of a ROC curve is a measure of the classifier's discriminating power, with an AUC of 1 indicating a perfect classifier, and an AUC of 0.5 indicating that the classifier performs no better than random classification.

WM2021 Conference, March 8 - 12, 2021, Phoenix, Arizona, USA

The non-binary concrete vs iron, lead and uranium classifier has an AUC ~ 0.996, indicating it is highly effective at distinguishing concrete from the other materials.

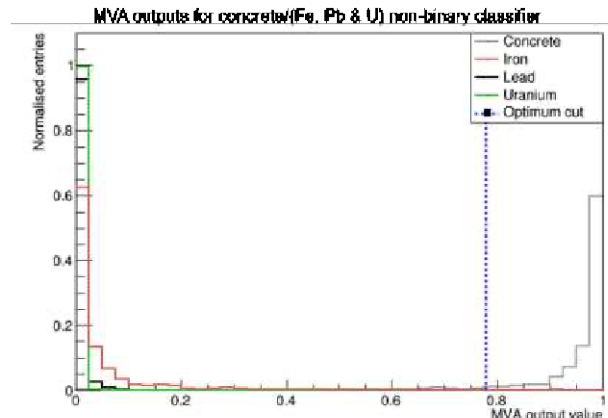


Fig 5: Responses to training sets from non-binary MVA classifier trained with concrete as signal and iron, lead and uranium as backgrounds. Voxels that return a response value above the marked cut are considered 'signal (i.e. concrete)-like'.

Thus the classifier is able to approximately identify the voxels corresponding to objects of iron, lead or uranium stored in the concrete-filled drum. We are then able to remove all voxels except these from the binned clustering algorithm output image and show the stored objects only.

Clustering

With these 'object voxels' identified and separated, we used a clustering algorithm to group them into clusters, with each cluster approximately corresponding to a body stored in the waste drum. This was achieved through the widely used *k*-means++ clustering algorithm [13]. In summary, one selects a set of random data points to be the initial cluster centroids, assigns each data point to the cluster with the closest centroid, then calculates new cluster centroids as the centers of these new clusters. This is repeated until the cluster centroids locations converge.

A complication of this algorithm is that it requires the number of clusters *k* as an input. This is best resolved by simply running the algorithm with a range of *k* values, then using some figure of merit to assess which clustering solution is the most natural. In our case, we calculate the Dunn index [14] for the *k*-means++ output for a range of *k* values. The Dunn index can be defined as the ratio between some measure of the minimum inter-cluster distance and some measure of the maximum intra-cluster distance. A high Dunn index therefore corresponds to compact and well-separated clusters. We found that choosing *k* so as to maximize the Dunn index was effective at obtaining the most natural value for *k*, i.e. the actual number of stored bodies in the drum.

Finally, we apply some simple filtering to remove first image noise (i.e. voxels that correspond to concrete in the drum but are incorrectly passed by the classifier, which will occur to approximately 0.1% of the concrete voxels due to the classifier's AUC) and subsequently to remove the 'outer layer' of voxels from each object cluster. This latter step is necessary as there will be a degree of smearing between a stored object and the concrete background, due to scattering vertices from muons that did not pass through the object being reconstructed within it. Fig. 6 shows the results of successively applying the concrete non-binary classifier, the *k*-means++ clustering algorithm, and the described filtering to MST data from a 10-day simulation of a drum containing 15 cm cubes of iron, lead and uranium.

WM2021 Conference, March 8 - 12, 2021, Phoenix, Arizona, USA

The voxels in the binned clustering algorithm output image corresponding to the stored cubes have been successfully isolated and clustered.

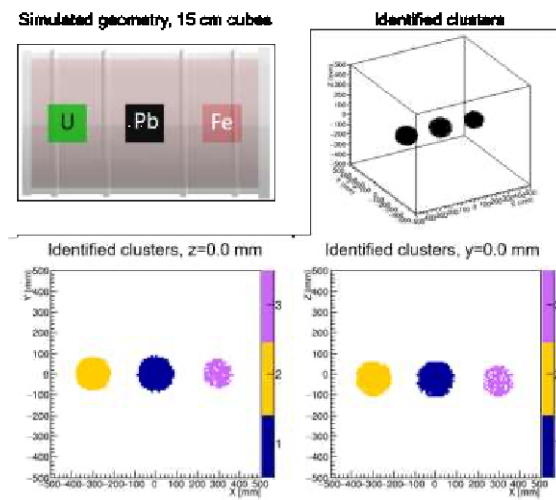


Fig 6: Result of applying filtering and clustering algorithms to a simulated drum containing three cubes. Clockwise from top left: the simulated drum geometry, a 3D view of the filtered image, xz slice of the filtered image showing clustering solution, xyslice of the filtered image.

Calculating material values

Two further MVA classifiers are now applied to these identified objects to obtain material information. These are a non-binary classifier with iron as the ‘signal’ case and lead and uranium as ‘background’ cases, and finally a binary lead-uranium classifier (with uranium as ‘signal’). The former has ROC AUC of ~0.993, and the latter ~0.811 (AUCs reduce as the materials become more similar in Z and thus harder to distinguish).

These classifiers will return a response value for each voxel passed to them. To obtain a single result for each identified cluster, all of the voxels in a cluster are passed to the classifier, and the proportion of response values that fall above the cut is calculated. For the iron vs. lead and uranium non-binary classifier, this value will reflect how ‘iron-like’ the cluster appears. The uranium-lead binary classifier value will reflect how ‘uranium-like’ the object appears, and 1 – this value how ‘lead-like’ it appears (the lead and uranium values are also normalized by multiplying by 1 – the iron value from the non-binary classifier). For objects of similar volume to the 20 cm cubes used for training the classifiers, the largest value corresponds to the correct material, and objects of different materials are clearly distinguished by the three material values (see fig. 7).

WM2021 Conference, March 8 - 12, 2021, Phoenix, Arizona, USA

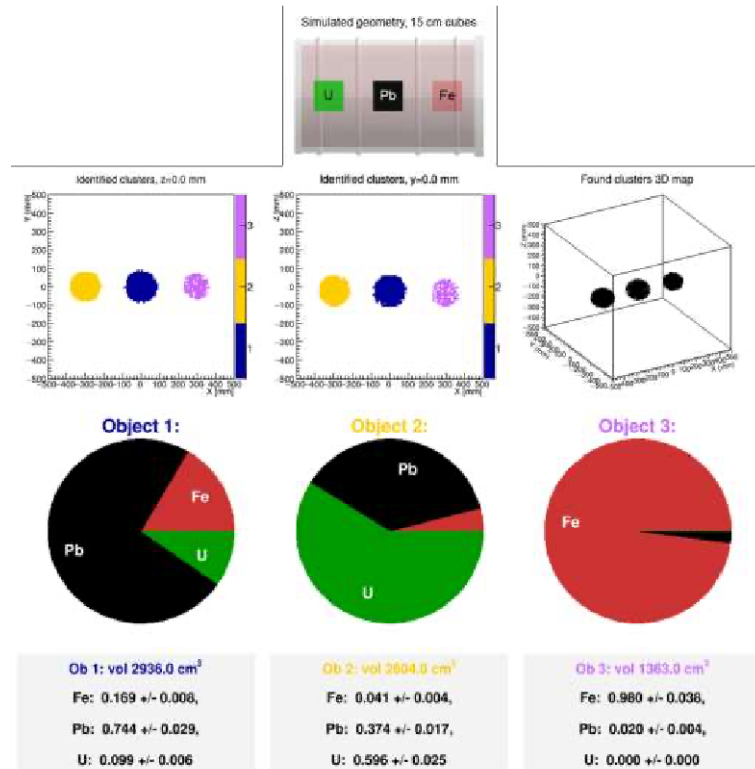


Fig. 7: Calculated material values for successfully identified clusters corresponding to three stored 15 cm cubes of uranium, lead and iron. In each case, the largest value corresponds to the true material.

However, this does not necessarily hold for objects significantly larger or smaller than the 20 cm training cubes. This is because muons passing through a greater thickness of high-Z material will undergo more scatterings, and so the final scattering angle will be, in general, larger. This will propagate through to the binned clustering algorithm metric values, and hence to the MVA classifiers. Therefore, larger objects appear 'shifted' to higher-Z material and vice versa. This can lead to e.g. a large lead object appearing similar to a small uranium object, or a small uranium object being interpreted as lead. Fortunately this effect can be corrected for by calibrating an object's material values to its volume. We achieved this by applying the system to a series of spheres of increasing volume and different materials, producing a set of calibration curves (fig. 8).

Thus to obtain a final material decision for an object, its material values are calculated using the method described above, and its volume simply from the number of 1 cm³ voxels in the cluster. This volume is input to the calibration curves, producing sets of 'expected' material values if the object was made of iron, lead or uranium. The actual material values are compared to each set (in terms of Euclidean distance), and the material with the best match (minimal distance) identified.

WM2021 Conference, March 8 - 12, 2021, Phoenix, Arizona, USA

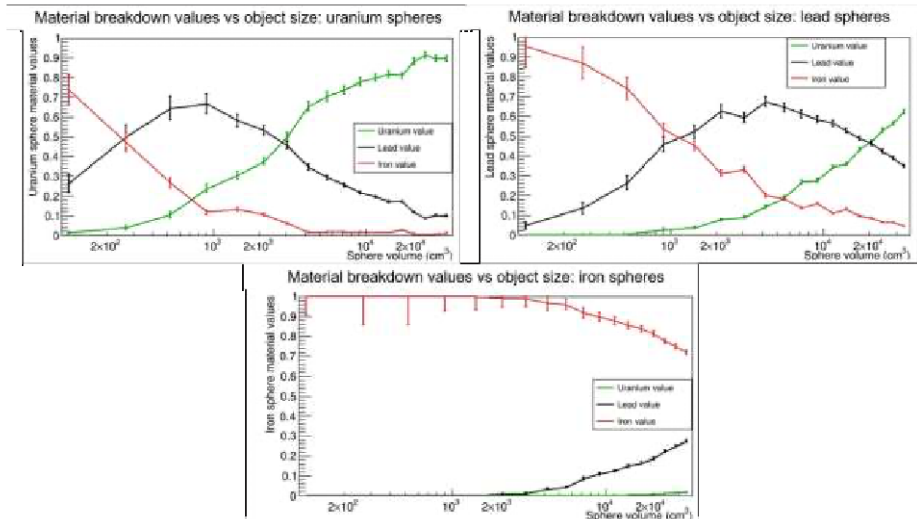


Fig. 8: Calibration curves used to make a material decision for an object from its MVA-calculated material values and volume. Plots show the three material values for a series of spheres of increasing volume, made of uranium (top left), lead (top right) or iron (bottom).

RESULTS

Here are shown some example results of applying this system to a series of more complicated simulated geometries: a set of three 10 cm cubes (fig. 9), a set of three irregular shaped and positioned objects (fig. 10), and a set of five varied objects (fig. 11). The system performs well in all cases, correctly identifying the number and position of all the stored objects. All the uranium objects present are correctly identified. Even the smaller uranium objects, which have smaller uranium values than larger objects, are correctly identified when properly calibrated by their volumes. In total from these examples, 10 out of 11 objects are correctly identified. One lead object in the five object case is misclassified as being iron. The object is

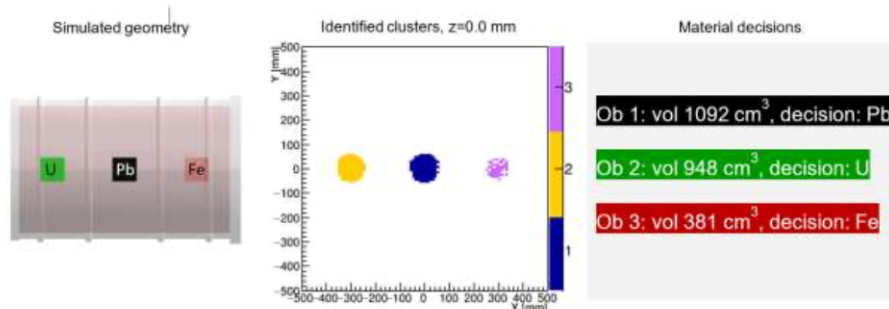


Fig. 9: Material results for a simple geometry of three 10 cm cubes of lead, uranium and iron, centred in the drum and aligned with the voxel grid. All three objects are correctly identified. Left to right: simulated geometry, xZ slice of final image showing clustering solution, object volumes and material decisions.

WM2021 Conference, March 8 - 12, 2021, Phoenix, Arizona, USA

a small lead tube, and likely indicates a vulnerability of the system to less-spherical objects.

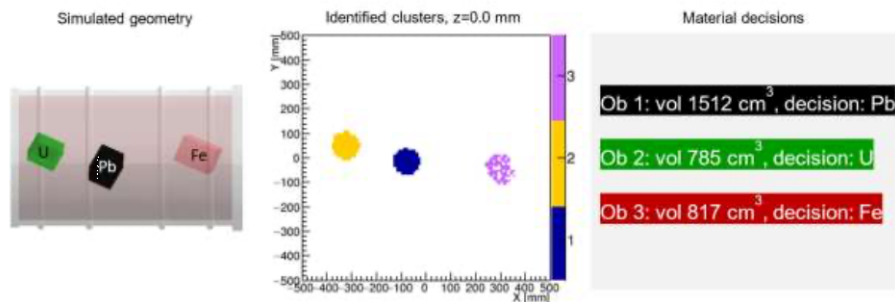


Fig. 10: Material results for a more complex geometry of three cuboids, rotated away from the voxel grid. Again all three objects are correctly identified. Left to right: simulated geometry, XZ slice of final image showing clustering solution, object volumes and material decisions.

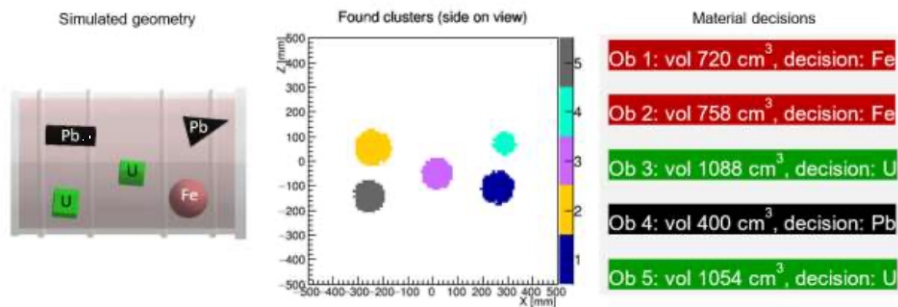


Fig. 11: Material results for a complex geometry of five variously-shaped objects. The uranium bodies are correctly identified. One lead object, a small tube, has been misclassified as iron. Left to right: simulated geometry, side-on view of final clustered image, object volumes and material decisions.

Efficiency at uranium object detection

Finally, the system’s efficiency at detecting small uranium objects (the true positive rate) was calculated. This was done using a set of randomly generated waste drum geometries, each containing three spheres with 6 cm radii. The spheres were constrained to not intersect each other but otherwise randomly dispersed in the drum. 100 simulations were run in total; half contained one uranium, one lead and one iron sphere, and half contained two lead spheres and one iron sphere. Defining a true positive identification of a uranium object as an object close to the uranium sphere’s true location being identified and classified as uranium, we calculated a true positive rate of $0.90^{+0.07}_{-0.12}$. On inspection, most failed cases corresponded to drum geometries in which the iron and uranium spheres were very close together, causing them to be interpreted as a single object, and usually classified as lead. With a false positive defined as any object in a drum not containing uranium being assigned uranium, we found a false positive rate of $0.12^{+0.12}_{-0.07}$. Similarly, most false positives were cases where the two lead spheres were very close together.

WM2021 Conference, March 8 - 12, 2021, Phoenix, Arizona, USA

CONCLUSIONS

Machine learning techniques in combination with MST allow for more information about a waste drum's contents to be extracted than MST alone. MVA classifiers trained on variables obtained from the binned clustering algorithm are effective at identifying the materials of objects stored in waste drums. One such classifier, trained on concrete, iron, lead and uranium samples, has been used to successfully isolate the voxels corresponding to stored objects in a binned clustering output image of a waste drum. These remaining voxels can be sorted into clusters, each approximately corresponding to a stored body in the drum, using simple clustering algorithms.

Additional MVA classifiers can be used to give further material information about each identified object. When combined with calibration curves calculated from a set of test cases, the outputs of these classifiers can be used to successfully identify objects composed of iron, lead or uranium for a wide range of object shapes, locations and sizes.

With a sample set of randomly generated drum geometries, we were able to correctly identify uranium objects on a scale of ~10 cm with an efficiency of $0.90^{+0.07}_{-0.12}$, and a corresponding false positive rate of $0.12^{+0.17}_{-0.07}$, indicating that this approach is effective at identifying uranium objects stored inside waste drums. The identified vulnerabilities include objects of materials with very different Z values, such as iron and uranium, that are close together; uranium objects can be misidentified in such cases.

REFERENCES

- Schultz, L.J., Blanpied, G.S., Borozdin, K.N., Fraser, A.M., Hengartner, N.W., Klimenko, A.V., Morris, C.L., Orum, C. and Sossong, M.J., 2007. Statistical reconstruction for cosmic ray muon tomography. *IEEE transactions on Image Processing*, 16(8), pp.1985-1993.
- Tanaka, H.K., Uchida, T., Tanaka, M., Shinohara, H. and Taira, H., 2010. Development of a portable assembly-type cosmic-ray muon module for measuring the density structure of a column of magma. *Earth, planets and space*, 62(2), pp.119-129.
- Morishima, K., Kuno, M., Nishio, A., Kitagawa, N., Manabe, Y., Moto, M., Takasaki, F., Fujii, H., Satoh, K., Kodama, H. and Hayashi, K., 2017. Discovery of a big void in Khufu's Pyramid by observation of cosmic-ray muons. *Nature*, 552(7685), pp.386-390.
- Lynch, G.R. and Dahl, O.I., 1991. Approximations to multiple Coulomb scattering. *Nuclear Instruments and Methods in Physics Research Section B: Beam Interactions with Materials and Atoms*, 58(1), pp.6-10.
- Agostinelli, S., Allison, J., Amako, K.A., Apostolakis, J., Araujo, H., Arce, P., Asai, M., Axen, D., Banerjee, S., Barrand, G.2. and Behner, F., 2003. GEANT4—a simulation toolkit. *Nuclear instruments and methods in physics research section A: Accelerators, Spectrometers, Detectors and Associated Equipment*, 506(3), pp.250-303.
- Hagmann, C., Lange, D. and Wright, D., 2007, October. Cosmic-ray shower generator (CRY) for Monte Carlo transport codes. In *2007 IEEE Nuclear Science Symposium Conference Record (Vol. 2, pp. 1143-1146)*. IEEE.
- Morris, C.L., Alexander, C.C., Bacon, J.D., Borozdin, K.N., Clark, D.J., Chartrand, R., Espinoza, C.J., Fraser, A.M., Galassi, M.C., Green, J.A. and Gonzales, J.S., 2008. Tomographic imaging with cosmic ray muons. *Science & Global Security*, 16(1-2), pp.37-53.
- Riggi, S., Antonuccio-Delogu, V., Bandieramonte, M., Becciani, U., Costa, A., La Rocca, P., Massimino, P., Petta, C., Pistagna, C., Riggi, F. and Sciacca, E., 2013. Muon tomography imaging algorithms for nuclear threat detection inside large volume containers with the Muon Portal detector. *Nuclear Instruments and Methods in Physics Research Section A: Accelerators, Spectrometers, Detectors and Associated Equipment*, 728, pp.59-68.
- Thomay, C., Velthuis, J.J., Baesso, P., Cussans, D., Morris, P.A.W., Steer, C., Burns, J., Quillin, S. and Stapleton, M., 2013. A binned clustering algorithm to detect high-Z material using cosmic muons. *Journal of Instrumentation*, 8(10), p.P10013.

WM2021 Conference, March 8 - 12, 2021, Phoenix, Arizona, USA

10. Frazão, L., Velthuis, J., Thomay, C. and Steer, C., 2016. Discrimination of high-Z materials in concrete-filled containers using muon scattering tomography. *Journal of Instrumentation*, 11(07), p.P07020.
11. Hoecker, A., Speckmayer, P., Stelzer, J., Therhaag, J., von Toerne, E. and Voss, H., 2007. TMVA - Toolkit for Multivariate Data Analysis, PoS ACAT 040, arXiv:physics/0703039
12. Brun, R., and Rademakers, F., 1996. ROOT - An Object Oriented Data Analysis Framework, Proceedings AIHENP'96 Workshop, Lausanne, Sep. 1996, Nucl. Inst. & Meth. in Phys. Res. A 389 (1997) 81-86.
13. Arthur, D. and Vassilvitskii, S., 2006. k-means++: The advantages of careful seeding. Stanford.
14. Dunn, J.C., 1973. A fuzzy relative of the ISODATA process and its use in detecting compact well-separated clusters.

ACKNOWLEDGEMENTS

This project has received funding from the Euratom research and training programme 2014–2018 under grant agreement No 755371.





PUBLISHED BY IOP PUBLISHING FOR SISSA MEDIALAB

RECEIVED: December 4, 2020
 REVISED: February 12, 2021
 ACCEPTED: February 24, 2021
 PUBLISHED: May 6, 2021

Material identification in nuclear waste drums using muon scattering tomography and multivariate analysis

M.J. Weekes,^{a,*} A.F. Alrheli,^a D. Barker,^a D. Kikoła,^b A.K. Kopp,^c M. Mhaidra,^{b,c}
 J.P. Stowell,^a L.F. Thompson^a and J.J. Velthuis^c

^aUniversity of Sheffield, Department of Physics and Astronomy,
 Hounsfield Road, Sheffield, S3 7RH, U.K.

^bWarsaw University of Technology,
 Pl. Politechniki 1, 00-661 Warsaw, Poland

^cUniversity of Bristol, School of Physics, HH Wills Physics Laboratory,
 Tyndall Avenue, Bristol BS8 1TL, U.K.

E-mail: mweekes1@sheffield.ac.uk

ABSTRACT: The use of muon scattering tomography for the non-invasive characterisation of nuclear waste is well established. We report here on the application of a combination of feature discriminators and multivariate analysis techniques to locate and identify materials in nuclear waste drums. After successful training and optimisation of the algorithms they are then tested on a range of material configurations to assess the system's performance and limitations. The system is able to correctly identify uranium, iron and lead objects on a few cm scale. The system's sensitivity to small uranium objects is also established as $0.90^{+0.07}_{-0.12}$, with a false positive rate of $0.12^{+0.12}_{-0.07}$.

KEYWORDS: Pattern recognition, cluster finding, calibration and fitting methods; Search for radioactive and fissile materials; Particle tracking detectors

*Corresponding author.

 © 2021 The Author(s). Published by IOP Publishing Ltd on behalf of Sissa Medialab. Original content from this work may be used under the terms of the [Creative Commons Attribution 4.0 licence](https://creativecommons.org/licenses/by/4.0/). Any further distribution of this work must maintain attribution to the author(s) and the title of the work, journal citation and DOI.

<https://doi.org/10.1088/1748-0221/16/05/P05007>

2021 JINST 16 P05007



Contents

1 Introduction	1
2 Muon scattering tomography	2
2.1 Binned clustering algorithm	3
2.2 System configuration	5
3 Multivariate analysis	6
3.1 MVAs and muon tomography	6
3.2 Training MVA classifiers	9
3.3 Momentum information	9
4 Identifying stored bodies	11
4.1 Removal of concrete background	11
4.2 Clustering	13
5 Results and analysis	16
5.1 Applying MVAs to clustered objects	16
5.2 Obtaining material decisions	18
5.3 Sensitivity	22
6 Conclusions	23

2021 JINST 16 P05007

1 Introduction

It is important to develop non-destructive methods to determine the contents of sealed nuclear waste packages, in order to minimise the risks of environmental contamination and personnel radiation exposure and to allow for more effective safeguarding. Non-Destructive Assay (NDA) techniques in current use include calorimetry and Muon Scattering Tomography (MST).

NDA techniques can analyse drum contents in a variety of ways. For example, calorimetry can be used to measure the mass of nuclear material inside a container by its heat emission [1]. In contrast, MST (with exposure times of several days to weeks) can produce full 3D images of a volume of interest, allowing individual objects inside the drum to be viewed as well as giving information on their atomic number Z and density [2].

Simulation studies are useful tools to assess MST techniques and algorithms; the technique described in this paper was developed and tested via Monte Carlo simulations. It uses MST data in combination with Multi-Variate Analysis (MVA) classifiers and clustering algorithms to approximately identify the locations and shapes of objects stored in a concrete-filled waste drum. Subsequently, additional trained classifiers are applied to each identified object to classify them as 'iron',

‘lead’, or ‘uranium’, representing low-threat medium-Z material, low-threat high-Z material, and high-threat high-Z material respectively. The use of these four materials allows three classification problems of interest to be investigated: separation of stored objects from the concrete background, separating medium- and high-Z materials, and distinguishing between two high-Z materials.

Previous applications of machine learning techniques to MST imaging have demonstrated methods for distinguishing between drums containing uranium and lead blocks [3] and for reconstructing the size of uranium blocks [4]. Our system builds on these through the ability to isolate and identify multiple distinct bodies of different materials and sizes in a waste drum. Other previous research into combining machine learning and MST include applications in cargo scanning [5, 6], a related problem for which short exposure times are required.

2 Muon scattering tomography

Cosmic rays interact with the Earth’s atmosphere to produce showers of particles, some of which subsequently decay to muons, resulting in a muon flux at sea level of around $1 \text{ cm}^{-2} \text{ min}^{-1}$ [7]. These cosmic ray muons are highly penetrating due to their large mass and lack of strong interactions. They have an angular distribution that varies approximately as $\cos^2 \theta$, where θ is the zenith angle. Muons are also highly sensitive to the atomic number Z of the material they are passing through, making them suitable candidates for tomographic imaging of nuclear waste drums.

Muons undergo multiple elastic Coulomb scatterings in matter, with the projected scattering angles following an approximately Gaussian distribution with width σ given by

$$\sigma \approx \frac{13.6 \text{ MeV}}{\beta c p} \sqrt{X/X_0} \quad (2.1)$$

where β is the muon speed divided by the speed of light in a vacuum, c ; p is the muon momentum, X is the thickness of the material and X_0 is the radiation length of the material [8]. The latter is given by

$$X_0 = \frac{716.4A}{Z(Z+1) \ln(287/\sqrt{Z})} [\text{g} \cdot \text{cm}^{-2}] \quad (2.2)$$

where ρ is the material density and A is atomic mass [9].

A general MST experiment consists of two sets of particle detectors, one above and one below some volume of interest such as a waste drum (see figure 1). Multiple layers of detector are necessary in order to construct a three dimensional trajectory for each muon from the detector hits. This allows the incoming and outgoing trajectories of each muon to be measured and hence the muon scattering angles to be calculated.

Several algorithms have been developed to enable imaging of a volume of interest from MST data. The simplest is the Point of Closest Approach (PoCA) algorithm [10], which models a muon’s multiple scatterings as a single scattering at a single point (‘scattering vertex’), found by extrapolating the incoming and outgoing tracks into the volume and finding the point which minimises the distance to each. This assumption allows for fast computation at the expense of image quality. A more advanced MST algorithm has been used in this study (see section 2.1) which builds on PoCA by exploiting the spatial density of scattering vertices; a high density of scattering vertices corresponds to the presence of high-Z material as large-angle muon scatterings occur more often in such materials.

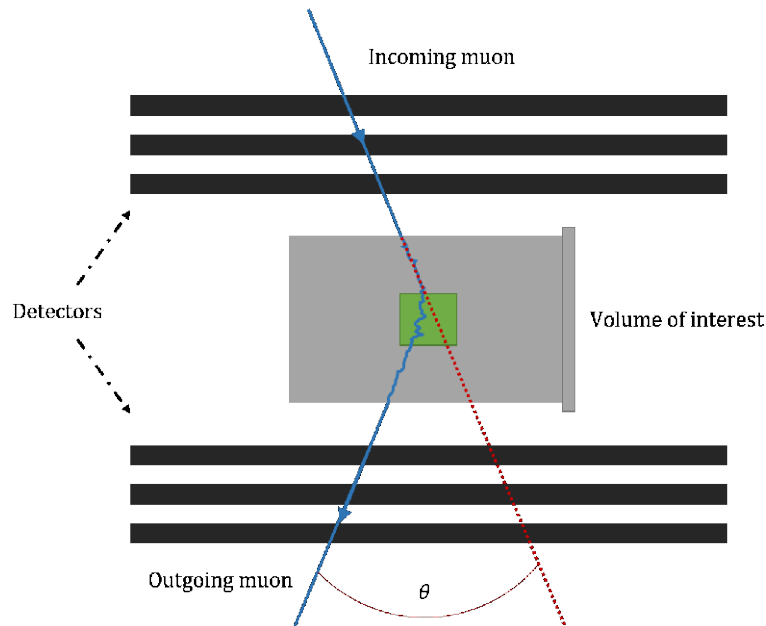


Figure 1. Schematic showing the principle of muon scattering tomography applied to a nuclear waste drum containing a block of high-Z material (in green). Particle detectors measure the trajectories of muons before and after encountering the volume of interest, allowing the scattering angle θ (here exaggerated) to be calculated.

2.1 Binned clustering algorithm

This algorithm, developed in [11], improves on the widely-used Point of Closest Approach (PoCA) muon tomography algorithm [2] by taking into account the degree of spatial clustering of muon scattering vertices. A higher density of vertices corresponds to higher-Z materials (once the muon momentum is accounted for, see below) as strong muon scatterings take place with greater frequency in such materials.

The volume is divided into cubic voxels of sidelength 1 cm. The incoming and outgoing muon tracks are extrapolated through the volume, and the point at which the distance between the tracks is minimal (the PoCA) is designated as the scattering vertex for the muon. This is repeated for all of the detected muons that encounter the volume of interest. Next, the scattering vertices inside each 1 cm³ voxel are sorted by the scattering angle of the corresponding muon, and the vertices corresponding to the α largest scattering angles are kept (voxels which contain less than α vertices are discarded). This factor of α is an important tunable parameter of the algorithm. High values of α improve the contrast between high and low-Z materials, as a greater sample of muons are kept, but reduce image 'quality' (i.e. the number of non-empty voxels in the image) as more voxels fall below the cut and are removed from the image.

2021 JINST 16 P05007

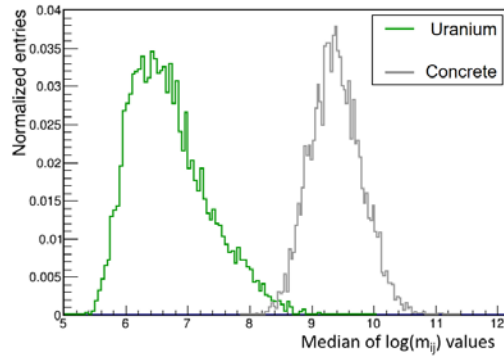


Figure 2. Comparison of distributions of the binned clustering algorithm discriminator, for 20 cm cubes of uranium and concrete. Lower discriminator values correspond to higher Z material.

For each of the $\binom{n}{2}$ pairs of vertices i, j in each voxel, a metric value m_{ij} is calculated according to

$$m_{ij} = \frac{|\mathbf{V}_i - \mathbf{V}_j|}{(\theta_i \tilde{p}_i) \cdot (\theta_j \tilde{p}_j)} \quad (2.3)$$

where \mathbf{V}_i , θ_i and \tilde{p}_i are respectively the position, scattering angle and normalised (by a factor of 3 GeV/c) momentum of muon i . Weighting by muon momentum is necessary as large scattering angles could indicate low-momentum muons being scattered in low-Z materials instead of strong scattering in high-Z materials. In an experimental system, the muon momentum can be estimated using the muon scatterings between the detector planes, as the planes are of known material and thickness. Following the method of [12], for our simulations the momentum was obtained by adding a smearing factor to the Monte Carlo truth momentum. The smearing factor was drawn from a Gaussian with width 50% of the Monte Carlo truth momentum.

Finally, the median of the distribution of $\log(m_{ij})$ in a voxel is determined; this is the algorithm's discriminator value for that voxel. Comparing the distributions of this discriminator for high- and low-Z materials shows that the discriminator is sensitive to Z (see figure 2).

For imaging purposes, each voxel is filled with its discriminator value as described above, creating a tomogram of the volume of interest. Viewing slices of discriminator values through the image (see figure 3) allows regions of high-Z material to be identified visually. This gives a degree of information about the locations and morphologies of objects stored in the drum. However, it is vulnerable to a vertical smearing effect inherent in the PoCA reconstruction, and without an object of known material for comparison, it is difficult to determine the specific materials of objects 'by eye'. Additionally, without any way to automatically remove background materials such as the steel drum and concrete matrix, the 3D image must be viewed in slices to determine the locations of stored objects.

By default, the binned clustering algorithm only takes into account the median of the $\log(m_{ij})$ distribution in each voxel. To test the possibility that additional material information is encoded in the shape of the $\log(m_{ij})$ value distribution, variables capturing the shape were used to train MVA classifiers. These classifiers are then used to separate the regions of the image corresponding to

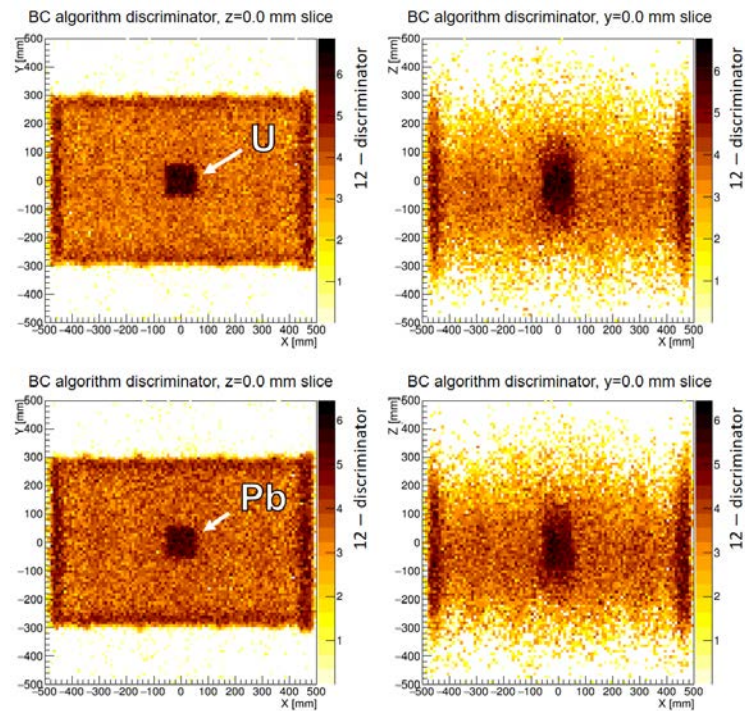


Figure 3. *xy* (left) and *xz* (right) slices from binned clustering output images of waste drums containing 10 cm side length cubes of uranium (top) and lead (bottom). Exposure time = 10 days, $n = 5$. The smearing effect along the z axis is due to uncertainty in the scattering vertex z coordinate for tracks with small scattering angles. Note that the plotted discriminator values have been subtracted from 12 for visual clarity.

objects stored in the drum from the concrete matrix. Subsequently the classifiers are used to assign a material to each identified object.

2.2 System configuration

All simulations were performed using CRESTA [13], a cosmic ray simulation platform built on the Geant4 [14] particle physics toolkit and the CRY [15] cosmic ray library. Within CRESTA a MST detector system comprising two particle detector modules above and below a waste drum was simulated (see figure 4). This represents a ‘generic’ MST detector system, designed for imaging a 1 m waste drum. The detector modules are 2 m by 2 m and each consists of two layers of resistive plate chambers (RPCs), polystyrene scintillator triggers and three layers of drift chambers. The RPCs and drift chambers have spatial resolutions of $\sim 350 \mu\text{m}$ and $\sim 2 \text{mm}$ respectively. The detectors are arranged in alternating x and y layers, allowing 3D muon hits to be recorded and the incoming and outgoing tracks reconstructed.

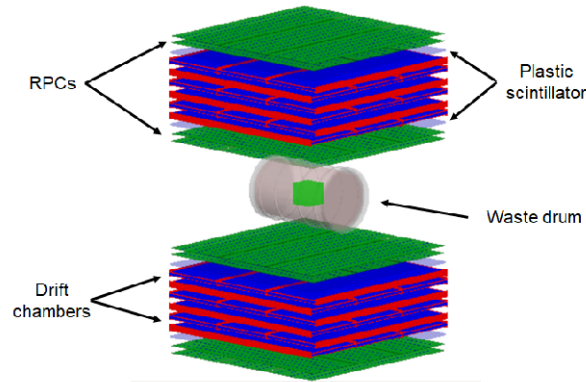


Figure 4. MST detector system simulated in CRESTA: detector modules above and below a waste drum, in which objects can be placed. The detector modules are approximately 2 × 2 m.

The waste drum is made of steel (approx. 91% iron, 9% carbon; element isotopes in natural abundances). It is approximately 100 cm in length and 30 cm in radius (see figure 5 for precise dimensions), and is filled with homogeneous concrete of density 2.3 g cm^{-3} .

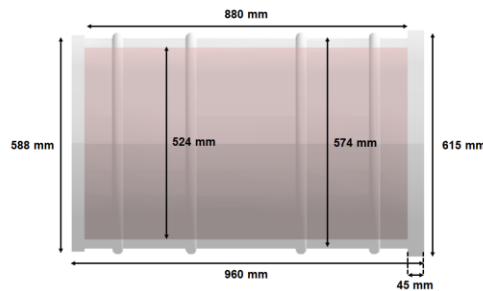


Figure 5. The simulated concrete-filled steel nuclear waste drum used in CRESTA, with its dimensions.

2021 JINST 16 P05007

3 Multivariate analysis

3.1 MVAs and muon tomography

Fração et al. [3] used MVA classifiers trained on simulated MST data to discriminate between waste drums containing lead and uranium blocks. This method can be thought of in a 'global' sense, distinguishing between two categories of waste drum but not analysing the specific drum contents in terms of bodies encased in the concrete. Our approach by contrast is 'local', as we are able to produce localised material information down to the scale of single 1 cm voxels. This approach requires longer exposure times (of the order of several days rather than hours) but gives more

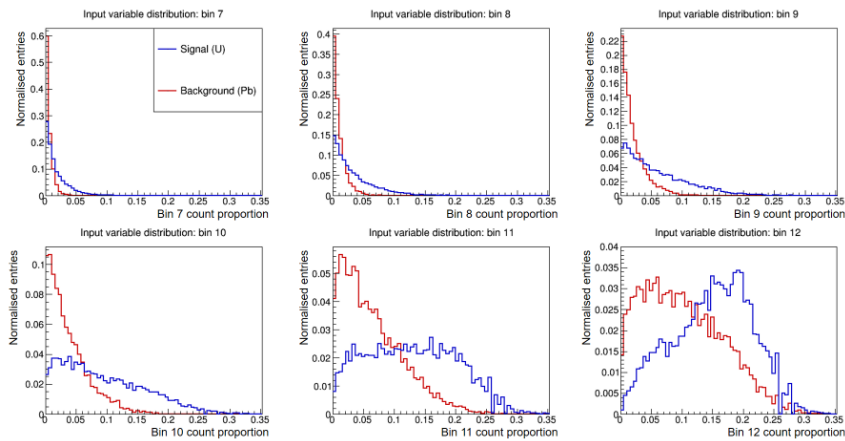


Figure 7. Example distributions of some of the input variables used to train the MVA classifiers, here specifically a binary uranium-lead classifier. The variables are the normalised bin counts (see figure 6) of the $\log(m_{ij})$ values calculated by the binned clustering MST algorithm. The signal set (blue) are voxels in a 20 cm cube of uranium, and the background set (red) an equivalent cube of lead.

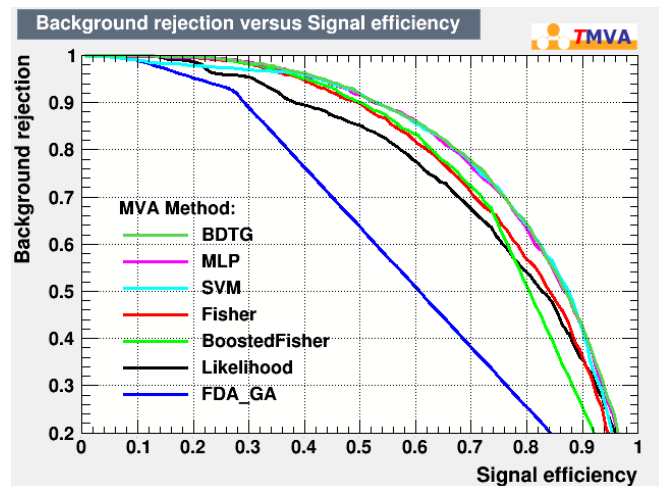


Figure 8. ROC curves showing discriminating power for several TMVA methods when applied to the described binned clustering algorithm variables, for distinguishing voxels in 20 cm cubes of uranium and lead.

2021 JINST 16 P05007

3.2 Training MVA classifiers

The MVAs were trained on a number of simulated MST muon track data corresponding to a 10 day exposure of four different waste drums: an ‘empty’ drum containing only concrete, and three drums containing 20 cm side length cubes (see figure 9) of iron, lead and uranium, in the centre of the drum and aligned with its central axis. Only the voxels in the cube (or the equivalent volume for the homogeneous empty drum) were passed to the classifier. The binned cluster algorithm’s n parameter (see section 2.1) was set to 20. The dataset is split into equally sized ‘training’ and ‘testing’ sets; the MVA is trained on the former then applied to the latter as an overtraining check. For a binary classifier, one dataset of voxel variables is designated as ‘signal’ and the other ‘background’, whereas a non-binary classifier is passed a single signal dataset and several background datasets. In each case, the classifier attempts to distinguish signal voxels from background(s) voxels, such that when applied to a new voxel it will be classified correctly as often as is possible from the provided variables and the classifier’s discriminating power. The non-binary classifiers are trained to distinguish the signal set from all the provided backgrounds (i.e. one-vs-all classification). TMVA calculates an optimum cut value on the classifier response, with a response above the cut being considered ‘signal-like’ and below ‘background-like’. The optimum cut corresponds to the point at which the signal efficiency is equal to the background rejection. On the ROC curve, this corresponds to the point with the maximum Youden index [18], defined as signal efficiency + background rejection – 1; i.e. the length of the vertical line between the ROC curve and the 45° line connecting the curve’s ends.

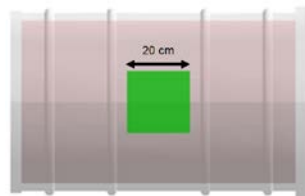


Figure 9. Example simulated geometry used for MVA training: 20 cm side length uranium cube, in the centre of the waste drum.

To check for overtraining, TMVA’s standard check was used: the training signal and background datasets of voxels are both randomly split into two equal groups, with one being used to train the classifier and the other reserved for testing. The trained classifier is then applied to the test set. The classifier output distributions for the training and test sets are then directly compared (see figure 10), with a close match between the distributions indicating a low degree of overtraining. A Kolmogorov-Smirnov test is also performed to quantify the similarity of the distributions. In our case, the distributions of the test and training MVA outputs are a close match visually. The Kolmogorov-Smirnov test value is low however, indicating some degree of overtraining has taken place.

3.3 Momentum information

To determine the importance of momentum information for material classification, two alternative approaches to the muon momentum were investigated in addition to the 50% Gaussian smeared truth momentum described in 2.1. These were using the Monte Carlo truth momentum itself,

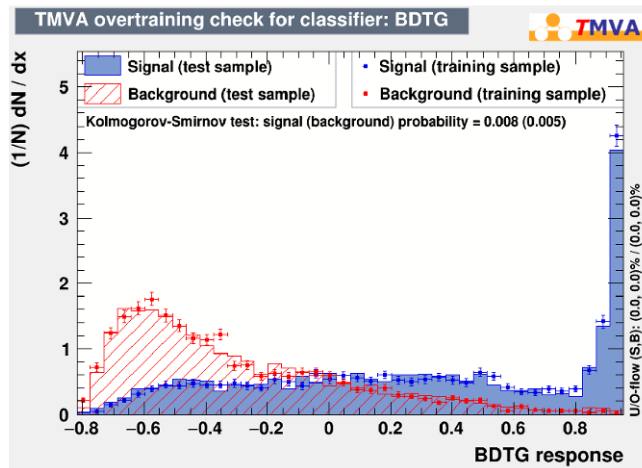


Figure 10. TMVA overtraining check plot for the uranium-lead binary MVA classifier. The MVA output distributions for the signal and background training sets are overlaid with the output distributions for the test sets for comparison and a Kolmogorov-Smirnov test is performed.

with no smearing, and fixing the measured muon momentum at a constant value of 3 GeV/c, i.e. removing momentum information entirely. A comparison of binned clustering algorithm output images of a drum containing 15 cm cubes of uranium, lead and iron for the different approaches is shown in figure 11. Using the Monte Carlo truth momentum results in a slightly sharper image with less variation in the concrete background, whereas using fixed momentum significantly reduces the quality of the image with the iron cube in particular difficult to distinguish from the concrete background.

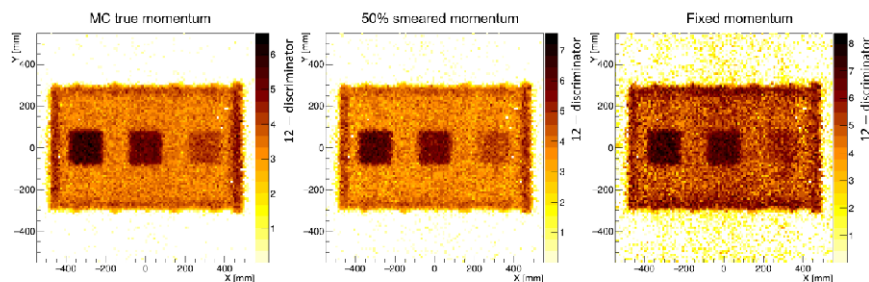


Figure 11. GHSlices from binned clustering algorithm output images (with the algorithm's discriminator value subtracted from 12) of a waste drum containing 15 cm side length cubes of uranium, lead and iron, with three different muon momentum approaches: using the Monte Carlo truth momentum (left), applying a 50% Gaussian smear to the truth momentum (centre), and removing momentum information entirely by fixing it at a constant value (right). Exposure time = 10 days, $\tau = 5$.

2021 JINST 16 P05007

To quantify the effect on material discrimination, binary uranium-lead MVA classifiers trained as described in section 3.2 but with samples obtained using the three different momentum approaches were used to create ROC curves for each scenario (figure 12). Comparing the AUC for each case shows that smearing the momentum slightly reduces the discriminating power of the classifier, with AUC = 0.852 for the truth momentum and AUC = 0.811 for the 50% smeared momentum. The fixed momentum classifier has significantly worse performance with AUC = 0.631. The implication is that momentum information is important for this ‘local’ i.e. voxel-scale approach to material discrimination, but that a smeared momentum approach gives comparable performance to the idealised Monte Carlo truth.

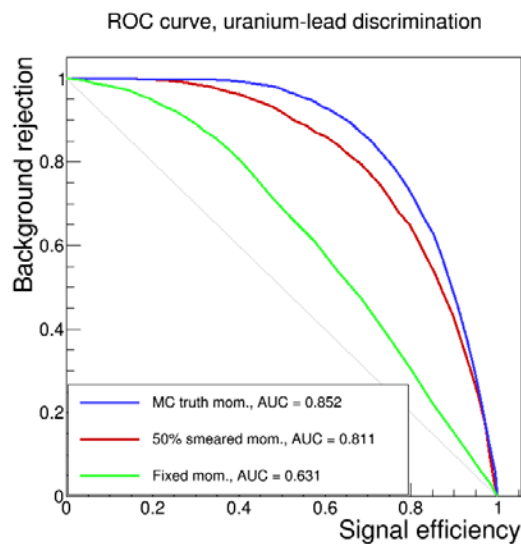


Figure 12. Comparison of ROC curves and their AUCs for the three momentum approaches (Monte Carlo truth momentum, 50% Gaussian smeared truth momentum, and fixed momentum). The MVA classifier trained to discriminate uranium and lead voxels from samples taken from drums containing 20 cm cubes, with exposure time 10 days. Smearing the momentum reduces the discriminating power by a small degree, removing momentum information greatly reduces discriminating power.

4 Identifying stored bodies

4.1 Removal of concrete background

It is necessary to attempt to remove the voxels corresponding to the concrete background and steel shell from the binned clustering algorithm output image. The remaining voxels, corresponding to stored objects, can then be sorted into distinct clusters using the algorithm described in section 4.2. The non-binary concrete classifier’s training outputs and ROC curves are shown in figure 13.

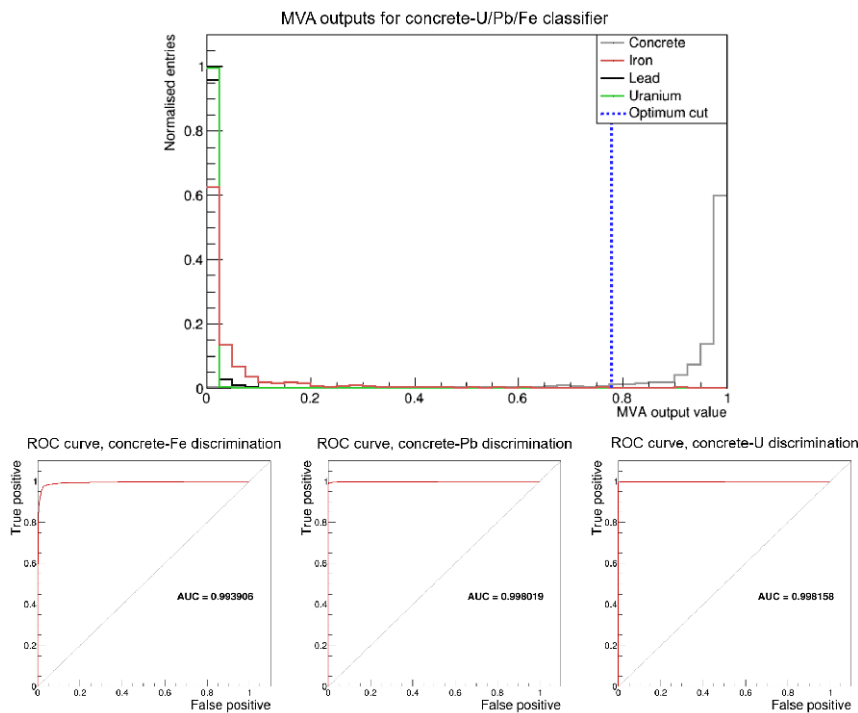
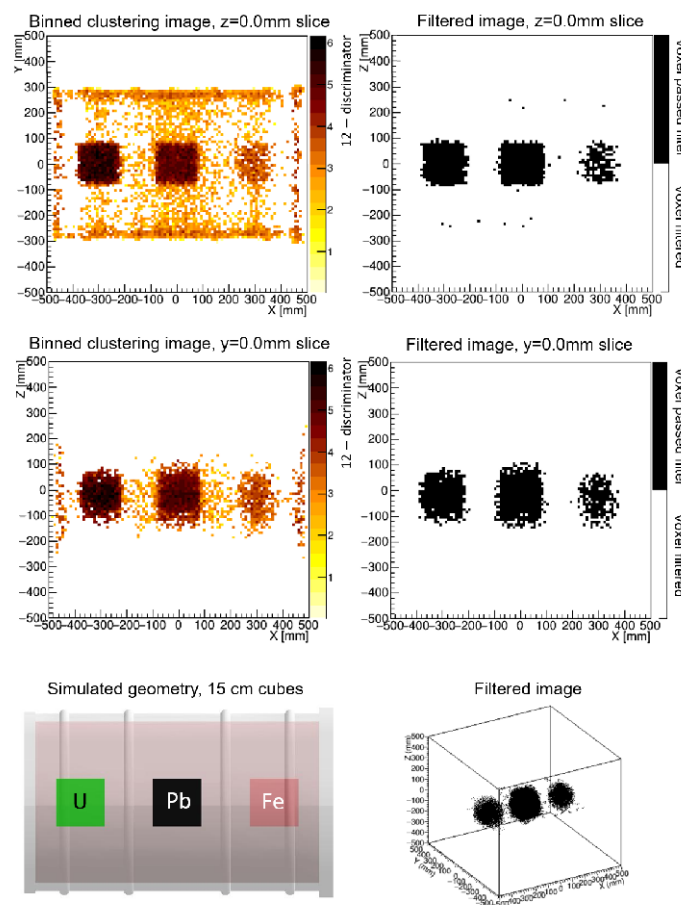


Figure 13. MVA training outputs (top) and ROC curves (bottom) for concrete vs iron/lead/uranium non-binary classifier. The optimum cut (blue) corresponds to the point at which signal efficiency is equal to background rejection.

As the dimensions of the drum are known, the steel outer shell voxels can be removed trivially through a cylindrical spatial cut on the image. Subsequently an MVA classifier trained as described in section 3, designating the dataset of concrete voxels as ‘signal’ and the other materials as ‘backgrounds’, is applied to the remaining voxels to filter out the concrete voxels. As the classifier is not perfect, some voxels that correspond to concrete in the original simulated geometry remain in the filtered image. The problem is partially mitigated by applying a simple filtering algorithm to remove ‘isolated’ voxels from the image. Each remaining voxel has its 6 nearest neighbour voxels checked; if they are all empty, the voxel is removed from the image. figure 14 illustrates the result of applying this process to a simulated geometry of three 15 cm cubes. The removed voxels are coloured white in the images; the remaining voxels are black. To test the performance of the nearest neighbour filtering method, the false positive and false negative rates were calculated for this example. Defining a false positive as voxel that does not correspond to concrete being filtered out, and a false negative as a voxel that does correspond to concrete passing the filter, the false positive rate was $0.014^{+0.008}_{-0.005}$ and the false negative rate was 0.497 ± 0.008 . The low false positive

2021 JINST 16 P05007

rate indicates that very few non-concrete voxels are being incorrectly filtered out. The high false negative rate however indicates that a large number of concrete voxels remain in the final image; this corresponds to the smearing in the *z* direction of objects in the drum visible in figure 3.



2021 JINST 16 P05007

Figure 14. Illustrative example of MVA-filtering algorithm applied to a simulated geometry of a drum containing 15 cm cubes of uranium, lead and iron. Voxels passing the MVA filtering process described above are coloured black.

4.2 Clustering

Subsequently these identified and separated ‘object’ voxels need to be grouped into individual clusters, each corresponding to a body stored in the drum. This will allow material information to be calculated by applying MVA classifiers to each identified body. The clustering is achieved

through the widely used k -means clustering algorithm, which in its simplest form operates as follows:

- Choose a value for the number of clusters, k .
- Pick k randomly selected data points to be the initial cluster centroids.
- For each data point, calculate the Euclidean distance (in geometric space) to each of the centroids and assign the point to the cluster with the closest centroid.
- Calculate new centroids as the new centres of the clusters.
- Repeat until the centroid locations converge.

Though this algorithm is fast and easy to implement, it requires the number of clusters k to be known in advance and used as an input. One solution is to run the algorithm multiple times with range of k values as input, and calculate some figure of merit of the clustering output for each. A commonly used figure of merit for clustering algorithms is the Dunn index [19], defined as the ratio between the minimum inter-cluster distance and the maximum intra-cluster distance. A high Dunn index therefore indicates well-separated and compact clusters. The inter- and intra-cluster distances can be defined to suit the problem; in our case the inter-cluster distance metric is the distance between the closest two data points in the two clusters, and the intra-cluster distance metric is the distance between the two furthest-apart points in a cluster. Defined in this way, the k value that corresponds to the maximum Dunn index will represent the most natural choice for k . In most cases this will correspond to the number of bodies stored in the waste drum. In some cases the algorithm can under-estimate k if e.g. two objects are in contact or very close together.

In practise, the simple k -means algorithm often produces poor clustering solutions if the randomly chosen initial centroids are too close together. This problem is avoided by choosing the first centroid only from a uniform distribution and the subsequent $k - 1$ centroids from a distribution weighted by the squared distances of the data points from the already chosen centroid(s). This form of the algorithm is often referred to as ' k -means++' [20]. Figure 15 shows the result of applying the k -means++ algorithm to a drum containing 15 cm cubes of iron, lead and uranium.

This algorithm occasionally fails when applied to MVA-filtered binned clustering images such as figure 14, as the 'noise' voxels that do not correspond to a stored object can be treated as a new superfluous cluster. These 'fake' clusters are much more sparse than clusters corresponding to stored objects. This allows the problem to be mitigated by defining a cluster density and removing clusters with densities below some cut. We define cluster density as the ratio of the number of voxels in the cluster to the cube of the mean inter-voxel distance. A density cut of 5×10^{-2} voxel cm^{-3} is effective at removing the sparse clusters.

A small percentage of voxels that correspond to concrete in the drum will be incorrectly passed by the classifier and included in the filtered image. These will be incorporated into one of the clusters, which could cause an incorrect material decision. These voxels will be outliers in the cluster as the majority of the cluster voxels will be close to the cluster centroid; thus they can be filtered out by placing a cut on the distribution of voxel-centroid distances for each cluster. Choosing the cut so as to remove voxels for which the voxel-centroid distance is greater than one standard deviation from the mean of this distribution is effective at removing outlier voxels.

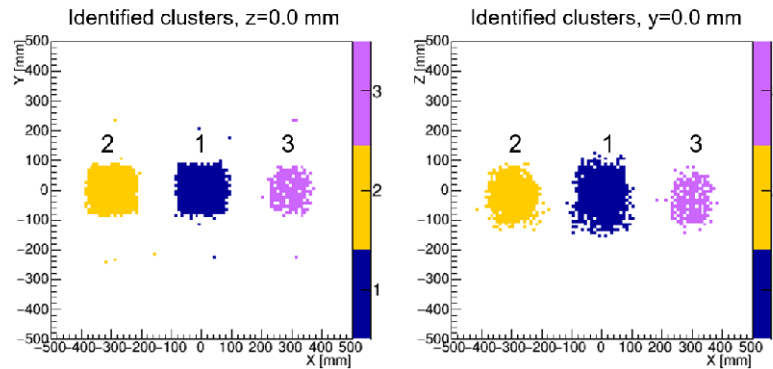


Figure 15. GH (left) and G (right) slices of the clustering solution for a simulated waste drum containing three 15cm cubes of different materials. The voxels separated by the method described in section 4.1 have been grouped into three clusters using the k -means++ clustering algorithm.

Finally, a filter is applied to remove approximately the outermost voxel layer (see figure 16) from the surface of each cluster. This is necessary as in general there will be a degree of smearing between a stored body and the concrete background, due to scattering vertices from muons passing close to the object contributing to the algorithm's metric values (see section 2.1) and hence affecting the variables that are passed to the MVA classifiers. The filtering is achieved by calculating the mean of the centroid-voxel distances for each cluster, and removing voxels for which the distance is greater than the mean.

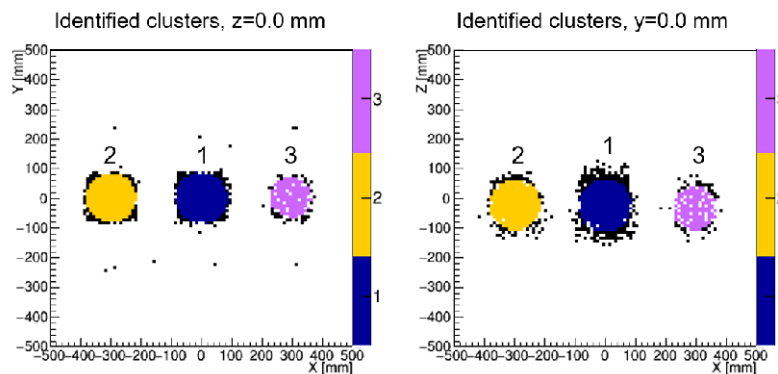


Figure 16. GH (left) and G (right) slices of the clustering solution of figure 15 after filtering the outermost voxels from each object. Here black indicates voxels removed from the cluster.

2021 JINST 16 P05007

5 Results and analysis

5.1 Applying MVAs to clustered objects

Further MVA classifiers are now applied to the voxels in each identified cluster to obtain material information for the bodies stored in the drum. Two additional MVA classifiers are trained: a non-binary classifier that separates iron signal from lead and uranium backgrounds (see figure 17), and a final binary classifier to discriminate lead and uranium (figure 18). The training ROC AUCs for these classifiers show that the lead and uranium cases are easily distinguished from iron (as the AUC values are close to 1), whereas the lead/uranium classifier does not perform as well, due to the similarity of the materials' / values.

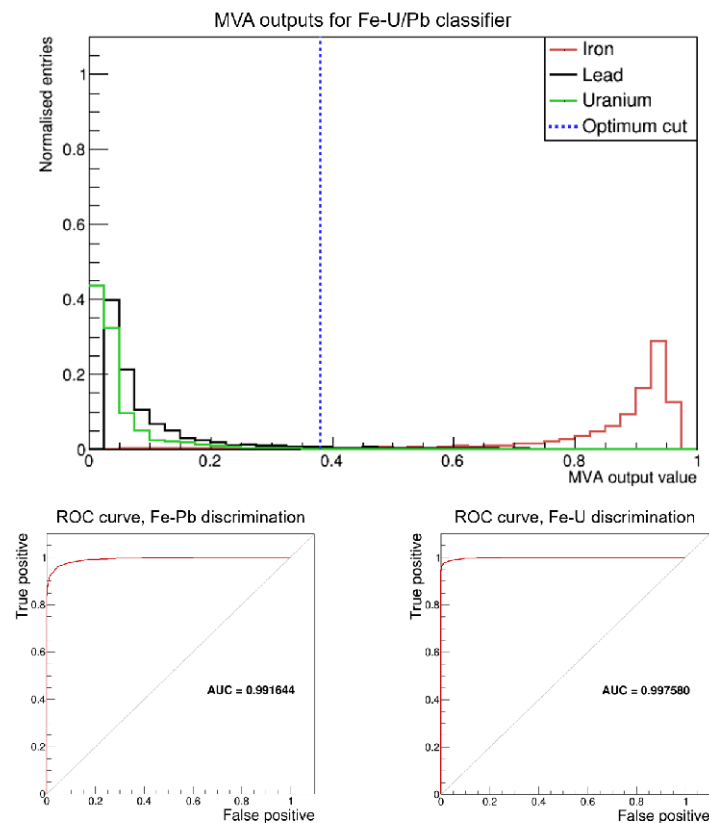


Figure 17. MVA training output and ROC curves for iron/lead/uranium non-binary classifier. The optimum cut corresponds to the point at which signal efficiency is equal to background rejection.

2021 JINST 16 P05007

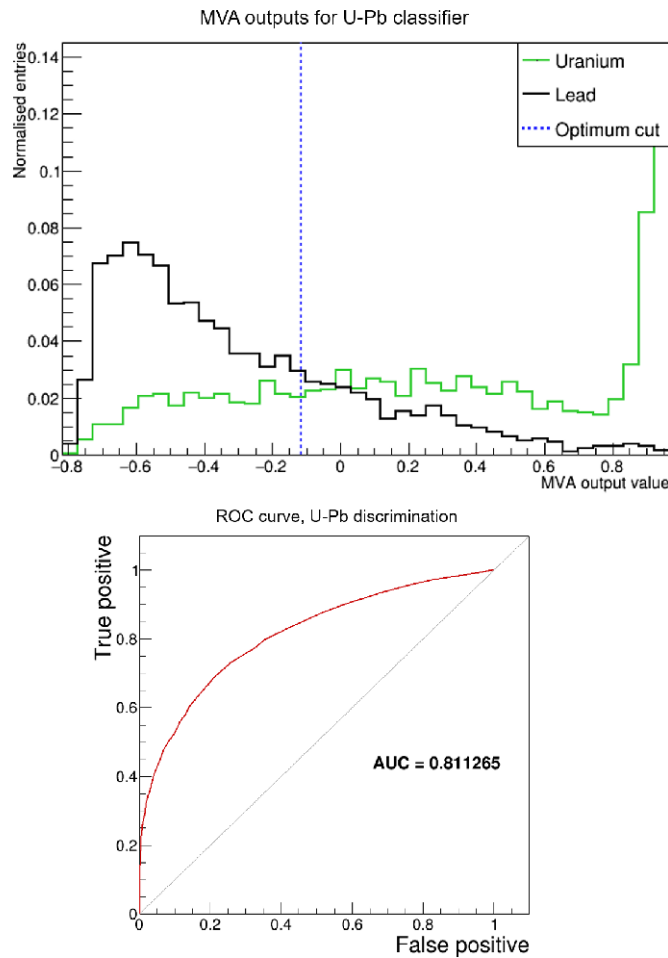
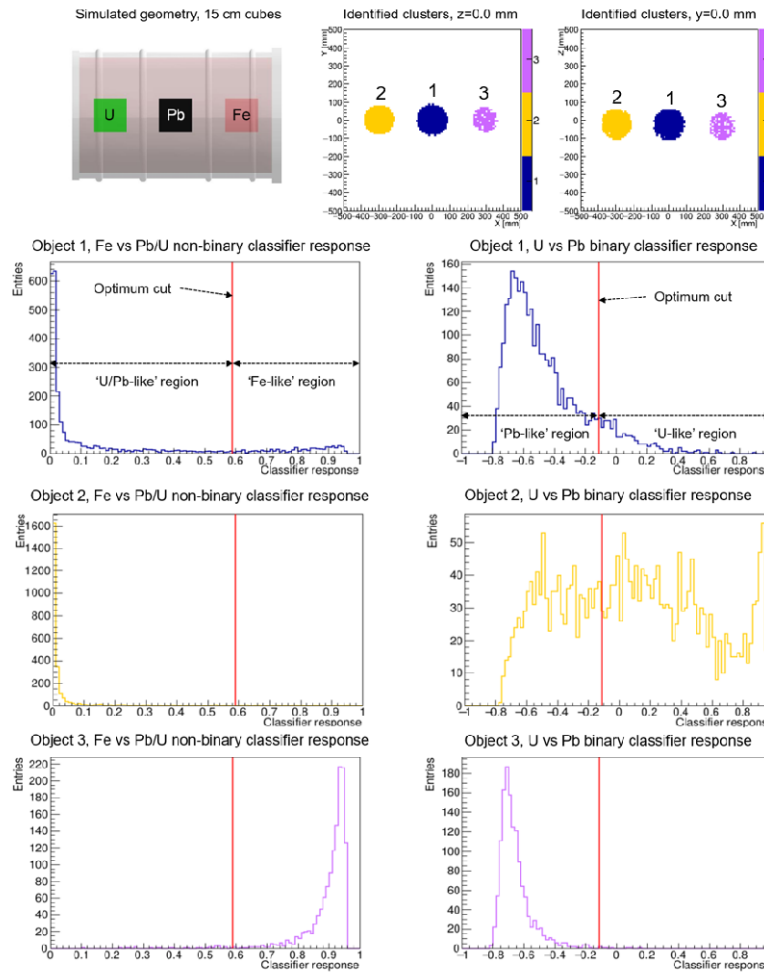


Figure 18. MVA training output and ROC curves for lead/uranium binary classifier. The optimum cut corresponds to the point at which signal efficiency is equal to background rejection.

Each MVA classifier will produce a single response value for each voxel it is applied to. If the value falls above the cut (see section 3.2), the voxel will be considered signal-like, and if it falls below, background-like. Each identified object is a set of voxels, we apply the classifiers to each voxel to obtain the object's distributions of response values, then calculate the proportions of response values that fall above the cuts (i.e. the proportion of the object's voxels that are signal-like) to arrive at a single value from each classifier for each object. Figure 19 shows the MVA classifier response distributions for the three identified objects in the 15 cm cube example simulated geometry.



2021 JINST 16 P05007

Figure 19. Distributions of responses of MVA classifiers applied to found clusters from a simulated waste drum containing 15 cm cubes of uranium (object 2), lead (object 1) and iron (object 3). The optimum cuts for the classifiers correspond to the points at which the signal efficiency is equal to background rejection.

5.2 Obtaining material decisions

Applying the integral method described above to these distributions results in uranium, lead and iron 'material scores' for each object stored in the drum. The uranium and lead material scores are subsequently multiplied by 1 – iron score, i.e. the 'not-iron' score. These scores are very effective at distinguishing objects of different materials once the sizes of the objects are taken into account. The material scores are intuitively viewed as a pie chart (see figure 20). For the simulated drum contain-

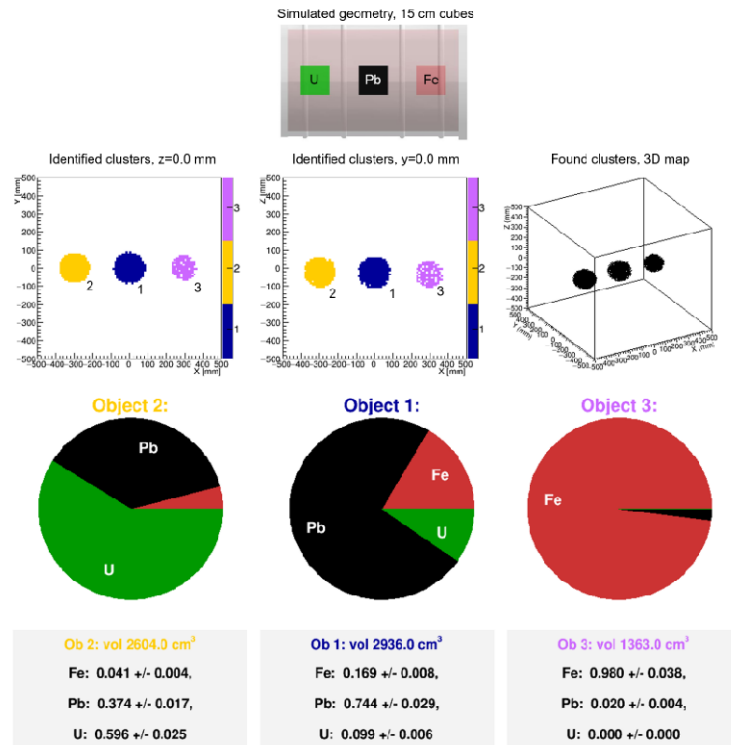


Figure 20. Material scores for simple geometry of three 15cm cubes, uranium, lead and iron, aligned with voxel grid.

ing three 15cm sidelength cubes of uranium, lead and iron, each object has the MVA-calculated material score that corresponds to the true material as the largest score. The scores for the uranium and lead blocks are also clearly distinguished from each other. However, this simulation is an idealised case due to the large size of the objects and their similarity to the 20 cm cube training geometries.

Applying the MVA classifiers to a similar but more challenging geometry of three 10 cm side length cubes (see figure 21), two effects become apparent. Firstly, the classifiers do not perform as well i.e. the score corresponding to the true material is not necessarily the largest. For example, the 'uranium' score has reduced from 0.596 ± 0.025 for the 15 cm cube case to 0.221 ± 0.025 . However, the uranium score for the lead cube has also reduced, by a comparable factor. This effect can be explained by considering the repeated scatterings of muons in a large high- Z object: a larger object will lead to larger detected muon scattering angles, and hence a smaller binned clustering metric value (see 2.1). Hence a large lead object can appear more 'uranium-like' than a smaller lead object. The implication is that the size of stored objects must be taken into account to reliably determine their material composition.

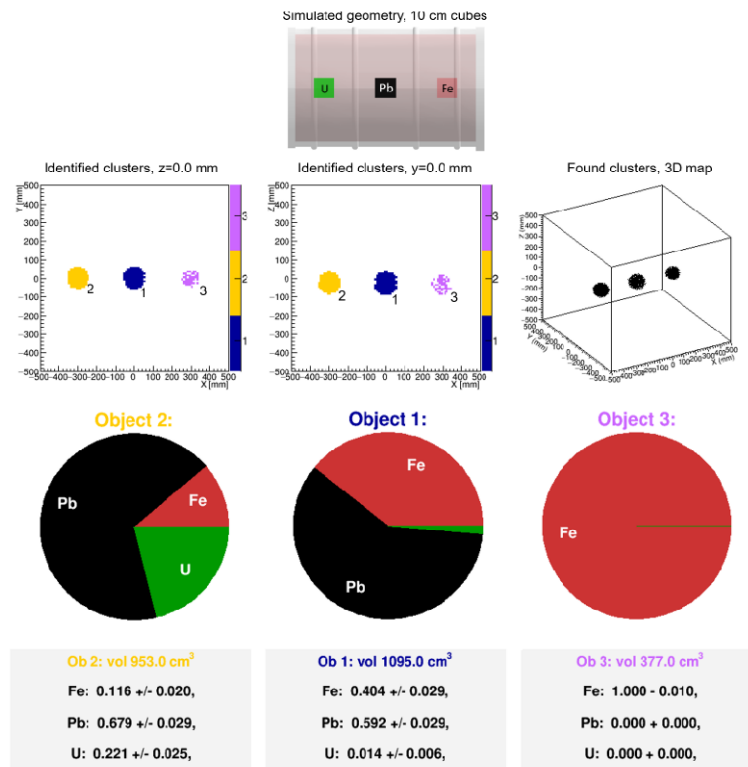
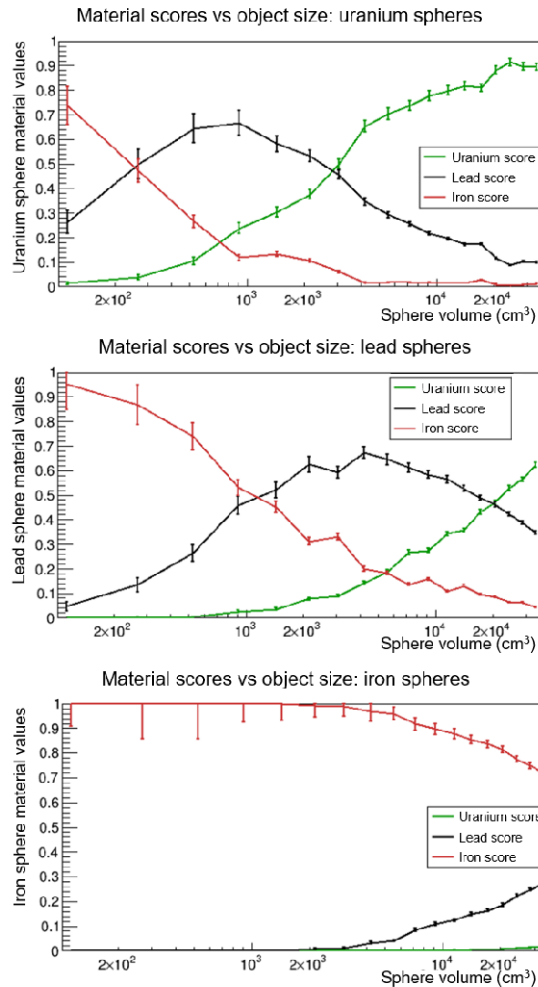


Figure 21. Material estimate results for simple geometry of three 10cm cubes, uranium, lead and iron, aligned with voxel grid.

To quantify the relations between the object size and the material scores, we applied our system to a series of simulated drums containing spheres of different materials and increasing radii. The results are shown in figure 22. It is apparent that whilst there is no simple relation between the material scores and the object volume, objects of different material are clearly distinguished for a wide range of volumes.

However, these plots can be used empirically to arrive at a single decision material for each identified stored body in the drum. As the volumes of the clusters (equivalent to the number of constituent voxels) are known, the plots in figure 22 give the 'expected' material scores for a cluster of that size if the object was composed of one of the three materials. Finally, a material decision is arrived at by comparing the object's actual material scores with each set of expected values. The material with the best match, i.e. the minimal 3D Euclidean norm between the actual and expected material scores, is selected as the final material decision.



2021 JINST 16 P05007

Figure 22. Relationship between the MVA-calculated material scores and the size of the stored object. Each simulated geometry contains a single sphere of increasing radii, composed of uranium (top), lead (middle) or iron (bottom).

This approach was tested on more complex simulated geometries. Figure 23 shows results for a drum similar to the three-cube example of figure 20, but with objects of irregular size, location and rotation. In this case the system has accurately identified the correct material for each object. Despite the uranium block's low uranium score compared to the equivalent 15 cm cube (figure 20), the calibration by volume has correctly identified it as uranium.

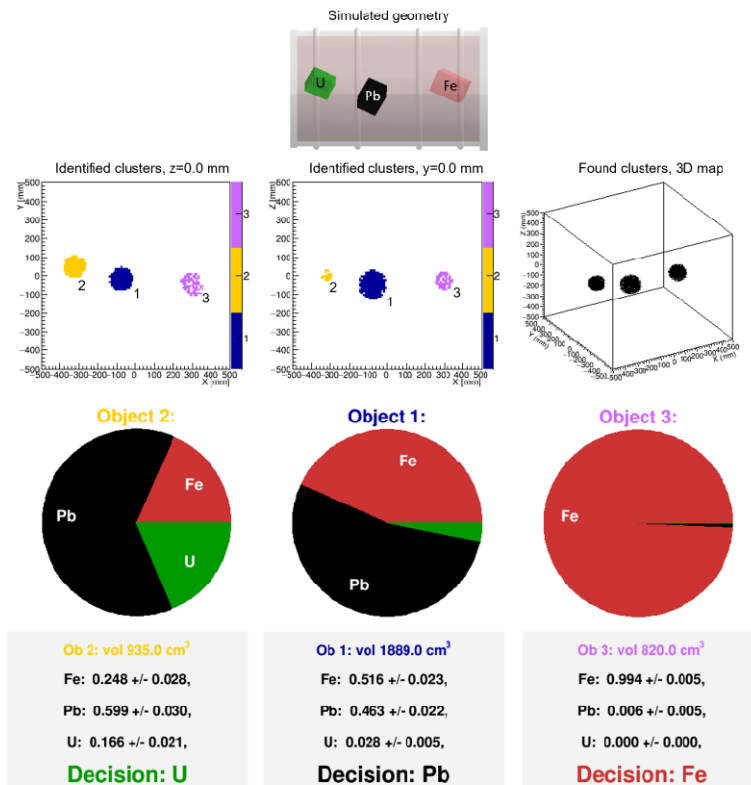


Figure 23. Material estimate results for more complex geometry of three objects, uranium, lead and iron, not aligned with the voxel grid or centred. By calibrating the three material scores against the volume calibration curves, (figure 22), the correct material has been assigned in each case.

A further example with a larger number of objects is shown in figure 24. This drum contains five objects (two uranium, two lead, and one iron) of a wider range of shapes, dispersed more evenly through the drum. However, the system still performs well. The identified clusters are a close match to the true locations of the stored objects. Both uranium objects are correctly assigned, as is the iron sphere and one of the lead objects. One lead object, a tube, has been incorrectly identified as iron. This indicates a limitation of the system when attempting to determine the materials of non-spherical objects.

5.3 Sensitivity

To establish the system's sensitivity and false positive rate, we then applied it to a set of randomly generated waste drum simulations. Each simulation contained three spheres of radius 6 cm, randomly dispersed throughout the drum but constrained to not intersect each other. 100 simulations

2021 JINST 16 P05007

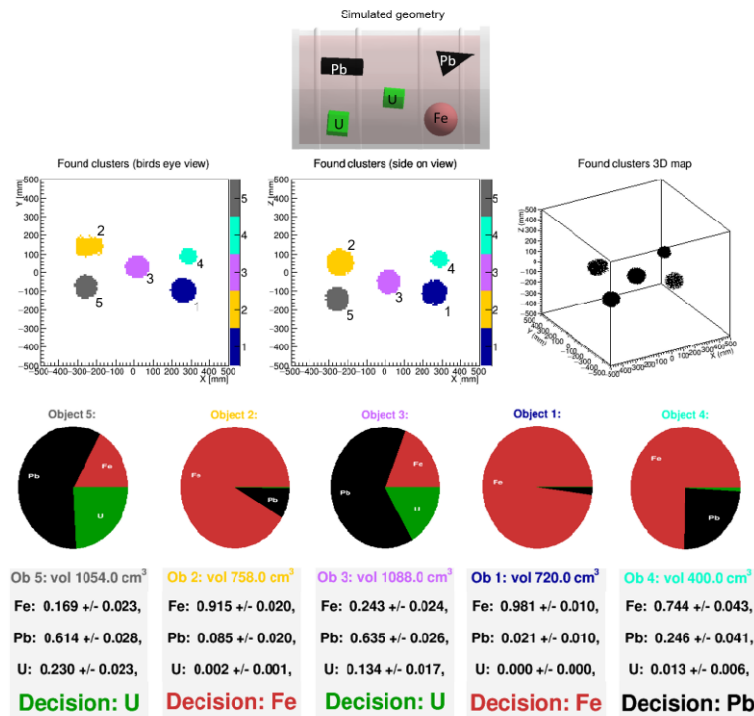


Figure 24. Material estimate results for more complex geometry of five objects of various materials and shapes, dispersed throughout the drum. Note that the 2D cluster plots are viewed as side-on and bird's eye views of the 3D map; this is necessary to view all the clusters as they do not all intersect the central *G* and *I* planes. Four of the objects have been assigned the correct material; one lead object has been incorrectly classified as iron.

were run in total. 50 simulations contained one uranium, one lead and one iron sphere, and the remaining 50 contained two lead spheres and one iron sphere. A true positive identification of a uranium object was defined to be an object identified close to the true location of a uranium sphere that was designated as uranium by the system. Conversely a false positive comprised any assignment of a uranium decision to an object in a drum not containing uranium. With these criteria, we found a sensitivity of $0.90^{+0.07}_{-0.12}$, and a false positive rate of $0.12^{+0.12}_{-0.07}$ (95% Clopper-Pearson confidence intervals).

6 Conclusions

We have demonstrated that machine learning techniques are a powerful tool for enhancing the information about a waste drum's contents that can be obtained in a muon scattering tomography experiment. MVA classifiers trained on variables obtained from the distribution of binned clustering

2021 JINST 16 P05007

algorithm metric values are effective at discriminating materials in waste drums. The concrete matrix can be distinguished from stored objects of mid- and high-Z material, allowing the voxels corresponding to the matrix to be removed, and the remaining object voxels sorted into clusters.

Additional material information can be obtained with further MVA classifiers, to discriminate first mid-Z (e.g. iron) from high-Z (lead, uranium) objects, and then between materials with similar Z. The effectiveness of the material discrimination is highly dependent on object size. By establishing the empirical relation between object size and the MVA classifiers' material output scores, a final material decision can be made for each identified stored body in the simulated waste drum. This has shown to be accurate for a wide range of object sizes, shapes and drum locations.

When tested against a set of simulated drums containing 6 cm radius spheres of different materials in randomly determined positions, the system performed with a true positive rate of $0.90^{+0.07}_{-0.12}$, and a false positive rate of $0.12^{+0.12}_{-0.07}$, indicating this approach is effective at identifying uranium objects inside waste drums. The main identified vulnerabilities are objects with large differences in Z (e.g. iron and uranium) being very close too each other, and more spatially extended objects being misidentified, although the latter problem could be mitigated by extending the object size-based decision method (see figure 22) to account for a wider range of object shapes.

Acknowledgments

This project has received funding from the Euratom research and training programme 2014–2018 under grant agreement No. 755371.

References

- [1] W Kubinski et al., *Calorimetric non-destructive assay of large volume and heterogeneous radioactive waste drums*, *EPJ Web Conf.* **225** (2020) 06003.
- [2] L.J. Schultz et al., *Image reconstruction and material Z discrimination via cosmic ray muon radiography*, *Nucl. Instrum. Meth. A* **519** (2004) 687.
- [3] L. Frazão, J. Velthuis, C. Thomay and C. Steer, *Discrimination of high-Z materials in concrete-filled containers using muon scattering tomography*, *2016 JINST* **11** P07020.
- [4] L. Frazão, J. Velthuis, S. Maddrell-Mander and C. Thomay, *High-resolution imaging of nuclear waste containers with muon scattering tomography*. *2019 JINST* **14** P08005.
- [5] T. Stocki et al., *Machine learning for the cosmic ray inspection and passive tomography project (CRIPT)*, *IEEE Nucl. Sci. Symp. Med. Imag. Conf. Rec.* (2012) 91.
- [6] X.-Y. Pan, Y.-F. Zheng, Z. Zeng, X.-W. Wang and J.-P. Cheng, *Experimental validation of material discrimination ability of muon scattering tomography at the TUMUTY facility*, *Nucl. Sci. Tech.* **30** (2019) 120.
- [7] L.J. Schultz et al., *Statistical reconstruction for cosmic ray muon tomography*, *IEEE Trans. Image Processing* **16** (2007) 1985.
- [8] G.R. Lynch and O.I. Dahl, *Approximations to multiple Coulomb scattering*, *Nucl. Instrum. Meth. B* **58** (1991) 6.
- [9] PARTICLE DATA GROUP collaboration, *Review of particle physics*. *Particle Data Group, Phys. Lett. B* **592** (2004) 1.

2021 JINST 16 P05007

- [10] S. Riggi et al., *Muon tomography imaging algorithms for nuclear threat detection inside large volume containers with the Muon Portal detector*, *Nucl. Instrum. Meth. A* **728** (2013) 59 [arXiv:1307.0714].
- [11] C. Thomay et al., *A binned clustering algorithm to detect high-Z material using cosmic muons*, 2013 *JINST* **8** P10013.
- [12] C.L. Morris et al., *Tomographic imaging with cosmic ray muons*, *Sci. Global. Secur.* **16** (2008) 37.
- [13] C. Steer, P. Stowell and L. Thompson, *CRESTA: Cosmic rays for engineering, scientific, and technology applications*, <https://gitlab.com/cosmicraysim/cresta>.
- [14] GEANT4 collaboration, *GEANT4 — a simulation toolkit*, *Nucl. Instrum. Meth. A* **506** (2003) 250.
- [15] C. Haggmann, D. Lange and D. Wright, *Cosmic-ray shower generator (CRY) for Monte Carlo transport codes*, *IEEE Nucl. Sci. Symp. Conf. Rec.* **2** (2007) 1143.
- [16] H. Voss, A. Hocker, J. Stelzer and F. Tegenfeldt, *TMVA, the Toolkit for Multivariate Data Analysis with ROOT*, *PoS ACAT* (2007) 040.
- [17] R. Brun and F. Rademakers, *ROOT: An object oriented data analysis framework*, *Nucl. Instrum. Meth. A* **389** (1997) 81.
- [18] W.J. Youden, *Index for rating diagnostic tests*, *Cancer* **3** (1950) 32.
- [19] J.C. Dunn, *A fuzzy relative of the isodata process and its use in detecting compact well-separated clusters*, *J. Cybern.* **3** (1973) 32.
- [20] D. Arthur and S. Vassilvitskii, *k-means++: The advantages of careful seeding*. <http://ilpubs.stanford.edu:8090/778/>, June 2006.

2021 JINST 16 P05007



9.6 Initial study for Zwilag



Zwilag project



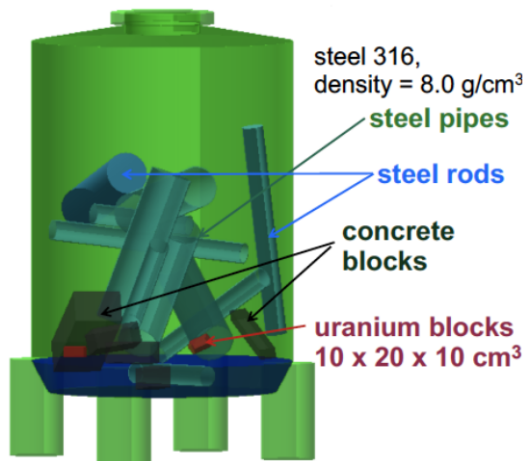
Dr. Jaap Velthuis

🔥 Outline

- ◆ Highlights of our brief Monte Carlo study
- ◆ Current and recent work
- ◆ Proposed project
- ◆ Thoughts on first phase

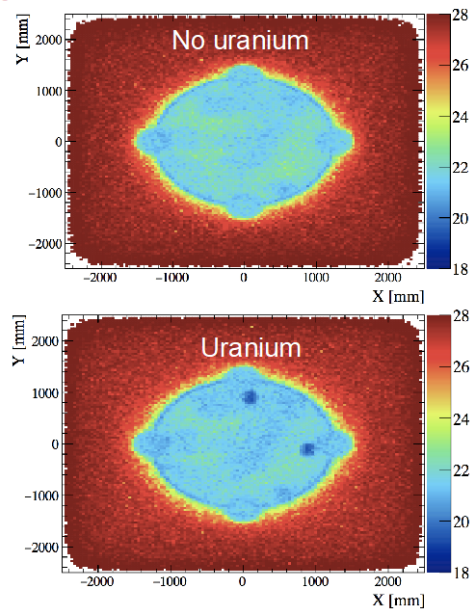
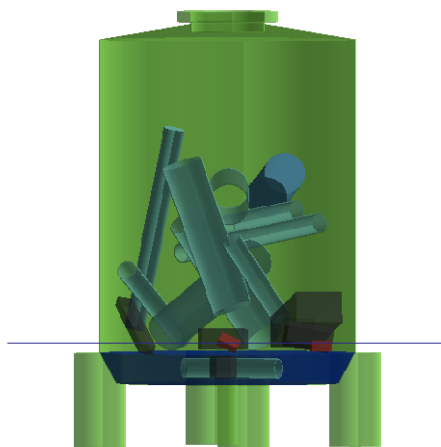
🔥 Highlights simulation study

- ◆ Simulated container 5a
 - placed 5m x 5m detectors above and below cask
 - ~3 months worth of muon
 - no optimization done yet for actual deployment
 - used large U blocks, steel pipes and rods



🔥 Highlights simulation study

- ◆ Have our own metric variable.
- ◆ Slice through uranium blocks shows uranium blocks clearly.



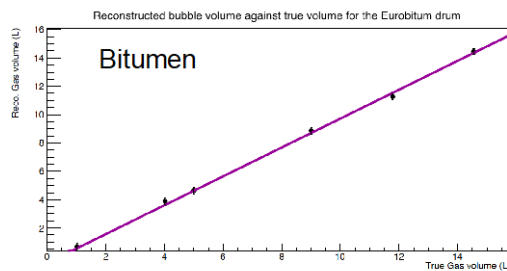
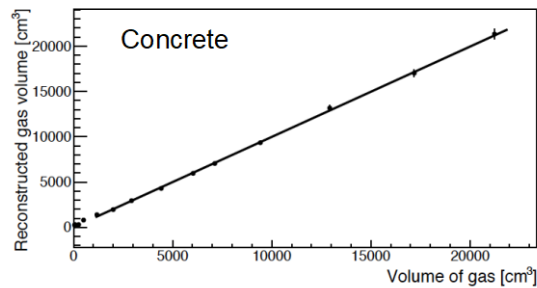
🔦 Highlights simulation study

- ◆ Very first studies, not fully optimized for this case
 - Can distinguish uranium blocks from other content by eye
- ◆ No quantitative analysis done yet, also depends on what the goal is:
 - locate uranium?
 - measure amount of uranium?
 - exclude uranium?



🔦 Current and recent work

- ◆ Have focused so far on smaller drums (400L)
- ◆ Can detect gas bubbles in concrete and Eurobitum.

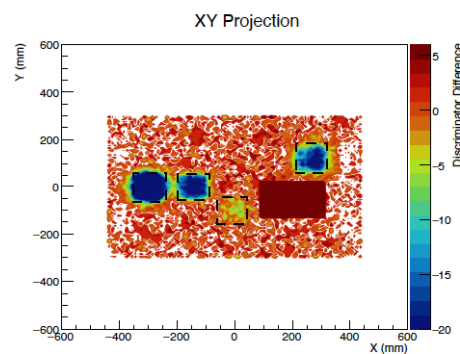
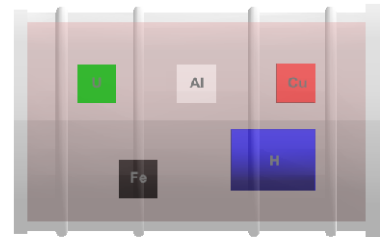


M. Dobrowolska et al 2018 JINST 13 P05015



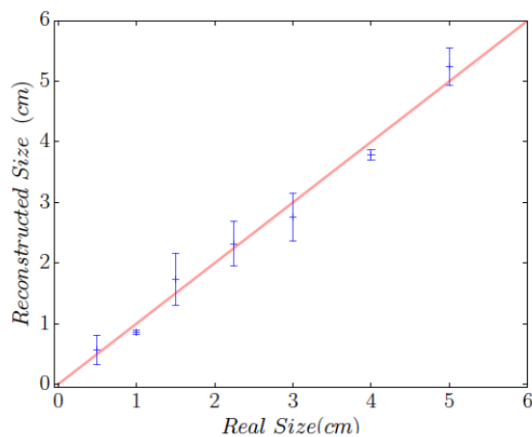
🔦 Current and recent work

- ◆ Have focused so far on smaller drums (400L)
- ◆ Can detect gas bubbles in concrete and Eurobitum.
- ◆ Developed techniques to measure sizes of gas bubbles even when located next to lumps of Uranium.



🔦 Current and recent work

- ◆ Have focused so far on smaller drums (400L)
- ◆ Can detect gas bubbles in concrete and Eurobitum.
- ◆ Developed techniques to measure sizes of gas bubbles even when located next to lumps of Uranium.
- ◆ Measured the size of cubes of uranium

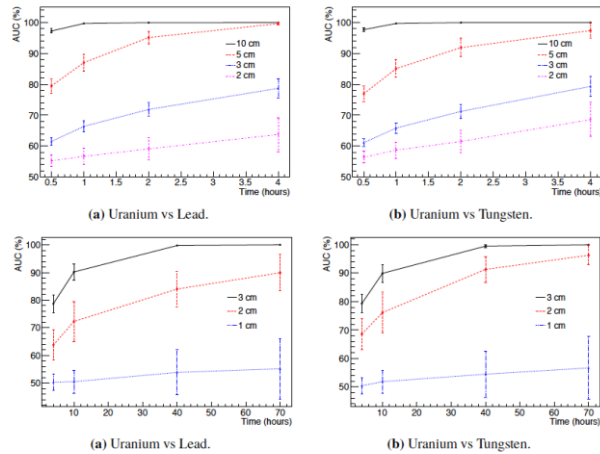


L. Frazão et al 2019 JINST 14 P08005



🔥 Current and recent work

- ◆ Have focused so far on smaller drums (400L)
- ◆ Can detect gas bubbles in concrete and Eurobitum.
- ◆ Developed techniques to measure sizes of gas bubbles even when located next to lumps of Uranium.
- ◆ Measured the size of cubes of uranium
- ◆ Discriminate between materials

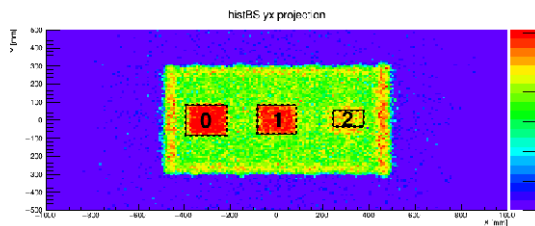
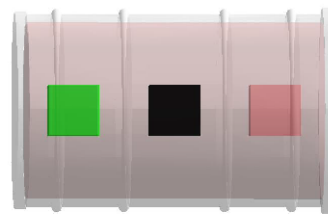


L. Frazão et al 2016 JINST 11 P07020



🔥 Current and recent work

- ◆ Have focused so far on smaller drums (500L)
- ◆ Can detect gas bubbles in concrete and Eurobitum.
- ◆ Developed techniques to measure sizes of gas bubbles even when located next to lumps of Uranium.
- ◆ Measured the size of cubes of uranium
- ◆ Discriminate between materials
 - Using machine learning



Block	Conc	Fe	Pb	U
0	0	6	29	66
1	0	18	57	26
2	0	82	18	1



✦ Lucens project

- ◆ We have good analysis techniques and a detector system for tomography with 500L drums.
- ◆ We know that the techniques work for the large Lucens containers in principle.
- ◆ We do not yet know how the small drum results translate to the large Lucens containers.
 - larger distance between detector planes (located above and below the containers) reduces the angular resolution
 - can we (afford to) build a 5x5m² detector system or a smaller system that is moved around
 - required measurement time is not linear
- ◆ We do not yet know the relevant questions in a way that we can evaluate.



✦ Project outline

- ◆ Phase 1:
 - Monte Carlo study to better address the experimental questions and run some realistic deployment scenarios.
- ◆ Phase 2a - pre-deployment
 - Ordering and further MC
 - Manufacture and qualification tests
- ◆ Phase 2b - deployment on site
 - Installation and qualification
- ◆ Phase 3 - data taking and analysis



🔥 Phase I

- ◆ In order to study what we can achieve we need to do Monte Carlo simulations. Quality of the information depends on
 - data taking time
 - detector size
 - deployment scenario, i.e. detector placement and spacing

- ◆ For simulation study two options
 - hiring a currently employed person. Have a somebody available from Oct 1st 2020. Depending on details takes 6-8 months.
 - hiring a new person. Earliest estimated start date May 1st. Depending on details takes 12 months.

9.7 A proposal for muon tomography proof-of-principle projects at the Grimsel Test Site

A proposal for muon tomography proof-of-principle projects at the Grimsel Test Site

L.F. Thompson^{1,2}, K. Aymanns³, D. Garbutt⁴, E. Holme⁴, A. Liebscher⁶, A. Martin⁵,
I. Niemeyer³, C. Vieh⁶, M. Weekes¹.

- 1 Department of Physics and Astronomy, University of Sheffield, Sheffield, S3 7RH, UK.
2 Geoptic Infrastructure Investigations, Pickaxe Lane, South Warnborough, RG29 1SD, UK.
3 Forschungszentrum Jülich GmbH, IEK-6: Nuclear Waste Management, Wilhelm-Johnen Strasse, 52425 Jülich, Germany.
4 Nuclear Waste Services, Nuclear Decommissioning Authority, Building 329, Thomson Avenue, Harwell Campus, Didcot, Oxfordshire, OX11 0GD, UK.
5 Nationale Genossenschaft für die Lagerung radioaktiver Abfälle (NAGRA), Hardstrasse 73, 5430 Wettingen, Switzerland.
6 Bundesgesellschaft für Endlagerung mbH (BGE), Eschenstraße 55, 31224 Peine, Germany.

Abstract

This document describes the muon tomography technique and discusses the potential for the technique to address issues around safety and safeguards during the process of the disposal of nuclear waste in geological disposal facilities (GDFs). A number of potential proof-of-principle projects are proposed for deployment at the Grimsel Test Site in Switzerland.

Introduction

Muon radiography (also known as “muography”) is a powerful technique that employs naturally occurring radiation, specifically cosmic ray muons. Muons are fundamental particles that are benefit from being both abundant (1 per cm² per minute at sea level) and highly penetrating. These properties make them ideal for exploitation, via a technique analogous to a medical X-ray, to locate, identify and measure density irregularities in geological overburdens. Muon radiography benefits from being non-invasive, non-destructive and leaves no residual activation of any nuclear materials. First applied in the 1950s [1], muography is currently undergoing something of a renaissance with a broad and diverse range of applications including imaging civil infrastructure such as railway tunnel imaging [2], identifying ore bodies in mines, monitoring magma chambers in volcanoes [3] and identifying voids in pyramids [4,5].

A further technique, muon scattering tomography, henceforth MST, requires the muons to be tracked both entering and leaving the object of interest. This enables important information on the atomic number, Z, of any objects being imaged to be obtained (in addition to density information). MST has most notably been applied to the imaging of the Fukushima reactor [6].

Safety and Safeguards in Geological Disposal Facilities

The penetrative nature of cosmic ray muons and their natural abundance gives rise to the possibility of applying both muon radiography and muon scattering tomography techniques to detect possible features that may need to be identified for safety or safeguards [7] purposes in geological disposal facilities (GDFs).

The safety of a GDF considers the safe enclosure of radioactive substances; for example, the avoidance, limitation and control of radiation exposure to the operating staff as well as the permanent protection of people and the environment from ionizing radiation and other harmful effects of disposed waste. Furthermore, there are protection goals for disposal of radioactive waste such as to avoid unreasonable burden and obligation for future generations and the safe compliance with sub-criticality.

Safeguards are a set of technical measures applied by the International Atomic Energy Agency (IAEA) on nuclear material and activities, through which the Agency seeks to independently verify that nuclear facilities are not misused and nuclear material not diverted from peaceful uses. States accept these measures through the ratification of safeguards agreements. Under the Euratom Treaty, European Union countries subject their civil nuclear material and facilities also to nuclear safeguards inspections and assurance which is carried out by the European Commission on the behalf of Euratom.

In some instances muon imaging can provide potentially unique information, in other cases data fusion methods, which consider muon imaging alongside other more traditional techniques, may be necessary. A non-exhaustive list of potential areas where muography/MST may provide valuable information to the safety and/or safeguards processes includes:

Safety applications:

- understanding the condition of the host rock and overburden geology of a GDF;
- sensitivity to changes and heterogeneities in the density of the overburden (e.g.: voids, movement or karst formation, water ingress/aquifer);
- confirmation of the disposal canister (DC) emplacement and orientation following backfilling.

Safeguards applications:

- existence of a pre-excavated tunnel near the deposition area;
- construction of a tunnel (or borehole) after deposition;
- substitution of a DC containing spent fuel with one containing dummies;
- design information verification (DIV)¹;
- confirmation of DC emplacement prior to backfilling;
- re-verification of disposal casks post-retrieval.

Safety and safeguards applications:

- continuous geological overburden monitoring for overburden change detection;
- detection of undocumented voiding (e.g.: existence of a (pre-)excavated tunnel near the disposal area);
- checks of backfill integrity in the vaults;
- tunnel lining system checks and monitoring;
- long-term monitoring of the GDF.

¹ Design information includes information on the facility, the nuclear material at the facility and procedures for nuclear material accountancy and control. In this regard “Design information verification” (DIV) activities are carried out by the IAEA at a facility to verify the correctness and completeness of the design information provided by the State. In terms of GDFs a detailed understanding of the geological structure of the site is required, furthermore it needs to be ensured that there are no significant deviations from the facility design during the construction and the operational phase.

It should be stressed that in the GDF application space we expect that muon tomography will often provide complimentary information which can be combined with data from other techniques. As an example of this, muon tomography could be used together with neutron-gamma measurements to scan the deposition tunnel prior to disposal and/or just after placing disposal canisters prior to the completion of the backfilling process. Similarly, muon imaging could be also combined with 3D laser scanning for basic technical characteristics (BTC) verification facilitating random checks that there are no undeclared voids near the declared and 3D-mapped tunnels.

Current work: initial simulations and results

To date, the authors have studied a number of the proposed applications of muon tomography to GDF safety and safeguards via series of simulations which employ large particle physics simulation packages, along with detailed geological information to accurately predict the expected flux of muons that would be observed in a certain, assumed detector or set of detectors. By making certain assumptions, the time taken to observe a particular feature in the object of interest, and the statistical significance of that observation, can be predicted.

In general terms it should be noted that for muon radiography, that whilst the muon flux at the surface is abundant, then the large overburdens expected at an underground GDF site significantly attenuate the muon flux, the result being that either large areas instrumented with detectors and/or long measurement times are required. Furthermore, ideally the detectors should be underneath the object of interest in order to most benefit from the natural properties of the muon flux, i.e. it is at a maximum from the vertical and falls off, approximately as $\cos^2 \theta$, towards the horizontal (where $\theta = 0$ is vertically up). More complete and accurate information on any geological overburden will result in more accurate simulations and hence final images.

A number of preliminary simulation studies have been performed to assess the capability of muography to detect potential features that may need to be identified for safety or safeguards purposes in GDFs. Similarly, the application of MST to the characterisation of materials located inside nuclear waste disposal canisters and to assessing unauthorised diversion scenarios has also been considered. A short summary of results to date is presented. Note, in all examples presented the simulated detector(s) is(are) assumed to have 100% efficiency and perfect angular resolution.

One area of interest is the use of muography to characterise the geological overburden. Here system of five 2 m x 2 m muon detectors deployed under a simple granite slope has been modelled. The 5 detectors are assumed to be located in a tunnel under the slope (see Figure 1 (top)). The resulting data, which effectively measures the “opacity” of the overburden (0% opacity means completely transparent), is measured as a function of incident muon angle and is depicted in Figure 1 (bottom) which clearly shows the change in opacity with detector position as the granite slope increases in thickness. The granite slope can thus be reconstructed using a suitable regression algorithm such as SART - a mathematical technique first used in medical imaging to reconstruct a 3D image from a series of 2D images [8].

Another clear area of concern for a future GDF is understanding of the integrity of the overburden. Muography offers the ability to confirm that the geological integrity of the overburden is as expected and, for example, there are no undocumented voids of considerable size which have the potential to be either a safety issue or suitable for a

diversion scenario. Confidence in the overburden integrity is of interest from both a safety and a safeguards perspective. The application of techniques such as SART, which permit 3D images to be reconstructed from a series of 2D measurements is under investigation to assess the potential of combining images from multiple detection systems to pinpoint features of interest in the overburden. Unphysically large features have been employed in these early stage simulations. Figure 2 (top) indicates the simulated geometry along with, (figure 2 (bottom)), opacity data from 12 different detector positions that clearly indicate that muography is capable of determining both object location and shape information.

Concerning the application of muon scattering tomography to safety and safeguards in nuclear waste disposal, as discussed above, MST returns valuable information on the atomic number of the object(s) being imaged as well as density information. In this respect it is a powerful technique when interrogating DCs. In a study involving the application of machine learning techniques to hidden material identification a two-stage methodology has been developed that first identifies and groups together materials in a concrete matrix and then assigns probabilities to those materials using multivariate analysis techniques [9]. The geometry under investigation, namely a DC filled with concrete with 3 objects of different materials and sizes is illustrated in Figure 3 (top). From left to right the materials and sizes (in cm) are: Uranium: 10x8x12, Lead: 12x12x10 and Iron: 15x11x16. Figure 3 (centre) shows the output from the first stage of the simulation where material boundaries have been determined and objects with densities different to the host matrix have been clearly identified. The MST information for the voxels associated with those differentiated objects are attributed a material identification probability using a machine learning methodology that has previously been trained on those materials (Figure 3 (bottom)).

Finally, a further study using MST has been performed to assess the suitability of the technique to the potential risk of materials diversion. A detailed model of a CASTOR V/52 type storage DC has been developed and various diversion scenarios considered. Figure 4 (left) illustrates the package that has been simulated with modifications applied to four of the 52 baskets, specifically: (1) completely empty basket, (2) a half-loaded basket (side fuel assemblies unloaded), (3) a half-loaded basket (central fuel assemblies unloaded) and (4) a basket where the UO₂ pellets have been replaced with Pb pellets. Figure 4 (right) shows the resulting image from a study using MST assuming detectors have been deployed at either side of the DC. Diversion scenarios (1), (2) and (3) are all very clearly identified, whilst scenario (4), where UO₂ pellets have been replaced with Pb pellets, is not visible.

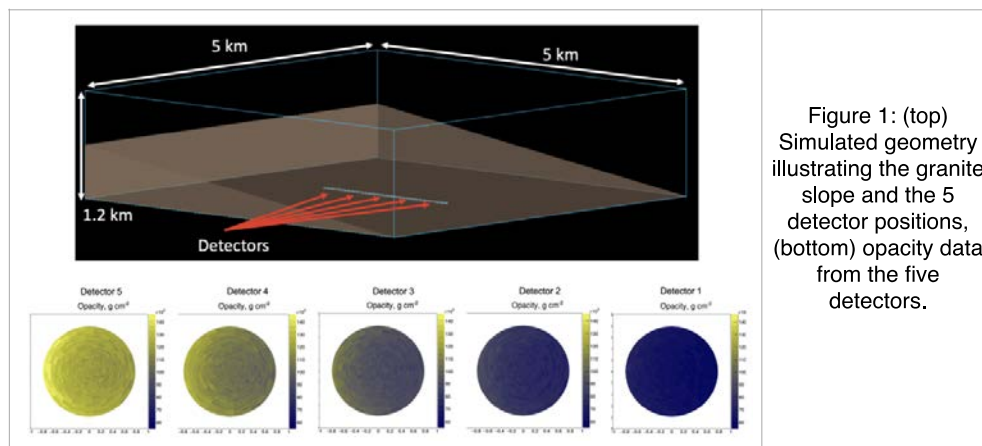


Figure 1: (top) Simulated geometry illustrating the granite slope and the 5 detector positions, (bottom) opacity data from the five detectors.

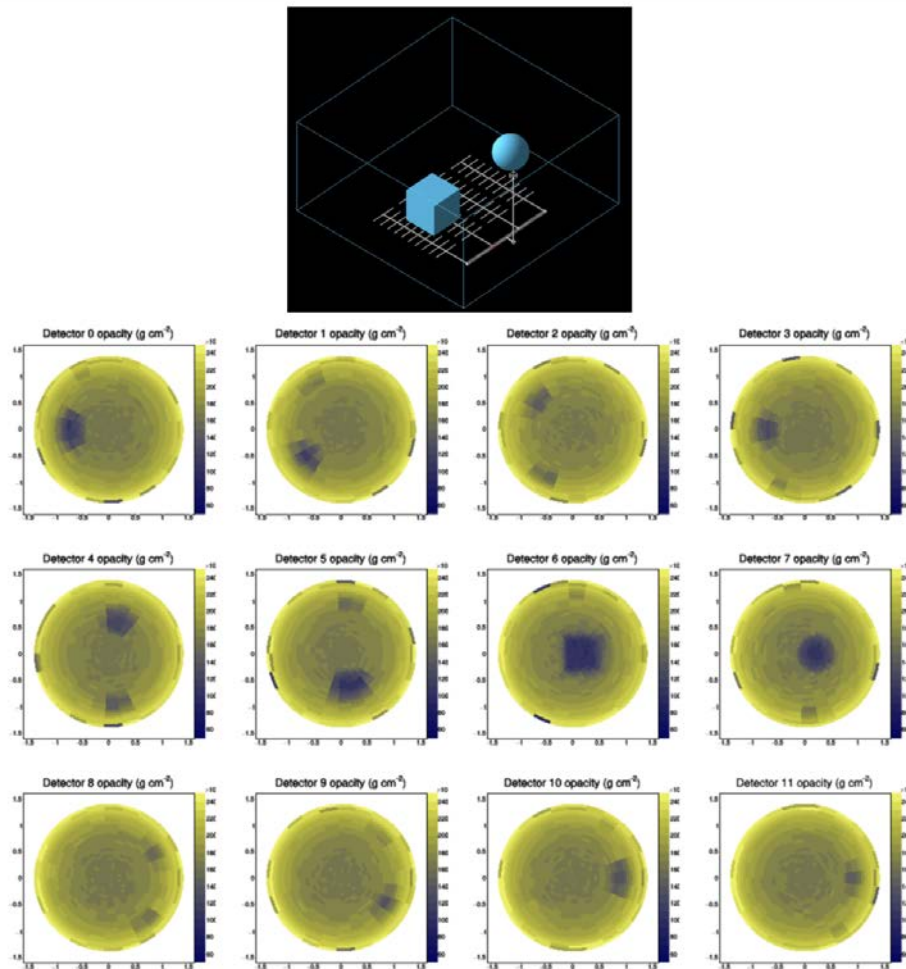


Figure 2: (top) Simulated view of the disposal facility geometry depicting two large voids, (bottom) opacity data from 12 different detectors deployed at various positions under the voids.

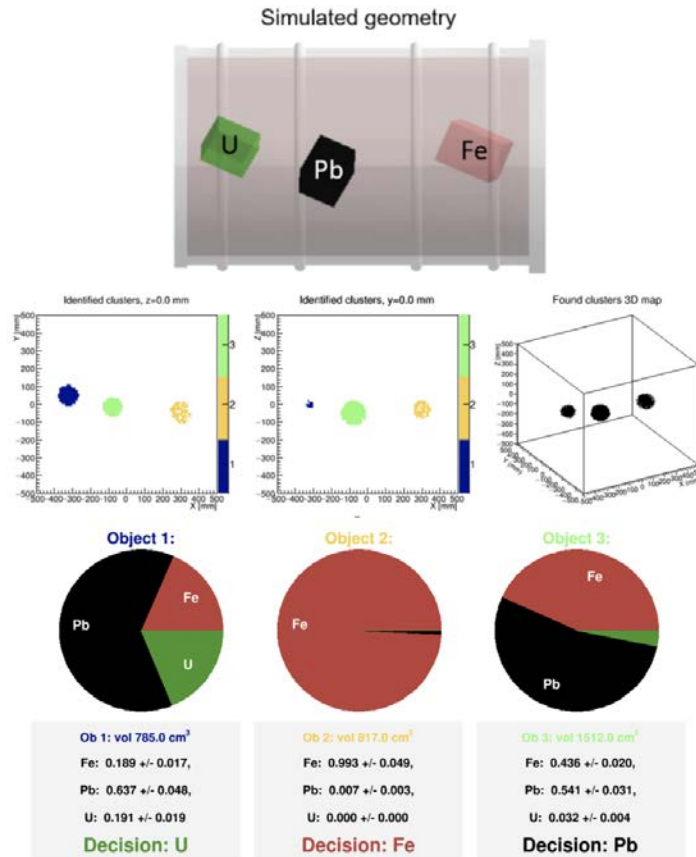


Figure 3: (top) Simulated in-canister geometry with 3 cubes of different materials inside the CASTOR/V52 disposal canister, (centre) clustering in z, y and 3D, (bottom) output of the BDT with material identification decision.

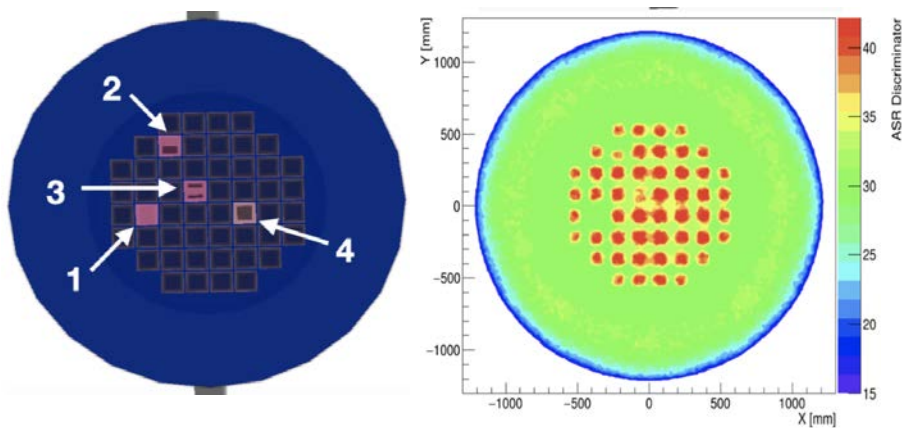


Figure 4: (left) Simulated CASTOR V/52 with 4 diversion scenarios considered (see text for detail), (right) subsequent image created using muon scattering tomography.

Next steps: experiments at Grimsel

The simulations described above are particularly useful in understanding the scope, potential and limitations for muon tomography. These initial simulations will continue to be developed and enhanced as the use case for muon tomography becomes clearer. Details such as the number of detection systems, their efficiency, resolution, configurations, etc. will all be explored and will help to educate our understanding of the relevance of this technique to the particular application being considered here. However, experience shows that empirical data is crucial in the development process for such a technique as muon tomography. In this respect, the possibility of deploying instrumentation at the Grimsel Test Site (GTS) is of great interest, a number of possible experiments can be considered which can be seen as “proof of concept” and which have the potential to address some of the safety and safeguards concerns described above.

1. Open sky/muon flux measurements

In general performing a careful measurement of the so-called “open sky flux” (i.e. no overburden) is an important initial step for any muon tomography experiment as it provides a data point to calibrate against. In this case this requirement could be extended to an open sky scan at the surface as a function of inclination of a detection system which may be of interest since, due to the local geology, the amount of material that the muons will pass through as a function of both inclination and rotation will change appreciably. This would provide a useful cross-check of our understanding of the muon flux due to the local geology.

2. Overburden imaging

This muon radiography test could be done using either large planar detectors deployed in a tunnel and/or a set of smaller borehole detectors deployed in a borehole. Ideally, to benefit from the maximum muon flux, the detectors would be deployed under the object to be imaged; however, a deployment which involves sideways imaging is often more practical. In order to simulate real use in a future GDF, it will be of interest to compare images formed using both deployment methods (sideways measurements and measurements made from under the object) to compare detector performance and practical challenges. If there are areas in GTS where there are known variations and/or voiding in the overburden then a deployment capable of imaging such a feature would be optimal. Any known voiding, including, e.g. pre-existing tunnels, may prove a useful surrogate for the imaging of karsts and other features in alternate geologies (see figure 5 below).

3. Disposal canister imaging (MST)

Any mock disposal canisters on the surface or underground could be imaged using multiple detector systems permitting through-going muons to be recorded such that a muon scattering measurement could take place. Again, ideally large planar detectors would be used however other systems, such as borehole detectors, could be considered.

4. Disposal canister imaging (muon radiography)

Here disposal canisters would be imaged from below or to the side using single-sided muon radiography which could look through an overburden that contains a tunnel with one or more disposal canisters. Any image would be coarse but could convey useful information needed for safety and safeguards purposes such as the configuration and state (upright, fallen over, etc.) of any disposal canisters or simply a “fingerprint” confirmation that the canisters disposed are still present. (see figure 6 below).

5. Long-term variations

Here the object to be imaged would ideally be one which is expected to change on timescales shorter than the measurement time, e.g. volumes susceptible to water ingress, etc. In this case muon radiography via, ideally, a large area system, would track changes in the muon count rate as a function of time and correlations with expected overburden changes from rainfall events, etc. considered. Possible experimental configurations are depicted in figures 6 and 7. Note that in the proposed experiments in figures 6 and 7 there exists a very compelling medium-term programme of work that has been proposed by GTS that would involve (1) a measurement with an empty gallery, then (2) with the gallery populated with dummy canisters then finally (3) with addition of backfill.

6. Detector format comparisons

In general, when designing muon tomography instrumentation for a particular application, there are a number of factors to be considered including performance characteristics, e.g. the angular resolution of a detector system will dictate the granularity of any resulting image. Furthermore, a general rule is to deploy as large a detection area as possible which reduces the measurement time. An obvious way to do this is to deploy one or more large planar detectors which are commonplace in a number of applications, e.g. volcano imaging. However, in the long term, it is likely that borehole detectors will be more relevant to a GDF. It is therefore of interest, in this early stage of demonstrating the muon tomography concept, to compare detectors in these different formats, as is illustrated in figures 6 and 7.

References

- [1] Cosmic rays measure overburden of tunnel, E.P. George, Commonwealth Engineer (1955) 455.
- [2] Muon tomography for railway tunnel imaging, L.F. Thompson et al., Phys. Rev. Research 2 (2020) 023017.
- [3] Radiographic visualization of magma dynamics in an erupting volcano, H.K.M. Tanaka et al., Nature Communications 5 (2014) 3381.
- [4] Search for hidden chambers in the pyramids, L. W. Alvarez et al., Science 167 (1970) 832.
- [5] Discovery of a big void in Khufu's Pyramid by observation of cosmic-ray muons. K. Morishima et al., Nature 552 (2017) 386.
- [6] Muon trackers for imaging a nuclear reactor, N. Kume et al., Journal of Instrumentation 11 (2016) P09008.
- [7] International nuclear material safeguards for the final disposal of spent nuclear fuel – why, what and how, I. Niemeier, K. Aymanns et al., Presentation at safeND 2021.
- [8] Muon Tracing and Image Reconstruction Algorithms for Cosmic Ray Muon Computed Tomography, IEEE Trans. Image Processing, vol. 28 (2019) 426-435.
- [9] Material identification in nuclear waste drums using muon scattering tomography and multivariate analysis, M.J. Weekes et al., JINST 16 (2021) P05007.

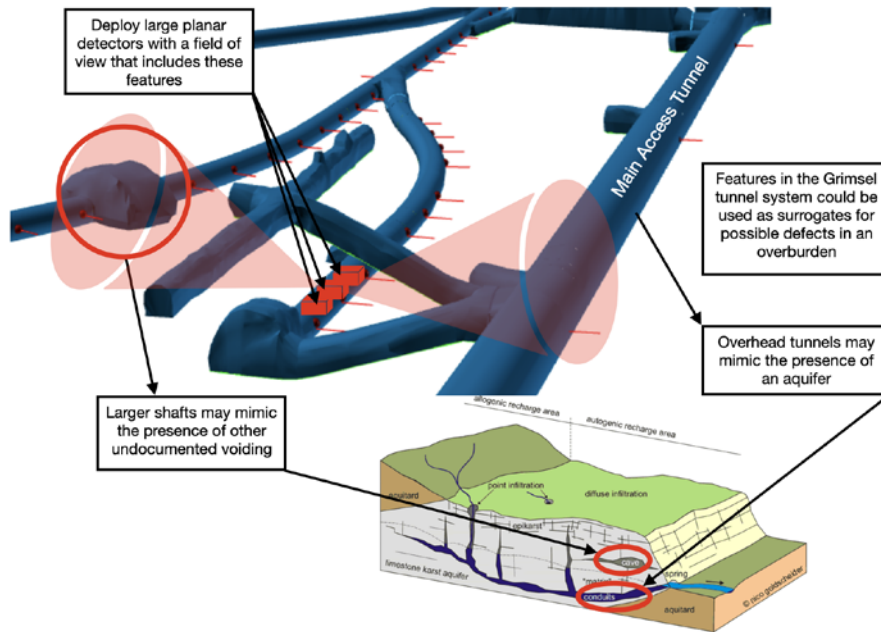


Figure 5: Schematic of overburden imaging

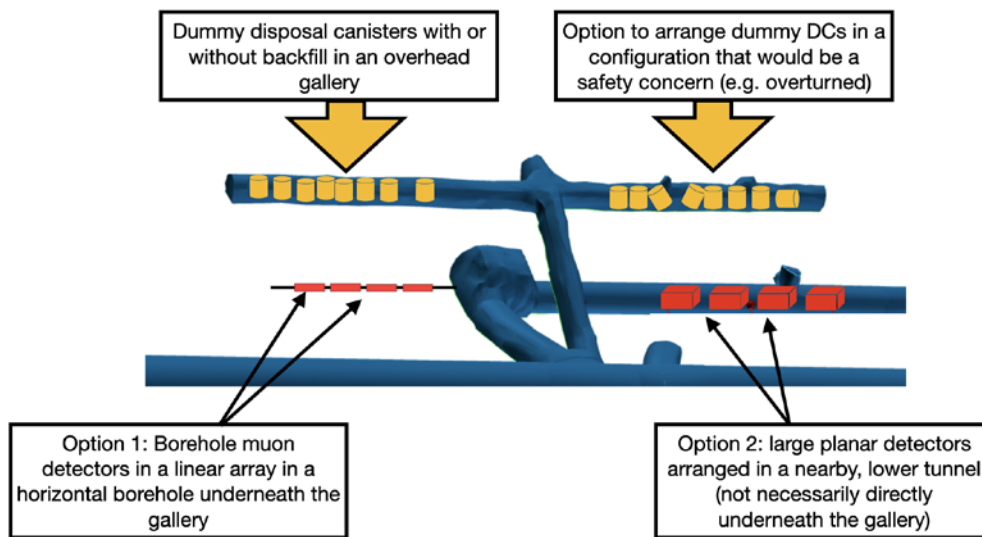


Figure 6: Schematic of disposal canister imaging

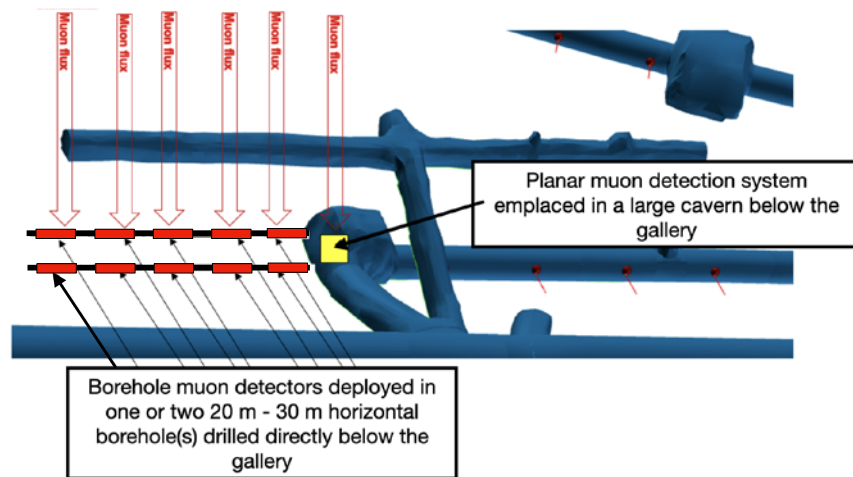


Figure 7: Schematic of long-term disposal overburden imaging